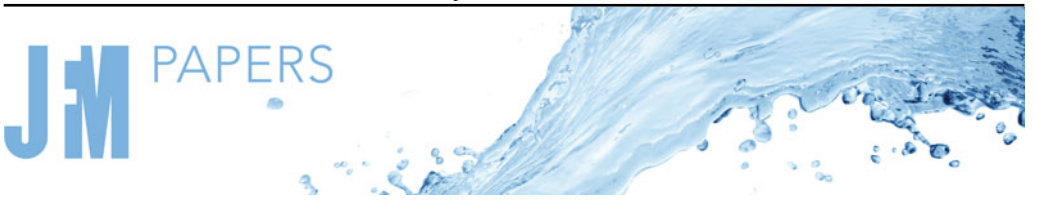
J. Fluid Mech. (2026), *vol.* 1041, A5, doi:10.1017/jfm.2026.11913



On the joint estimation of flow fields and particle properties from Lagrangian data

Ke Zhou[1] **and Samuel Jacobi Grauer**[1]

[1]Department of Mechanical Engineering, Pennsylvania State University, University Park, PA, USA
Corresponding author: Samuel Jacobi Grauer, sgrauer@psu.edu

(Received 5 October 2025 UTC; revised 23 May 2026 UTC; accepted 10 July 2026 UTC)

We numerically investigate the feasibility and limits of jointly estimating flow fields and unknown particle properties (e.g. position, size and density) from Lagrangian particle tracking data. Lagrangian particle tracking offers time-resolved, volumetric measurements of particle trajectories, which are markers of the carrier fluid motion. However, experimental tracks are spatially sparse and potentially noisy, and the problem of reconstructing flow fields may be further complicated by inertial particle transport, such that particle slip velocities must be determined to access the velocity field of the carrier fluid. To address this problem, we develop a data assimilation framework that couples an Eulerian representation of the flow with Lagrangian particle models, enabling the simultaneous inference of carrier fields and particle properties under the governing equations of disperse multiphase flow. We show that flow fields and particle properties can be jointly estimated in three representative regimes: (i) in a turbulent boundary layer with noisy tracer tracks ($St \to 0$), flow fields and true particle positions are jointly estimated, which amounts to a physics-informed particle tracking problem; (ii) in homogeneous isotropic turbulence seeded with inertial particles ($St \sim 1-5$), we demonstrate simultaneous recovery of flow states and particle diameters, showing the feasibility of implicit particle characterisation; and (iii) in a compressible, shock-dominated flow, we report the first joint reconstructions of velocity, pressure, density and inertial particle properties (diameter and density), highlighting both the potential and certain limits of joint estimation in supersonic regimes. A systematic sensitivity study reveals how the seeding density, noise level and Stokes number govern reconstruction accuracy for our method.

Key words: variational methods, particle/fluid flows

© The Author(s), 2026. Published by Cambridge University Press. This is an Open Access article, distributed under the terms of the Creative Commons Attribution licence (https://creativecommons.org/licenses/by/4.0/), which permits unrestricted re-use, distribution and reproduction, provided the original article is properly cited.

https://doi.org/10.1017/jfm.2026.11913 Published online by Cambridge University Press

1. Introduction

Understanding and modelling turbulent flow in real-world systems ideally call for dense, time-resolved Eulerian fields: velocity, pressure, density and gradient tensors of the same. These fields allow one to educe coherent structures and superstructures (Schröder *et al.* 2009; Schanz *et al.* 2018; Weiss *et al.* 2023), quantify energy transfer and dissipation (Schneiders *et al.* 2017; Schröder *et al.* 2022), determine surface loading from pressure and shear stress (Rival & van Oudheusden 2017; van Gent *et al.* 2017; Jux *et al.* 2020), analyse buoyancy-driven transport in convection (Muralidhar 2002; Wissink & Herlina 2023) and so forth. In principle, scale-resolving computational fluid dynamics (CFD) methods can deliver such fields, but direct numerical simulation (DNS) becomes intractable when applied to device-scale flows at realistic Reynolds numbers (Slotnick *et al.* 2014; Cary *et al.* 2021), and large-eddy simulation depends on subgrid-scale closures that require tuning for new physical regimes (Argyropoulos & Markatos 2015; Duraisamy *et al.* 2019). Even in a small subdomain, accurate simulations hinge on the fidelity of boundary conditions that are often difficult to specify, such as representative upstream disturbances (Buchta *et al.* 2022; Johnson *et al.* 2023), wall heat fluxes (Roy & Blottner 2006) or coherent structures in the inflow (Gorlé *et al.* 2015; Xiao & Cinnella 2019). These boundaries are challenging to measure experimentally, and it is uncommon to set up CFD simulations using empirical unsteady boundary conditions.

Experiments, by contrast, capture the true behaviour of flows but yield measurements that are typically sparse, noisy and indirectly related to the quantities of interest. Data assimilation (DA) offers a means to combine these complementary capabilities: enforcing the governing equations via CFD methods while matching available measurements, thereby producing physically consistent reconstructions of real flows (He *et al.* 2025; Zaki 2025; Zaki & Wang 2025). In this context, Lagrangian particle tracking (LPT) (Schröder & Schanz 2023) is an especially attractive diagnostic because it provides time-resolved, volumetric velocity and acceleration information in complex configurations and at high Reynolds numbers. The data, however, are limited to particle trajectories (also known as 'tracks') that are spatially sparse, subject to localisation and tracking errors, and, in some flows, whose velocities deviate from the underlying fluid velocity due to particle inertia. This leads to the central question motivating our study: Given experimentally realisable Lagrangian data, to what extent can we recover the antecedent sequence of Eulerian flow states and salient particle properties, such as their true positions, sizes and densities, by supplementing the tracks with the equations of motion for the carrier and particle phases in a DA reconstruction?

1.1. *Capabilities and limitations of Lagrangian particle tracking*

Lagrangian particle tracking has emerged as a leading diagnostic for volumetric velocimetry in both laboratory and field environments (Bristow *et al.* 2023; Li *et al.* 2024; Schröder *et al.* 2024). Compared with tomographic particle image velocimetry (PIV) (Scarano 2012), it achieves higher spatial resolution and nearly ghost-free particle fields, enabling more accurate computation of derivatives and more reliable pressure inference (van Gent *et al.* 2017). Tracks are obtained by seeding the flow with tracer particles (or by leveraging natural tracers), imaging them with one or more cameras and reconstructing three-dimensional (3-D) particle positions before linking them in time. Multi-camera triangulation provides high-accuracy localisation from overlapping views, while single-camera methods such as digital in-line holography (DIH) (Toloui *et al.* 2015; Mallery *et al.* 2019), plenoptic cameras (Fahringer *et al.* 2015; Hall *et al.* 2017) or defocusing imaging (Guo *et al.* 2019) enable four-dimensional measurements in settings where optical

https://doi.org/10.1017/jfm.2026.11913 Published online by Cambridge University Press

access is limited. Recent advances, including the predictor–corrector approach of shake-the-box (STB) tracking (Schanz *et al.* 2016; Schröder *et al.* 2024), object-aware LPT near boundaries (Wieneke & Rockstroh 2024), field-scale deployments in atmospheric turbulence (Bristow *et al.* 2023; Li *et al.* 2024) and multi-pulse schemes for high-speed compressible flows (Novara *et al.* 2019; Manovski *et al.* 2021), have expanded the technique's reach. Hence, LPT is now frequently applied to flows of practical relevance.

Two challenges are especially relevant to the question of what can be inferred from LPT data. The first challenge is localisation and tracking error. Although present in all LPT variants, these errors are most severe for single-camera systems (i.e. based on plenoptic or DIH imaging), which suffer from strongly anisotropic uncertainties due to depth-of-focus limitations. The largest errors occur along the optical axis (Katz & Sheng 2010; Gao *et al.* 2013), degrading velocity estimates and, in turn, derived quantities such as vorticity and pressure. The second challenge is inertial transport. Particles with finite response times, characterised by their Stokes number $St = \tau_p/\tau_f$, where τ_p and τ_f are characteristic time scales of the particle and carrier fluid, deviate systematically from the local fluid velocity (Melling 1997; Raffel *et al.* 2018). While small particles, with $St < 0.1$, are used to ensure good 'traceability' in LPT, inertial particle transport may occur inadvertently in both laboratory and natural settings. Examples include helium-filled soap bubbles in wind tunnels (Wolf *et al.* 2019; Faleiros *et al.* 2021), solid particles in shocked flows (Ragni *et al.* 2011), snowflakes in the atmospheric boundary layer (Li *et al.* 2022; Bristow *et al.* 2023) and sediment transport in waterways (Righetti & Romano 2004), with St varying from 0.1 to 10 in these examples. Track errors and particle inertia seemingly reduce the information content of LPT data and thus prevent the accurate determination of flow fields from particle tracks in a typical LPT workflow.

1.2. *Data assimilation for Lagrangian particle tracking*

Early reconstruction approaches for LPT converted Lagrangian tracks into Eulerian fields by interpolation (Agüí & Jimenez 1987; Malik & Dracos 1995), but these methods were limited by the particle sampling resolution and prone to amplifying noise. Modern DA methods incorporate the Navier–Stokes equations as constraints, either as hard constraints (ensemble Kalman filters (Deng *et al.* 2018); adjoint–variational methods (Gronskis *et al.* 2013; Foures *et al.* 2014; He *et al.* 2024)) or as soft ones (physics-based interpolation with B-splines (Gesemann *et al.* 2016); radial basis functions (Casa & Krueger 2013); vorticity formulations (Jeon *et al.* 2018)). By enforcing physical consistency, these methods have the potential to reconstruct velocity fields beyond the limits of interpolation *per se*, recovering information at scales finer than the particle-sampling Nyquist wavenumber (though this has yet to be demonstrated experimentally). Machine learning variants, like those based on physics-informed neural networks (PINNs) (Raissi *et al.* 2019), offer flexible functional representations and have been successfully applied to a broad range of flows. They are increasingly relied upon for LPT DA, including in the present study, owing to their ease of implementation, robustness in inverse settings and demonstrated accuracy with sparse or noisy data (Zhou *et al.* 2024).

Two central difficulties remain when processing LPT data, stemming from the challenges introduced above. One is localisation and tracking errors, which directly limit the fidelity of reconstructed velocities; these errors can be compounded by biases which are inadvertently introduced during track filtering. The other is the assumption of ideal tracers, which breaks down when particles have non-negligible inertia, creating the additional challenge of jointly inferring particle properties alongside flow fields. In other words, the particle–flow coupling must be modelled to reconstruct the flow, and

https://doi.org/10.1017/jfm.2026.11913 Published online by Cambridge University Press

it is not known *a priori* whether carrier-phase flow fields and particle properties can be jointly determined from LPT track data. A related theoretical question is whether the same framework can also recover the true particle positions from noisy measurements. Although this is rarely a primary objective in LPT, since particle positions are merely a means to recover flow fields, successful recovery of the true positions from noisy data would indicate that the governing physics and the measurements jointly constrain the track geometries, highlighting the information content of Lagrangian data in turbulence. Addressing these challenges requires a DA framework that treats particle positions as the measured quantity rather than velocities, encodes the coupled carrier-phase and particle-phase dynamics and operates directly on noisy particle position data. The development and demonstration of such a framework is one focus of this work.

1.3. *Present approach and investigations of joint estimation*

We empirically demonstrate the feasibility of jointly estimating flow fields and particle properties using a framework that we term neural-implicit particle advection (NIPA). The NIPA framework couples an Eulerian flow model, parametrised by coordinate neural networks (i.e. PINNs when trained with a physics loss), to individual Lagrangian particle models that embed the particle advection equation as a hard constraint. For inertial particles, their size, density and other attributes enter the model as trainable parameters, enabling estimation of properties that determine their response times. The governing physics enter via soft constraints on the Navier–Stokes equations for the carrier phase and an extended Maxey–Riley formulation for the particle (or 'disperse') phase (Subramaniam & Balachandar 2022). By design, NIPA works directly from the raw track positions, avoiding any biases induced by filtering the tracks, and it estimates both flow states and particle properties without requiring direct observations of either.

The NIPA framework provides numerical means to assess the factors that govern reconstruction accuracy across a range of flow regimes and measurement conditions. Moreover, it represents an algorithmic advance in LPT DA. We probe the degree to which flow fields can be recovered from Lagrangian data through synthetic test cases that include noisy tracks from ideal tracers in incompressible turbulence, inertial particles in the same and inertial particles in a compressible flow with a shock wave. In each case, we examine whether the available track data and governing equations suffice to recover the flow field and particle properties, and we study the sensitivity of reconstruction accuracy to the seeding density, noise level and Stokes number. These results provide empirical evidence for the existence of an inverse mapping from a Lagrangian measurement manifold to a flow's global attractor in state space. Despite the empirical nature of this work, our findings motivate a formal analysis of the joint observability of flow–particle systems (Zaki 2025). The remainder of this paper outlines the reconstruction methodology in § 2, describes the flow cases used for numerical testing in § 3 and the implementation details in § 4, tests the joint estimation of particle positions for ideal tracers in § 5 and extends this treatment to inertial particles for turbulent and compressible flow reconstruction in § 6. Lastly, in § 7, we investigate the sensitivity of reconstruction accuracy to both particle inertia and noise before concluding the paper in § 8.

2. Methodology: neural-implicit particle advection

Understanding when flow fields and particle properties can be jointly recovered from Lagrangian data requires a DA algorithm that accounts for the physics of both phases. Existing DA methods either reconstruct the flow but treat the particles as ideal tracers, neglecting particle–fluid interactions, or they infer the particle dynamics given full

https://doi.org/10.1017/jfm.2026.11913 Published online by Cambridge University Press

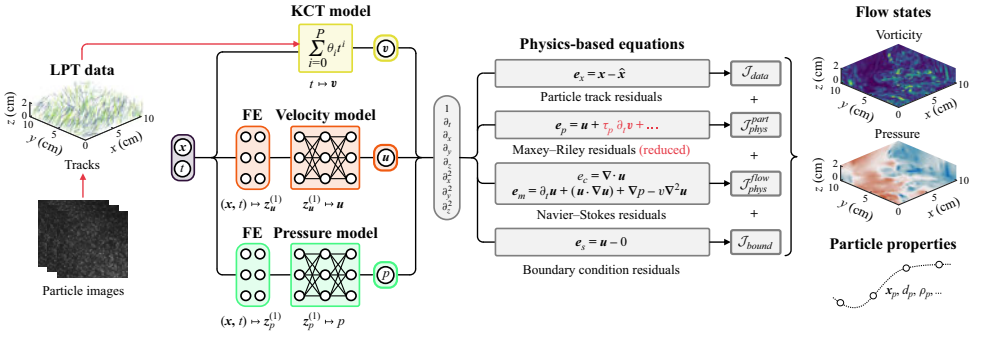


Figure 1. Architecture of the neural DA solver. Eulerian flow fields are represented by one or more neural networks. Fourier encoding (FE) enhances network expressivity and broadband spectral coverage. Each particle is represented by a Lagrangian kinematics-constrained track (KCT) model. Flow fields, particle kinematics and particle properties (when $St > 0$) are jointly inferred from the data and governing equations.

knowledge of the flow field (Domínguez-Vázquez *et al.* 2025). Neither approach is adequate to the task at hand. To remedy this shortcoming, we introduce a new framework for LPT DA, which we call NIPA. It features dedicated models of both the flow and the particles, which are coupled through the governing equations of disperse multiphase flow, namely the Navier–Stokes and extended Maxey–Riley equations. By simultaneously optimising the flow and particle models to satisfy these equations, NIPA recovers not only time-resolved flow fields but also enhanced particle trajectories and otherwise unknown particle properties. This tool thus enables the systematic evaluation of how dataset attributes (e.g. the number and spacing of particles, data fidelity, particle inertia and compressibility) affect reconstruction accuracy. Below, we present our framework, define the objective loss terms and describe our flow and particle models.

2.1. *Framework for data assimilation*

The NIPA framework employs 'neural-implicit flow states' coupled to a set of particle models, with one model per particle, to reconstruct unsteady flow fields from Lagrangian tracks. A schematic of the approach is shown in figure 1. The flow field is represented using one or more coordinate neural networks, which take space–time input coordinates and return flow variables at that position and time:

$$\mathsf{F} : \mathcal{V} \times \mathcal{T} \to \mathbb{R}^{d+1}, \quad (\boldsymbol{x}, t) \mapsto (\boldsymbol{u}, p), \tag{2.1}$$

where $\boldsymbol{x} \in \mathcal{V}$ are the spatial coordinates in the flow domain $\mathcal{V}$, $t \in \mathcal{T}$ is a time within the measurement interval $\mathcal{T}$, $\boldsymbol{u}$ and p are the velocity and pressure fields, respectively, and $d = 2$ or 3 is the number of spatial dimensions. Additional variables can be added to the outputs of F as needed, such as density or temperature in compressible flows. When coordinate neural networks like F are trained to minimise residuals to a set of physical equations, they are deemed to be PINNs. Network architectures used in this work are described in more detail in § 2.3.

We next introduce the concept of our Lagrangian particle model, whose detailed formulation is derived in § 2.4. Measured particle tracks natively comprise sequences of spatial positions determined at the image times. Accordingly, our particle models are defined with respect to these tracked locations, which may be adjusted during training to account for localisation uncertainty. For the kth particle, a dedicated model $\mathsf{P}^{(k)}$ is built to

https://doi.org/10.1017/jfm.2026.11913 Published online by Cambridge University Press

represent its velocity as a continuous function of time:

$$\mathsf{P}^{(k)} : \mathcal{T}^{(k)} \to \mathbb{R}^d, \quad t \mapsto \boldsymbol{v}^{(k)} \quad \text{for} \quad k \in \{1, \ldots, n_p\}, \tag{2.2}$$

where $\boldsymbol{v}^{(k)}$ is the velocity of particle k at time $t \in \mathcal{T}^{(k)}$, $\mathcal{T}^{(k)} \subseteq \mathcal{T}$ is the time span of that track and n_p is the total number of particle tracks. Although $\mathsf{P}^{(k)}$ may take various forms, a physical track model must satisfy both kinematic and dynamic constraints. Kinematic consistency corresponds to an advection equation:

$$\boldsymbol{x}_j{}^{(k)} - \boldsymbol{x}_{j-1}{}^{(k)} = \int_{t_{j-1}}^{t_j} \boldsymbol{v}^{(k)}(t)\ \mathrm{d}t \quad \text{for} \quad j \in \{1, \ldots, n_k - 1\}, \tag{2.3}$$

where $\boldsymbol{x}_j{}^{(k)}$ is the position of particle k at the jth time step t_j and n_k is the number of measurement points along that track. We embed this advection equation (2.3) as a hard constraint into $\mathsf{P}^{(k)}$, as elaborated in § 2.4. The dynamic consistency of $\mathsf{P}^{(k)}$ is weakly enforced by the physics-based optimisation described in § 2.2.

Our formulation of $\mathsf{P}^{(k)}$ provides a general framework for modelling the kinematics of both ideal tracers and inertial particles. In the latter case, properties of inertial particles like their size, density and shape determine τ_p and govern the particles' coupling to the carrier fluid (Subramaniam & Balachandar 2022). These properties, and hence any slip velocities, are nearly always unknown in practice, complicating the reconstruction problem. To address this, we treat the relevant particle properties as model parameters to be learned, enabling the implicit characterisation of particles from LPT data in conjunction with the equations of motion for both phases. In well-characterised experiments, by contrast, where the pertinent particle properties are known prior to reconstruction, they may be fixed in the model.

2.2. *Composite objective function*

Flow and particle states ought to satisfy the governing equations for both phases, they must match known boundary conditions and they should be consistent with the observed LPT data. To achieve these objectives, the flow model F and particle models $\mathsf{P}^{(k)}$ are trained in tandem by minimising a composite loss:

$$\mathscr{J}_{total} = \chi_1 \mathscr{J}^{\boldsymbol{x}}_{data} + \chi_2 \mathscr{J}^{flow}_{phys} + \chi_3 \mathscr{J}^{part}_{phys} + \chi_4 \mathscr{J}_{bound}, \tag{2.4}$$

where χ_i are weighting coefficients that balance the relative contributions of each term. The four loss terms, detailed below, are the position-based data fidelity term $\mathscr{J}^{\boldsymbol{x}}_{data}$ (cf. the velocity-based term in § 2.2.4), the flow physics term $\mathscr{J}^{flow}_{\mathrm{phys}}$, the particle physics term $\mathscr{J}^{part}_{phys}$ and the boundary condition term $\mathscr{J}_{bound}$.

2.2.1. *Data fidelity loss*

Particle positions are treated as trainable parameters, meaning that the estimated position of each particle at each measurement time can be adjusted during reconstruction. Without additional constraints, however, allowing the particles to move risks unmooring the models from the measurements. To anchor reconstructions to the experiment, therefore, we introduce a data fidelity term that penalises discrepancies between measured and estimated positions, weighted by the localisation uncertainty:

$$\mathscr{J}^{\boldsymbol{x}}_{data} = \left(\frac{1}{d n_p} \sum_{k=1}^{n_p} \frac{1}{n_k} \sum_{i=1}^{n_k} \underbrace{\left\| \boldsymbol{x}_i{}^{(k)} - \widehat{\boldsymbol{x}}_i^{(k)} \right\|^2_{\boldsymbol{L}}}_{\text{chi-squared statistic}} - 1 \right)^2. \tag{2.5}$$

https://doi.org/10.1017/jfm.2026.11913 Published online by Cambridge University Press

Here, ${\boldsymbol{x}_i}^{(k)}$ and $\widehat{\boldsymbol{x}}_i^{(k)}$ are the measured and estimated (i.e. trainable) positions of the kth particle at time t_i, with n_p total tracks and n_k samples in the kth track. The norm is the matrix-weighted Mahalanobis norm:

$$\|\Delta \boldsymbol{x}\|_{\boldsymbol{L}}^2 = \Delta \boldsymbol{x}^\top \boldsymbol{L}^\top \boldsymbol{L} \Delta \boldsymbol{x}, \quad \text{where} \quad \boldsymbol{L}^\top \boldsymbol{L} = \boldsymbol{\Gamma}^{-1} \tag{2.6}$$

and $\boldsymbol{\Gamma}$ is the covariance matrix for the localisation errors. For independent, centred Gaussian errors, the weighted norm follows a chi-squared distribution with d degrees of freedom, where d is the dimension of $\boldsymbol{x}$ and also the expected value of the statistic. Normalising the chi-squared statistic by d, subtracting 1 and squaring the result, as in (2.5), encourages consistency of the residuals $\|{\boldsymbol{x}_i}^{(k)} - \widehat{\boldsymbol{x}}_i^{(k)}\|_2$ with the expected statistics of the localisation errors. Values below d are indicative of overfitting to noise, while values above d suggest underfitting. In isolation, (2.5) acts as a maximum likelihood criterion for the particle positions. Notably, there exists an infinite set of minimisers for (2.5) for any set of LPT data. When coupled with the physics and boundary losses, however, the data loss enables a physics-informed particle tracking method. Both uses of (2.5) are demonstrated in § 5.

2.2.2. *Physics-based loss terms*

The flow physics loss penalises residuals of the carrier-phase governing equations:

$$\mathscr{J}_{phys}^{flow} = \frac{\dim(\boldsymbol{e}_f)^{-1}}{|\mathcal{V} \times \mathcal{T}|} \int_{\mathcal{T}} \int_{\mathcal{V}} \|\boldsymbol{e}_f\|_2^2 \, \mathrm{d}\boldsymbol{x} \, \mathrm{d}t, \tag{2.7}$$

where $\boldsymbol{e}_f$ is the residual vector associated with the governing flow equations within $\mathcal{V} \times \mathcal{T}$. For domains with transient boundaries, the space–time domain is not the simple Cartesian product of $\mathcal{V}$ and $\mathcal{T}$; see Tang *et al.* (2026) for details on handling such situations. While most LPT DA algorithms are restricted to incompressible flows, the present framework can be extended to compressible configurations with minimal modification. Appendix A summarises the governing equations used in this study.

The particle physics loss is based on residuals from an equation of motion for the disperse phase:

$$\mathscr{J}_{phys}^{part} = \frac{\dim(\boldsymbol{e}_p)^{-1}}{n_p} \sum_{k=1}^{n_p} \frac{1}{|\mathcal{T}^{(k)}|} \int_{\mathcal{T}^{(k)}} \|{\boldsymbol{e}_p}^{(k)}\|_2^2 \mathrm{d}t, \tag{2.8}$$

where ${\boldsymbol{e}_p}^{(k)}$ is the residual of the kth particle's governing equation. For small spherical particles with a vanishing particle Reynolds number, the dynamics is described by the Maxey–Riley equation (Maxey & Riley 1983; Capecelatro & Wagner 2023). The specific form adopted in this work, including its adaptation for compressible flows, is summarised in Appendix B. In cases with inertial particle transport, information about particle properties is obtained through the residuals in (2.8), since the equation of motion (and therefore ${\boldsymbol{e}_p}^{(k)}$) generally depends on the flow velocity $\boldsymbol{u}$, the particle velocity $\boldsymbol{v}^{(k)}$ and particle characteristics such as their sizes and densities.

In many LPT experiments, the particles are carefully selected to behave as ideal tracers with negligible slip velocities. In the limit $St \to 0$, the particle and carrier motions are equal. Hence, we specify velocity and acceleration residuals for ideal tracers:

$${\boldsymbol{e}_{p,\boldsymbol{u}}}^{(k)} = \boldsymbol{u} - \boldsymbol{v}^{(k)} \quad \text{and} \quad {\boldsymbol{e}_{p,\boldsymbol{a}}}^{(k)} = \frac{\mathrm{D}\boldsymbol{u}}{\mathrm{D}t} - \boldsymbol{a}^{(k)}, \tag{2.9}$$

https://doi.org/10.1017/jfm.2026.11913 Published online by Cambridge University Press

where $\mathrm{D}/\mathrm{D}t$ is the material derivative operator, $\boldsymbol{a}^{(k)}$ is the acceleration of a particle and $\boldsymbol{e}_p$ is the concatenation of $\boldsymbol{e}_{p,\boldsymbol{u}}$ and $\boldsymbol{e}_{p,\boldsymbol{a}}$.

2.2.3. *Boundary condition loss*

Although neural state estimation does not explicitly require boundary conditions, incorporating known constraints can improve reconstruction accuracy. In turbulent boundary layers (TBLs), for instance, enforcing a no-slip condition at the wall enhances near-wall resolution, where positional uncertainties are worsened by optical reflections and where the flow scales are smallest. This combination of large relative uncertainty and fine-scale dynamics makes boundary conditions especially valuable near walls. The no-slip boundary loss is

$$\mathscr{J}_{bound} = \frac{\dim(\boldsymbol{u})^{-1}}{|\mathcal{A}\times\mathcal{T}|}\int_{\mathcal{T}}\int_{\mathcal{A}} \|\boldsymbol{u}\|_2^2 \,\mathrm{d}\boldsymbol{x}\,\mathrm{d}t, \tag{2.10}$$

where $\mathcal{A}\subseteq\partial\mathcal{V}$ denotes the no-slip portion of the domain boundary $\partial\mathcal{V}$. This formulation can be extended to moving-wall conditions (Tang *et al.* 2026), enabling the inference of wall motion, or to hybrid constraints that feature multiple variables (e.g. a constant free-stream density, adiabatic walls, or known pressures at tap locations) and boundary types (Dirichlet, Neumann, Robin), depending on the pertinent physics.

2.2.4. *Baseline flow-only reconstruction*

To evaluate the added value of joint flow–particle reconstruction, we implement a simplified baseline that neglects the particle models and instead relies on velocity information derived from the particle tracks through an intermediate step, as is common in LPT DA (Di Leoni *et al.* 2023; Shin & Schröder 2025). In this baseline, the framework reduces to a flow network F that is trained to reproduce the track-based velocity estimates $\widehat{\boldsymbol{v}}$ while satisfying the governing equations and boundary conditions. The corresponding loss is

$$\mathscr{J}_{total} = \chi_1\mathscr{J}^{\boldsymbol{u}}_{data} + \chi_2\mathscr{J}^{flow}_{phys} + \chi_3\mathscr{J}_{bound}, \tag{2.11}$$

where $\mathscr{J}^{\boldsymbol{u}}_{data}$ enforces agreement between the reconstructed flow velocity and particle velocities inferred from the tracks. The velocity-based data fidelity term is

$$\mathscr{J}^{\boldsymbol{u}}_{data} = \frac{1}{n_p}\sum_{k=1}^{n_p}\frac{1}{n_k}\sum_{i=1}^{n_k}\left\|\boldsymbol{u}-\widehat{\boldsymbol{v}}_i^{(k)}\right\|_2^2, \tag{2.12}$$

where $\boldsymbol{u}$ is the velocity field from F and $\widehat{\boldsymbol{v}}_i^{(k)}$ is the velocity estimate for the kth particle at time t_i. Such estimates may be obtained by differentiating the tracked positions, but finite differencing amplifies noise, so smoothing or interpolation schemes like those based on B-splines, polynomial fits or kernel convolution are often applied. Here, we demonstrate 'baseline reconstructions' using both a second-order finite-difference scheme (with single-sided differences at the track ends) and a quasi-optimal B-spline filter, detailed in Appendix C. While these methods can suppress the effects of noise in $\widehat{\boldsymbol{v}}_i^{(k)}$, they also embed errors in $\mathscr{J}^{\boldsymbol{u}}_{data}$ through the heuristic choice of filter parameters. By contrast, our position-based formulation in (2.5) and the associated particle models bypass the intermediate estimation of velocity. Instead, we anchor the reconstruction to the measured positions, subject to the localisation error statistics.

https://doi.org/10.1017/jfm.2026.11913 Published online by Cambridge University Press

We wish to emphasise that this 'velocity data loss' formulation is used solely as a baseline. It represents the performance attainable when particle–fluid coupling and particle properties are ignored, thereby highlighting the added value of joint estimation.

2.3. *Neural flow model*

The flow model consists of one or more neural networks, here denoted by F, comprising an input layer, output layer and n_L hidden layers:

$$z^{(n_L+1)} = \mathsf{F}\big(z^{(0)}\big) = \boldsymbol{W}^{(n_L+1)}\big[\mathsf{L}^{(n_L)} \circ \mathsf{L}^{(n_L-1)} \circ \cdots \circ \mathsf{L}^{(2)} \circ \mathsf{G}\big(z^{(0)}\big)\big] + \boldsymbol{b}^{(n_L+1)}, \quad (2.13a)$$

with

$$z^{(L)} = \mathsf{L}^{L}\big(z^{(L-1)}\big) = \mathrm{swish}\big(\boldsymbol{W}^{(L)} z^{(L-1)} + \boldsymbol{b}^{(L)}\big), \quad \text{for} \quad L \in \{2, \ldots, n_L\}. \quad (2.13b)$$

In this expression, $z^{(L)}$ are the outputs at layer L and L represents the operator that maps between consecutive hidden layers. This operator consists of an affine transform followed by a nonlinear activation that is applied element-wise. The matrix $\boldsymbol{W}^{(L)}$ and the vectors $\boldsymbol{b}^{(L)}$ are the weights and biases of the affine transform, respectively; the latter provides an additive offset at each layer (not to be confused with measurement or estimation biases). We use the swish activation

$$\mathrm{swish}(z_i) = \frac{z_i \ \exp(z_i)}{1 + \exp(z_i)}, \quad (2.14)$$

which has been shown to mitigate issues associated with vanishing gradients and is also smooth, making it well suited for representing flow fields that must be at least twice differentiable (Jagtap & Karniadakis 2023). Furthermore, to mitigate the low-frequency bias that commonly occurs in gradient-based training (Wang *et al.* 2021), the first hidden layer $\mathsf{L}^{(1)}$ is replaced by a Fourier encoding G (Tancik *et al.* 2020):

$$z^{(1)} = \mathsf{G}\big(z^{(0)}\big) = \Big[\sin\big(2\pi \boldsymbol{f}_1 \cdot z^{(0)}\big),\ \cos\big(2\pi \boldsymbol{f}_1 \cdot z^{(0)}\big), \ldots,\ \sin\big(2\pi \boldsymbol{f}_{n_f} \cdot z^{(0)}\big),\ \cos\big(2\pi \boldsymbol{f}_{n_f} \cdot z^{(0)}\big)\Big], \quad (2.15)$$

where $\boldsymbol{f}_i$ are random frequency vectors, sampled once upon initialisation and fixed during training, and n_f is the number of features. For an incompressible flow represented by a single network, the input is $z^{(0)} = (\boldsymbol{x}, t)$ and the output is $z^{(n_L+1)} = (\boldsymbol{u}, p)$.

Two additional strategies are used to improve reconstruction accuracy. First, some flow variables (e.g. density, temperature, total energy in compressible flows) must be strictly positive. Enforcing positivity stabilises the inverse problem, and we achieve this by reparametrising the corresponding outputs with a softplus function:

$$\mathrm{softplus}(z_i) = \log\big[1 + \exp(z_i)\big], \quad (2.16)$$

which smoothly maps $\mathbb{R} \to (0, \infty)$. Second, different flow variables often have distinct spectral characteristics, which can hinder the performance of a shared network. For example, in homogeneous isotropic turbulence (HIT), velocity and pressure follow $\kappa^{-5/3}$ and $\kappa^{-7/3}$ scalings, respectively (Kolmogorov 1941; Obukhov 1949; Corrsin 1951). In such cases, it is advantageous to assign dedicated subnetworks, e.g. $\mathsf{F}_{\boldsymbol{u}} : (\boldsymbol{x}, t) \mapsto \boldsymbol{u}$ and $\mathsf{F}_p : (\boldsymbol{x}, t) \mapsto p$. Both strategies are employed in this work where appropriate and noted, accordingly.

2.4. *Kinematics-constrained particle model*

Particles are represented by models that we term kinematics-constrained tracks (KCTs), which embed the advection equation (2.3) as a hard constraint. As a result, trajectories

https://doi.org/10.1017/jfm.2026.11913 Published online by Cambridge University Press

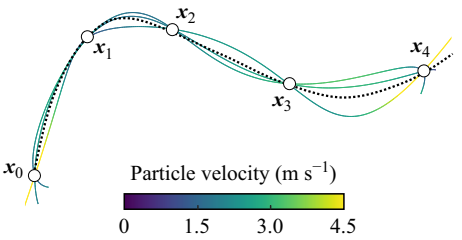


Figure 2. Illustration of a KCT model. Coloured trajectories show particle histories outputted by the KCT, with colour indicating particle speed. Dotted lines indicate the ground truth. Embedding (2.3) as a hard constraint ensures that tracks pass through the specified positions (circles), regardless of adjustments to velocity via $\boldsymbol{\theta}$. Accordingly, $\boldsymbol{\theta}$ remains unconstrained.

given by KCTs always integrate to the positions specified by the model parameters. Measured positions are incorporated directly into the models. When high-fidelity LPT data are available, the specified particle positions can be fixed. In cases with appreciable localisation uncertainty, however, they are treated as trainable variables and refined through optimisation of the position-based data fidelity term $\mathscr{J}^{\boldsymbol{x}}_{data}$ in conjunction with the physics and boundary losses. Velocities, accelerations and intermediate positions are determined by free parameters of the model, but these parameters are themselves unconstrained. Instead, kinematic consistency is enforced by the model formulation, rather than by explicit nonlinear restrictions in parameter space. This ensures that the model outputs meet a baseline of physical fidelity without complicating gradient-based training. Figure 2 illustrates a representative KCT. In the example, tracked positions are fixed while other model parameters are adjusted, yielding multiple velocity histories that integrate to the same set of data.

In what follows, the KCT formulation is presented for a single velocity component v, with the particle index k omitted for clarity. Extension to the full vector $\boldsymbol{v}^{(k)}$ is straightforward. The construction draws on the theory of functional connections (Leake *et al.* 2022), which provides a systematic framework for converting constrained optimisation problems into unconstrained ones. Within this framework, each velocity component can be written as a function of time:

$$v(t) = g(t) + \sum_{j=1}^{n_c} \eta_j \, \varphi_j(t) \,, \tag{2.17}$$

where g is a user-chosen 'free function', η_j is a projection coefficient that enforces the integral constraint over the interval $[t_{j-1}, t_j]$, φ_j is a switch function that activates the projections over time and $n_c = n_k - 1$ is the number of constraints. The choice of g determines the form of the projection coefficients. Here, g is taken as a Pth-order polynomial in time:

$$g(t) = \sum_{i=0}^{P} \theta_i \, t^i, \tag{2.18}$$

with the coefficients θ_i being trainable parameters. To enforce the advection constraint, the projection coefficients are set to

$$\eta_j = \left(x_j - x_{j-1}\right) - \int_{t_{j-1}}^{t_j} g(t) \; \mathrm{d}t, \tag{2.19}$$

https://doi.org/10.1017/jfm.2026.11913 Published online by Cambridge University Press

where x_j is the tracked position at time t_j. The switch functions are linear combinations of a set of so-called 'support functions':

$$\varphi_j(t) = \sum_{i=1}^{n_c} s_i(t)\, A_{ij}, \tag{2.20}$$

where s_i is the ith support function and A_{ij} is a weighting coefficient. The switch functions must successively activate the integral constraints over the corresponding intervals, which amounts to the condition

$$\int_{t_{i-1}}^{t_i} \varphi_j(t)\, \mathrm{d}t = \begin{cases} 1, & i = j \\ 0, & i \neq j \end{cases} \quad \text{for} \quad i, j \in \{1, \ldots, n_c\}. \tag{2.21}$$

Enforcing this condition is equivalent to solving the linear system

$$\boldsymbol{SA} = \boldsymbol{I}, \tag{2.22}$$

where $\boldsymbol{S}$ is an $n_c \times n_c$ matrix with entries

$$S_{ij} = \int_{t_{i-1}}^{t_i} s_j(t)\ \mathrm{d}t \tag{2.23}$$

and $\boldsymbol{I}$ is the identity matrix. The support functions s_j must yield a non-singular matrix $\boldsymbol{S}$ but are otherwise flexible. While Leake *et al.* (2022) suggested monomials (e.g. $s_j(t) = t^{j-1}$), the resulting KCT model becomes ill-conditioned for long tracks. Instead, we use radial basis functions:

$$s_j(t) = \exp\Big[-\beta_j^2 \left(t - t_{0,j}\right)^2\Big], \tag{2.24}$$

with $\beta_j = (t_j - t_{j-1})^{-1}$ and where $t_{0,j} = (t_{j-1} + t_j)/2$ is the midpoint for the jth interval.

Given a set of support functions, the coefficient matrix $\boldsymbol{A}$ is determined by solving (2.22), which may be done independently of the free function g and its parameters. Conversely, the projection coefficients η_j explicitly depend upon the polynomial parameters θ_i through (2.19). Substituting the polynomial form of g from (2.18) yields a closed-form expression for the projection coefficients:

$$\eta_j = \left(x_j - x_{j-1}\right) - \sum_{i=0}^{P} \frac{\theta_i}{i+1} \left(t_j^{i+1} - t_{j-1}^{i+1}\right), \tag{2.25}$$

where t_j^{i+1} is time t_j raised to the $(i+1)$th power.

For ease of implementation, it is convenient to recast (2.17) in matrix form. We thus define a series of entities: a parameter vector $\boldsymbol{\theta} = \{\theta_0, \ldots, \theta_P\}$, time vector $\boldsymbol{\tau}_v(t) = \{t^j \mid j = 0, \ldots, P\}$, displacement vector $\boldsymbol{\delta} = \{x_j - x_{j-1} \mid j = 1, \ldots, n_c\}$, support-function vector $\boldsymbol{s}_v(t) = \{s_j(t) \mid j = 1, \ldots, n_c\}$ and $(P+1) \times n_c$ support matrix $\boldsymbol{C}$, with entries

$$C_{ij} = i^{-1}\left(t_j^i - t_{j-1}^i\right). \tag{2.26}$$

Using these definitions, the KCT velocity model can be written compactly as

$$v(t) = \boldsymbol{\theta}^\top \boldsymbol{\tau}_v(t) + \left(\boldsymbol{\delta}^\top - \boldsymbol{\theta}^\top \boldsymbol{C}\right) \boldsymbol{A}^\top \boldsymbol{s}_v(t). \tag{2.27}$$

This representation, which is one component of P for a single particle, provides a continuous, differentiable velocity profile that inherently satisfies the advection constraint.

https://doi.org/10.1017/jfm.2026.11913 Published online by Cambridge University Press

The displacement vector $\boldsymbol{\delta}$ encodes the measured particle positions. For noisy tracks, however, the positions in $\boldsymbol{\delta}$ can be adjusted during training alongside $\boldsymbol{\theta}$, enabling refinement of particle positions at measurement times.

Integration and differentiation of the velocity model yield continuous expressions for the particle's position and acceleration. The position is

$$x(t) = \boldsymbol{\theta}^\top \boldsymbol{\tau}_x(t) + \left(\boldsymbol{\delta}^\top - \boldsymbol{\theta}^\top \boldsymbol{C}\right) \boldsymbol{A}^\top \boldsymbol{s}_x(t) + x_0, \tag{2.28}$$

where x_0 is the initial position of the chosen track component. The acceleration is

$$a(t) = \boldsymbol{\theta}^\top \boldsymbol{\tau}_a(t) + \left(\boldsymbol{\delta}^\top - \boldsymbol{\theta}^\top \boldsymbol{C}\right) \boldsymbol{A}^\top \boldsymbol{s}_a(t). \tag{2.29}$$

As in (2.27), all time dependencies are carried by the $\boldsymbol{\tau}$ and $\boldsymbol{s}$ vectors. For position, these are

$$\boldsymbol{\tau}_x(t) = \left\{ t^{j+1}/(j+1) \;\middle|\; j = 0, \ldots, P \right\} \tag{2.30a}$$

and

$$\boldsymbol{s}_x(t) = \left\{ \frac{\sqrt{\pi}}{2\,\beta_j} \operatorname{erf}\left[\beta_j \left(t - t_{0,j}\right)\right] \;\middle|\; j = 1, \ldots, n_c \right\}, \tag{2.30b}$$

and for acceleration, they are

$$\boldsymbol{\tau}_a(t) = \left\{ j\, t^{j-1} \;\middle|\; j = 0, \ldots, P \right\} \tag{2.30c}$$

and

$$\boldsymbol{s}_a(t) = \left\{ -2\,\beta_j^2 (t - t_{0,j})\, s_j(t) \;\middle|\; j = 1, \ldots, n_c \right\}. \tag{2.30d}$$

It should be emphasised that while the KCT model enforces particle kinematics as a hard constraint, the dynamics emerges through the joint optimisation of F and $\mathsf{P}^{(k)}$ by minimisation of the particle physics loss in (2.4). For any prescribed set of positions, the KCT admits many velocity histories, as illustrated in figure 2. Accordingly, the free parameters $\boldsymbol{\theta}$ and $\boldsymbol{\delta}$ must be identified from the interplay of physics and data losses. In cases involving inertial transport with particles of unknown size, density or other properties, the kinematic parameters alone are insufficient. Additional training variables associated with the relevant particle dynamics (diameter d_p, density ρ_p, etc.) must be included in the optimisation.

2.4.1. *Comparison to alternative track models*

Track processing for LPT generally falls into two categories: filtering and optimisation. In filtering methods, the particle position time series is differentiated and smoothed by convolving the raw trajectories with a discrete kernel. Velocities and accelerations are estimated at the measurement times. The simplest example is finite differencing, which amplifies noise. For this reason, low-pass filtering is commonly introduced, with Gaussian kernels being a standard choice (Mordant *et al.* 2004; Berk & Coletti 2021; Will *et al.* 2021; Brandt & Coletti 2022). These methods are simple and computationally efficient, but they suffer from large endpoint errors due to the asymmetric support of the stencil. Berk (2024) found that Gaussian smoothing requires kernels with 20 points or more to perform well, which effectively removes 10 points from each end of a track. Short tracks may then be discarded entirely, introducing a potential selection bias, since tracks associated with larger velocities and accelerations are often the shortest ones (Lawson *et al.* 2018).

https://doi.org/10.1017/jfm.2026.11913 Published online by Cambridge University Press

In optimisation methods, including our KCT approach, an analytical function is fitted to the raw trajectories, thereby providing a continuous representation in time and avoiding the worst of the endpoint issue. Early techniques in this class represented tracks using low-order polynomials (Malik *et al.* 1993; Voth *et al.* 2002; Di Leoni *et al.* 2023); these models were typically under-parametrised and optimised by least squares (Lynch & Scarano 2013). Such models inherently suppress noise, but they can also smooth out *bona fide* fluctuations. More recently, spline-based models have become prominent, with TrackFit as a notable example (Gesemann *et al.* 2016; Gesemann 2021; Buchwald *et al.* 2025). In that method, each trajectory is represented by an over-parametrised B-spline. Regularisation is supplied by a third-order smoothness penalty, and the weighting parameter is selected so as to balance realistic spectral characteristics against the suppression of noise. See Gesemann (2021) for a full description.

In a similar spirit, KCTs also over-parametrise each track and yield a continuous, differentiable representation of the trajectory. We do not claim that KCTs confer a theoretical advantage over spline-based methods. Rather, we have simply found that the KCT formulation performs well across all of our tests, being easy to initialise and sample and well conditioned in the joint optimisation. More broadly, the main point of the present work is not the use of KCTs *per se*, but the use of parametrised tracks within a physics-constrained reconstruction, which amounts to a form of physics-informed particle tracking. A similar approach could be implemented using the B-splines of TrackFit or other smooth track models.

3. Flow cases and datasets

We investigate the joint estimation problem using three flow configurations: a TBL, forced HIT and supersonic flow over a cone–cylinder body. These are referred to as the TBL, HIT and cone cases, respectively, and they are introduced below in the order in which they appear in the paper. First, in the TBL case, we estimate true tracer trajectories from noisy data, corresponding to physics-informed tracking in the $St \to 0$ limit. Second, in the HIT and cone–cylinder cases, we estimate inertial particle properties for particles with finite St and Re_p. Third, in the HIT case, we jointly estimate particle positions and sizes from noisy tracks to assess the interaction between noise and inertia. Each dataset mimics realistic LPT conditions in terms of particle densities and tracking accuracy.

3.1. *Turbulent boundary layer with noisy particle tracks*

The first case is drawn from a DNS of channel flow with a favourable pressure gradient, obtained from the Johns Hopkins Turbulence Database (JHTDB) (Perlman *et al.* 2007). An imposed pressure gradient drives the development of TBLs along the top and bottom walls, with friction Reynolds numbers up to $Re_\tau \approx 1000$. The DNS domain spans $8\pi \times 3\pi \times 2$ and is discretised with $2048 \times 1536 \times 512$ voxels in the streamwise, spanwise and wall-normal directions, and the data are stored at a dimensionless temporal resolution of 0.0065. Our study focuses on a $(126 \times 54 \times 80)$-voxel subvolume at the bottom wall, corresponding to a physical region of $56 \times 12 \times 4.25$ mm^3 (air, $\nu = 15$ mm^2 s^{-1}). In viscous units, this region spans $1546 \times 331 \times 117$ and covers the buffer layer. The viscous length and time scales are $\ell_\nu = 0.036$ mm and $\tau_\nu = 0.09$ ms, respectively.

Synthetic LPT data are generated by advecting 70 000 ideal tracers, yielding a particle image density of 0.07 particles per pixel (ppp) for a 1 MP camera. This lies squarely within the capability of standard multi-camera STB workflows (which extend to about 0.1 ppp; Schanz *et al.* 2016) and slightly above the typical range reported for single-camera techniques such as DIH and plenoptic LPT (0.03–0.06 ppp; Shao *et al.* 2020;

https://doi.org/10.1017/jfm.2026.11913 Published online by Cambridge University Press

Yamakaitis *et al.* 2025*b*). Advection is performed with a fourth-order Runge–Kutta scheme and periodic boundary conditions. To mitigate boundary-related artefacts, the tracks are first computed in an extended outer domain and then cropped to an inner region that is 15 % smaller in each direction. Tracks are 'recorded' for 51 consecutive frames at a temporal resolution of 0.057 ms. The mean particle spacing is about $9\ell_\nu$, which is sufficient to resolve most of the flow's energy content using PINNs. The particle field is downsampled by factors of 8 and 64 to produce datasets with lower seeding densities, having mean inter-particle spacings of $18\ell_\nu$ and $36\ell_\nu$.

To simulate experimental localisation errors, the ground-truth particle positions are corrupted with random noise drawn from the error probability density function (PDF) reported for iterative particle reconstruction at 0.1 ppp (Wieneke 2012; Schanz *et al.* 2022). A range of localisation uncertainties is considered, with standard deviations of $\sigma_x = \sigma_y \in \{0.05, 0.15, 0.25, 0.35, 0.45, 0.5\}$ in pixel units in the x–y plane. In viscous units, this corresponds to $0.09\ell_\nu$–$0.9\ell_\nu$. To reflect the anisotropy commonly observed in experiments, the wall-normal noise is taken to be twice as large as the other components, with $\sigma_z/\sigma_x = 2$, under the assumption that the z axis coincides with the optical axis. This ratio is broadly consistent with STB and with advanced DIH and plenoptic techniques. For example, Shao *et al.* (2020) developed a deep learning method for DIH–LPT that reduced the positional uncertainty ratio to $\sigma_z/\sigma_x = 2$–4, and Moaven *et al.* (2024) proposed a ray-bundling method that achieved a ratio of about 3 for plenoptic LPT. By contrast, when processed using conventional numerical refocusing, low-aperture LPT methods can exhibit much larger anisotropy ratios, often up to 10. In previous work, we showed that DA can compensate for such issues (Zhou *et al.* 2023, 2024), but a comprehensive study of noise distributions is outside the scope of the present paper.

The selected localisation noise levels span a broad range of measurement conditions. Low noise levels, with $\sigma_x \leq 0.15$ px, roughly correspond to multi-camera STB (Schanz *et al.* 2016), whereas high noise levels, with $\sigma_x \geq 0.35$ px, are consistent with low-aperture single-camera systems (Mallery & Hong 2019; Moaven *et al.* 2024; Yamakaitis *et al.* 2024*b*). At the high end of this range, recent campaigns using DIH and plenoptic LPT to measure turbulent flows have reported particle image densities and extraction rates similar to those considered here. For instance, deep learning methods for DIH–LPT can achieve extraction rates up to 95 % at seeding densities reaching 0.06 ppp (Shao *et al.* 2020). Likewise, the plenoptic LPT algorithm of Moaven *et al.* (2024) extracts more than 90 % of particles at seeding densities up to 0.06 particles per microlens (analogous to ppp for plenoptic imaging), although a larger sensor would be required to recover the same number of particles in a plenoptic configuration. Other sources of error, such as ghost particles and broken tracks, are not considered here because modern processing methods have been shown to suppress most such artefacts (Schanz *et al.* 2016; Mallery *et al.* 2020).

The TBL case is specifically designed to reproduce the conditions of a recent LPT experiment conducted by Schröder *et al.* (2024, 2025). In it, a TBL with $Re_\tau \approx 995$ was measured in a near-wall region of size $60 \times 12 \times 2$ mm^3. Particle images were captured by five high-speed cameras at a temporal resolution of 0.042 ms, with a particle image density of 0.06–0.07 ppp for a 2048×512 pixel sensor. The flow properties and acquisition parameters in this experiment closely match those of our synthetic case, which features a slightly larger domain ($56 \times 12 \times 4.25$ mm^3) and lower temporal resolution (0.057 ms), thereby posing a somewhat harder reconstruction problem. Similar near-wall measurements have also been performed using low-aperture imaging systems (Yamakaitis *et al.* 2024*a*, 2025*a*). Given this experimental backdrop, we use the TBL case to address our first question: can noisy tracks, when coupled with flow physics constraints and a

https://doi.org/10.1017/jfm.2026.11913 Published online by Cambridge University Press

localisation error PDF, support accurate reconstruction of both the flow field and the true tracer trajectories?

3.2. *Homogeneous isotropic turbulence with bidisperse inertial particles*

The second case is based on a DNS of forced incompressible HIT, also taken from the JHTDB. Inertial particle transport in HIT has been studied extensively, both numerically (Eaton 2009; Rosa *et al.* 2016) and experimentally (Petersen *et al.* 2019; Ferran *et al.* 2023), making it a suitable numerical testbed for evaluating the joint estimation problem. The selected JHTDB dataset has a Taylor-scale Reynolds number of $Re_\lambda = 433$ and is simulated in a periodic domain of size $2\pi \times 2\pi \times 2\pi$, which is discretised into 1024^3 voxels. We focus on the central 128^3-voxel subvolume, spanning 100 frames at a dimensionless temporal resolution of 0.002. To mimic laboratory conditions, the data are dimensionalised assuming air as the carrier fluid, giving a physical volume of 10^3 cm^3, a measurement duration of 0.04 s and a sampling rate of 2500 Hz. The Taylor and Kolmogorov length scales are $\ell_\lambda = 14.38$ mm and $\ell_\eta = 0.35$ mm, with corresponding time scales of $\tau_\lambda = 31.9$ ms and $\tau_\eta = 8.2$ ms.

Particle tracks are generated by simulating 50 000 spherical soda-lime glass beads of density $\rho_p = 2500\ \mathrm{kg\,m^{-3}}$. Diameters are drawn from two Gaussian distributions, one with mean 32 μm and standard deviation 2 μm, and the other having mean 73 μm and standard deviation 4 μm, with equal sampling from each distribution. The resulting particle field has a volume fraction of 3.4×10^{-6} and a mass loading of 6.9×10^{-3}, placing it near the upper boundary of the one-way-coupled regime (Elghobashi 1994; Brandt & Coletti 2022). The corresponding Stokes numbers, based on τ_η and τ_p, are approximately 1 and 5, indicating substantial inertial lag and clustering (Samimy & Lele 1991). Particle dynamics is governed by the Maxey–Riley equation (Maxey *et al.* 1997), which applies to small spherical particles in the one-way-coupled regime, together with a Schiller–Naumann drag correction that is valid for $Re_p < 800$ (Schiller 1933). Here, the maximum particle Reynolds number is about 6.5. Following Eaton (2009) and Ling *et al.* (2013), the Basset history force is neglected. Trajectories are integrated using a second-order Runge–Kutta scheme (we use a second-order Runge–Kutta scheme to preserve the native temporal resolution of the DNS data; at the time steps used here, it yields nearly identical particle positions to a fourth-order scheme) with periodic boundaries applied at the periphery of an extended domain (150 voxels). The simulation is run for 201 frames to minimise initialisation and boundary artefacts. Reconstructions are performed for the 128^3-voxel subvolume over the final 100 frames at a temporal resolution of 0.4 ms. On average, 33 000 particles occupy the probe volume at any instant, corresponding to 0.033 ppp for a 1 MP camera. Once again, this seeding level lies comfortably within the capability of leading LPT techniques (Schröder & Schanz 2023). The mean inter-particle spacing is approximately $8.9\ell_\eta$ or $0.216\ell_\lambda$, which is low enough for joint reconstruction (see § 7.1).

The configuration of this case is motivated by extensive experimental studies of inertial particle dynamics in HIT. A pertinent example is the work of Petersen *et al.* (2019), who investigated particle clustering and settling dynamics in HIT at $Re_\lambda \approx 200$–500. In that study, sub-Kolmogorov inertial particles ($d_p = 30$–90 μm) exhibited Stokes numbers of order 1–10; the carrier fluid was simultaneously seeded with 1–2 μm diethylhexyl sebacate tracers having negligible Stokes numbers. A single imaging system was used to perform simultaneous planar PIV and LPT, with intensity-based image processing used to segregate the tracers and inertial particles. This enabled detailed analysis of particle–flow interactions, including preferential sampling of high-strain/low-vorticity regions and turbulence modulation. The same facility was later used at comparable Re_λ and St to

https://doi.org/10.1017/jfm.2026.11913 Published online by Cambridge University Press

study conditional Lagrangian statistics of inertial particles (Berk & Coletti 2021) and slip velocities (Berk & Coletti 2024). Although the flow and particle parameters in these studies are broadly comparable to the present case, the planar nature of the measurements can bias trajectory sampling (Berk & Coletti 2021). Extending such measurements to three dimensions would alleviate this issue, but doing so whilst tracking both tracer and inertial particles would restrict the admissible concentration of the latter. Moreover, optical segregation of tracers and inertial particles becomes quite difficult for smaller particles, e.g. towards $St \sim 1$, where phenomena such as inertial clustering (Wang & Maxey 1993; Petersen *et al.* 2019) and gravitational settling (Aliseda *et al.* 2002; Rosa *et al.* 2016) are especially pronounced.

Such limitations could, in principle, be addressed by joint estimation, in which time-resolved 3-D flow fields and particle characteristics are inferred solely from inertial track data. Ideally, no additional seeding of tracers would be required to measure the carrier phase, nor would image-based phase segregation be needed, thereby permitting measurements of denser inertial particle fields. The present HIT case therefore allows us to assess whether inertial particle trajectories, themselves, contain enough information to support joint recovery of the flow field and unknown particle properties.

3.3. *Supersonic cone–cylinder flow with inertial particle transport*

The third case involves a steady compressible axisymmetric flow at Mach 2 over a 15° half-angle cone–cylinder body, generating an oblique shock wave at the nose and an expansion fan over the shoulder. The inflow density and temperature are 0.55 kg m^{-3} and 166.7 K, and the cylinder radius is 20 mm, consistent with the experiments of Venkatakrishnan & Meier (2004). The flow is simulated with the compressible, axisymmetric Navier–Stokes solver in SU2 7.3.0. The computational domain spans a radius of 0.15 m and a length of 0.25 m, with $\gamma = 1.4$. For reference, the free-stream velocity is $U_\infty \approx 520$ m s^{-1} and the cone length is 40 mm, leading to a characteristic Reynolds number of $Re \sim 10^6$. Viscous scales for this flow are of the order of a micrometre in length and tens of nanoseconds in time, and the physical shock thickness is likewise submicrometric, i.e. well below both the resolution of the CFD grid and that of present LPT scenario. Nevertheless, particle tracks throughout the domain provide physical anchors for DA reconstruction. Further details on the mesh, solver settings and experimental validation are reported by Molnar *et al.* (2023).

Particle tracks are simulated for 2000 solid spherical particles, modelled as agglomerated TiO_2 seed. Diameters are drawn from a Gaussian distribution with mean $d_p = 2$ µm and standard deviation 0.5 µm, and densities from a Gaussian distribution with mean $\rho_p = 950$ kg m^{-3} and standard deviation 100 kg m^{-3}; these values were obtained from the calibration measurements of Williams *et al.* (2015). The resulting mean response time is $\tau_p \approx 20$ µs, which implies appreciable lag through the shock wave and expansion fan. The particle volume fraction and mass loading for this scenario are 10^{-9} and 10^{-6}, respectively, lying well within the one-way-coupled regime (Brandt & Coletti 2022). Particle transport is computed using a compressible drag law (see Appendix B.3); the particles are injected at the entrance of the computational domain at the free-stream velocity and advected downstream with periodic reinjection.

This case is intentionally idealised with respect to the measurement configuration and conservative with respect to the particle dynamics. The synthetic tracks are generated for eight frames at an implied imaging rate of 0.5 MHz. This frame rate, and the eight-pulse LPT configuration, lie near the boundary of what is currently possible in high-speed aerodynamic measurements, for which double-frame PIV remains the standard approach

https://doi.org/10.1017/jfm.2026.11913 Published online by Cambridge University Press

(Beresh 2021). Nevertheless, recent work has begun to extend multi-pulse LPT into this regime (Novara *et al.* 2019; Manovski *et al.* 2021), and such developments may ultimately enable LPT-based interrogation of high-speed flows. The particle properties, by contrast, correspond to a relatively unfavourable seeding condition. The resulting test therefore asks whether joint estimation remains useful when high-speed LPT data are available but particle filtering remains significant. Although we consider only the mean flow in this case, the characteristic time scales of turbulent fluctuations are much shorter than those associated with mean velocity gradients. As a result, effective Stokes numbers in real experiments on unsteady high-speed flows may be comparable to those tested here, even for tracers with much faster response times.

As mentioned above, shorter response times than those reported by Williams *et al.* (2015) have indeed been achieved for TiO_2 seed. For example, Urban & Mungal (2001) reported response times of 3–4 μs for TiO_2 particles from oblique-shock tests in supersonic shear layers, and Scarano & van Oudheusden (2003) determined relaxation times below 2 μs. Ragni *et al.* (2011) further developed specialised seeding and calibration procedures and reported typical response times of 2.5–3.25 μs for TiO_2, reducing the response time to as little as 0.5 μs through dehydration, a custom cyclone seeder and a 1 μm particle filter. Such measures may be necessary to ensure adequate traceability, although the particle filter in particular was reported to substantially reduce the number of particles delivered to the probe volume. In light of these studies, the calibration data of Williams *et al.* (2015) are likely associated with agglomerated seed. The present cone case thus provides a conservative test of whether joint estimation can compensate for non-ideal tracer behaviour without *a priori* knowledge of the particle response. We note again that the filtering effect associated with $\tau_p \approx 20$ μs tracers in steady flow may be viewed as a proxy for effect of very agile tracers when resolving turbulent fluctuations in high-speed flows, for which effective values of St can be high. For completeness, we also consider a lower-inertia case with $\tau_p = 3.1$ μs in Appendix D.

3.4. *Homogeneous isotropic turbulence with varying inertial particles and noise*

Lastly, we extend the HIT case from § 3.2 to establish how localisation uncertainty and inertial effects interact when jointly determining flow fields and particle properties. We use the central 64^3-voxel subdomain of the HIT dataset while keeping the temporal resolution, number of frames and advection schemes unchanged. A dense field of 6600 particles is first simulated and then downsampled by factors of 2^N, for $N \in \{1, \ldots, 6\}$, producing seeding densities with inter-particle spacings from $7.3\ell_\eta$ to $29.3\ell_\eta$. The particle density is increased from 2500 kg m^{-3} in § 3.2 to 6000 kg m^{-3}, and diameters are drawn from a Gaussian distribution with mean 33 μm and standard deviation 4 μm. This ensures one-way coupling, even at the densest seeding condition. The mean Stokes number is 3, and no localisation error is applied at this stage.

We then vary the localisation error and Stokes number independently. A total of 3300 particles are simulated, giving a mean spacing of $9.2\ell_\eta$, sufficient for a scale-resolving reconstruction in the tracer limit. Particle densities are then adjusted to set $St \in \{1, \ldots, 5\}$ via $\rho_p = 2000St$ kg m^{-3}; diameters are fixed to avoid the two-way-coupled regime. The clean tracks are corrupted with additive Gaussian noise, with $\sigma_x = \sigma_y \in \{0.1, \ldots, 0.5\}$ in pixel units, assuming a 1 MP camera. Similar to § 3.1, the lowest level ($\sigma_x = 0.1$ px) corresponds to STB accuracy in ideal laboratory conditions (Schanz *et al.* 2016). Once again, to mimic anisotropy, the magnitude of wall-normal noise is doubled ($\sigma_z/\sigma_x = 2$). These settings yield 25 cases spanning a matrix of localisation errors and Stokes numbers.

https://doi.org/10.1017/jfm.2026.11913 Published online by Cambridge University Press

Case	Flow model	Layers × neurons
TBL	$\mathsf{F}_{\boldsymbol{u}} : (\boldsymbol{x}, t) \mapsto \boldsymbol{u}$	10×300
	$\mathsf{F}_{p} : (\boldsymbol{x}, t) \mapsto p$	10×150
HIT	$\mathsf{F}_{\boldsymbol{u}} : (\boldsymbol{x}, t) \mapsto \boldsymbol{u}$	15×300
	$\mathsf{F}_{p} : (\boldsymbol{x}, t) \mapsto p$	15×150
Cone	$\mathsf{F}_{(\rho,\boldsymbol{u},T)} : \boldsymbol{x} \mapsto (\rho, \boldsymbol{u}, T)$	10×250

Table 1. Network architectures used for the flow models (velocity, pressure or full primitive state) in the three test cases.

4. Implementation of the method and evaluation metrics

4.1. *Neural network architectures*

We implement NIPA in TensorFlow 2.10. Exact partial derivatives of the model outputs with respect to $\boldsymbol{x}$ and t, and derivatives of the loss function with respect to the model parameters, are computed using automatic differentiation. The integrals over $\mathcal{V}$, $\mathcal{A}$ and $\mathcal{T}$ in (2.7)–(2.10) are approximated by Monte Carlo sampling. At each training step, the probe volume is sampled with a batch of 5000 points drawn uniformly from $\mathcal{V}$, and the boundary loss is evaluated using 1000 points drawn uniformly from $\mathcal{A}$. For the particles, 5000 tracks are sampled at each iteration, and eight random times are drawn for each track; the first and last times are also included to suppress boundary inflections, culminating in a particle batch size of 50 000 points.

The network architectures are tailored to the complexity of each flow case, with the corresponding parameters listed in table 1. Flow models and submodels are denoted by F, with subscripts indicating the target fields, e.g. $\mathsf{F}_{\boldsymbol{u}}$ and F_{p} represent neural models of the velocity and pressure fields, respectively. All the networks employ a Fourier encoding layer (see § 2.3), with frequency vectors $\boldsymbol{f}_i$ drawn from a standard Gaussian distribution for spatial features and from a zero-mean Gaussian distribution with a standard deviation of 0.2 for temporal features. The number of features is fixed at 1024. This choice provides sufficient expressivity for all the flow cases. We tested networks with 128, 256, 512 and 1024 Fourier features and found that the accuracy of the learned fields saturated before 1024 features, with little additional computational cost incurred between 512 and 1024. An assessment of the the networks' representational power is provided in Appendix E.

4.2. *Model initialisation strategy*

Initialisation of the flow model is straightforward: the network weights are drawn from a standard normal distribution and the biases are set to zero. Initialisation of the KCTs proceeds in three steps. First, long tracks are split into shorter segments to reduce computational costs and keep the associated matrix operations manageable; guidelines for selecting an appropriate segment length are provided in Appendix F.1. Second, for ideal tracers, the particle displacements $\boldsymbol{\delta}$ are directly initialised from the raw (noisy) track data, while the polynomial coefficients in $\boldsymbol{\theta}$ are set to zero. We refer to this as a cold start since it requires no prior information. Conversely, inertial tracks are warm-started using filtered track data to aid convergence. This is necessary because additional unknowns, such as particle diameters and densities, are inferred in the inertial cases, making the inverse problem more ill-posed. Warm-started KCTs thus inherit both the regularity and the bias of the chosen filter, which is a necessary trade-off for stable optimisation. Finally, all trainable parameters are normalised to be of order unity. This allows for particle

https://doi.org/10.1017/jfm.2026.11913 Published online by Cambridge University Press

quantities with different units and scales to be trained together using a single learning rate. Appendix F.2 provides details of the warm-start procedure, and Appendix F.3 describes the normalisation and parameter selection strategy.

4.3. *Training procedure*

Flow and KCT models are trained together by minimising $\mathscr{J}_{total}$. The weighting coefficients for each loss term χ_i are chosen through a simple parameter sweep, in which reconstructions are performed for different values of χ_i. We found that accuracy is relatively insensitive to χ_i near the optimum. Training is performed using the Adam optimiser, with the learning rate for flow networks fixed at 10^{-3}. For particle models, the learning rate is annealed from 10^{-4} to 10^{-5} and finally to 10^{-6} to improve precision. All cases are trained to convergence, typically requiring about 2000 epochs per learning rate. Computations are performed on an NVIDIA RTX A6000 GPU with 48 GB of onboard memory. The total wall-clock training time is approximately 25 hours for the TBL cases, 15 hours for the HIT cases and 3 hours for the cone case.

More advanced neural architectures and optimisation strategies may further improve DA performance. Examples include nonlinear residual layers such as PirateNet (Wang *et al.* 2024), multi-stage networks designed to better capture multi-scale features (Wang & Lai 2024), quasi-second-order optimisers like SOAP (Wang *et al.* 2025) and automatic loss-weighting methods (Wang *et al.* 2022). Incorporating such techniques could improve both reconstruction accuracy and training efficiency in future studies.

4.4. *Error metrics and spectral resolution*

Reconstruction accuracy is evaluated using global and spectral error metrics. For a field variable φ, the normalised root-mean-square error (NRMSE) is

$$e_\varphi = \left(\frac{\left\langle \|\varphi - \varphi_{exact}\|_2^2 \right\rangle}{\left\langle \|\varphi_{exact}\|_2^2 \right\rangle} \right)^{1/2}, \tag{4.1}$$

where φ_{exact} is the ground truth. The averaging operator $\langle\cdot\rangle$ may be taken either over the spatio-temporal domain,

$$\langle\varphi\rangle_{\mathcal{V}\times\mathcal{T}} = \frac{1}{|\mathcal{V}\times\mathcal{T}|}\int_{\mathcal{T}}\int_{\mathcal{V}} \varphi(\boldsymbol{x},t)\ \mathrm{d}\boldsymbol{x}\,\mathrm{d}t, \tag{4.2}$$

or across the tracks,

$$\langle\varphi\rangle_p = \frac{1}{n_p}\sum_{k=1}^{n_p}\frac{1}{|\mathcal{T}^{(k)}|}\int_{\mathcal{T}^{(k)}}\varphi(t)\,\mathrm{d}t. \tag{4.3}$$

In practice, these integrals are approximated by sums over DNS grid points and time steps for flow fields, and over discrete measurement instants in $\mathcal{T}^{(k)}$ for tracks. In the unsteady flow cases, we report errors for the fluctuating component φ', defined by a Reynolds decomposition $\varphi = \overline{\varphi} + \varphi'$. This yields a conservative estimate of reconstruction accuracy, since mean fields are easier to recover than turbulent fluctuations. In the steady cone flow case, errors are reported for the primitive fields without modification.

Spectral error analysis quantifies reconstruction accuracy across wavenumbers. The spherical averaging operator in Fourier space is

$$\langle\widetilde{\varphi}\rangle_\kappa = \int_{\mathcal{K}(\kappa)}\widetilde{\varphi}(\boldsymbol{\kappa})\ \mathrm{d}\boldsymbol{\kappa}, \tag{4.4}$$

https://doi.org/10.1017/jfm.2026.11913 Published online by Cambridge University Press

where $\widetilde{\varphi}$ is the 3-D Fourier transform of φ and $\mathcal{K}(\kappa)$ is a shell of radius κ. In practice, the integration is approximated by averaging Fourier magnitudes within discrete shells of width $\Delta\kappa$. For velocity fields, the turbulent kinetic energy (TKE) spectrum is computed using (4.4) for $\varphi = \boldsymbol{u} \cdot \boldsymbol{u}/2$. Normalised velocity error spectra are then given by

$$e_{\widetilde{\boldsymbol{u}}}(\kappa) = \left(\frac{\left\langle \|\widetilde{\boldsymbol{u}} - \widetilde{\boldsymbol{u}}_{exact}\|_2^2 \right\rangle_\kappa}{\left\langle \|\widetilde{\boldsymbol{u}}_{exact}\|_2^2 \right\rangle_\kappa} \right)^{1/2}. \tag{4.5}$$

This spectrum measures the energy of velocity reconstruction errors relative to the true turbulent energy at each wavenumber. A key reference point for interpreting these spectra is the particle sampling Nyquist wavenumber:

$$\kappa_{Nyq} = \frac{\pi}{\delta}, \tag{4.6}$$

where δ is the mean inter-particle spacing. Note that κ_{Nyq} represents the highest resolvable wavenumber from interpolation of the particle velocities, alone. In the absence of physics-based constraints, error levels beyond this limit are expected to saturate at 100 %.

5. Joint estimation of flow fields and particle positions

We firstly examine the TBL case, in which the particle tracks correspond to ideal tracers. Because trajectory estimation is the first step in LPT workflows, we begin in § 5.1 by comparing several track processing methods applied directly to noisy LPT data, including finite differencing, B-splines with a fixed length, TrackFit and KCTs trained without a physics loss. We then compare these results with the track estimates produced by our joint reconstruction procedure.

Next, we examine flow-field reconstructions in § 5.2. Specifically, we compare baseline reconstructions, produced using the track-only kinematics, with the results of joint estimation. By varying the seeding density and magnitude of localisation error, we assess how track density and track quality affect both stages of the reconstruction problem.

5.1. *Particle track optimisation*

We process datasets with three seeding densities, corresponding to mean particle spacings of $\delta = 9\ell_\nu$, $18\ell_\nu$ and $36\ell_\nu$, where ℓ_ν is the friction length. We also consider six localisation error levels, with $\sigma_x \in \{0.09, 0.27, 0.45, 0.63, 0.81, 0.9\}\ell_\nu$. Five approaches are used to estimate the tracks. First, we present the raw tracks, with velocities obtained by finite differencing. Second, we apply a B-spline filter, described in Appendix C, with the segment length tuned in a supervised manner to minimise error across all the datasets. Third, we use TrackFit (Gesemann *et al.* 2016; Gesemann 2021), which also represents trajectories with B-splines and approximates an optimal Wiener filter. Specifically, we use the advanced TrackFit variant of Buchwald *et al.* (2025), wherein the weights are adapted from local track statistics to improve performance in inhomogeneous flows. Fourth, we train KCT models using the data loss in isolation. These four approaches rely solely on measurement data and do not incorporate any flow physics information. For our fifth and final approach, we train KCTs jointly with the flow model using the combined data, flow physics, particle physics and boundary losses. This final setting embeds physical constraints and therefore indicates the extent to which such coupling improves track accuracy. Below, these five datasets are labelled raw, filtered, TrackFit, KCT (i.e. data only) and joint estimation.

https://doi.org/10.1017/jfm.2026.11913 Published online by Cambridge University Press

Noise level	Raw	Filtered	TrackFit	KCT	Joint estimation		
					$\delta = 9\ell_\nu$	$\delta = 18\ell_\nu$	$\delta = 36\ell_\nu$
	0.09	0.08	**0.04**	0.13	**0.04**	0.05	0.05
0.05 px	0.11	0.07	0.04	0.17	**0.03**	0.04	0.05
	0.14	0.07	0.04	0.30	**0.03**	**0.03**	0.05
	0.27	0.16	**0.12**	0.38	**0.12**	0.13	0.14
0.15 px	0.24	0.11	0.08	0.34	**0.06**	0.08	0.10
	0.32	0.10	0.05	0.35	**0.03**	0.04	0.07
	0.45	0.24	0.18	0.63	**0.17**	0.20	0.21
0.25 px	0.37	0.15	0.10	0.53	**0.07**	0.09	0.13
	0.50	0.14	0.06	0.65	**0.03**	0.04	0.07
	0.63	0.33	0.24	0.88	**0.23**	0.26	0.29
0.35 px	0.49	0.20	0.13	0.72	**0.09**	0.12	0.16
	0.67	0.19	0.07	0.82	**0.04**	0.05	0.09
	0.81	0.42	0.31	1.14	**0.28**	0.33	0.36
0.45 px	0.62	0.26	0.16	0.92	**0.09**	0.13	0.17
	0.84	0.24	0.08	1.20	**0.03**	0.06	0.11
	0.90	0.47	0.34	1.26	**0.30**	0.38	0.40
0.5 px	0.71	0.28	0.17	1.04	**0.10**	0.15	0.18
	0.97	0.26	0.09	1.29	**0.04**	0.05	0.12

Table 2. Standard deviations of track errors in the x direction for varying noise levels. At each level, the three sub-rows correspond to the position, velocity and acceleration errors, normalised by the friction length ℓ_ν, velocity v_ν and acceleration v_ν^2/ℓ_ν, respectively. The lowest error in each row is shown in bold.

Tables 2 and 3 report the error standard deviations in the x and z directions; statistics for the x and y directions are nearly identical. Finite differencing amplifies positional errors into very noisy velocity and acceleration estimates. B-spline filtering, by contrast, suppresses these errors by factors of two or more, consistent with the findings of Li & Pan (2024). TrackFit further improves upon the B-spline results by adapting its filter parameters from the position amplitude spectra of local track statistics (Buchwald *et al.* 2025). Data-only KCTs perform worse than the raw tracks because the data loss merely enforces statistical consistency with the assumed localisation uncertainty. The resulting optimisation is therefore highly ill-posed because infinitely many non-physical trajectories are perfectly consistent with the target distribution of residuals. Therefore, we exclude data-only KCTs from the flow reconstructions in § 5.2.

In stark contrast, joint particle–flow estimation substantially improves the accuracy of the KCT estimates, yielding lower position, velocity and acceleration errors than the filtering-based approaches across all the seeding densities considered here. Unlike the first four methods, however, performance of the jointly trained models depends upon the seeding density: as the number of particles decreases, the flow becomes progressively under-resolved, which in turn degrades the track estimates. Figure 3 plots the error standard deviations for the raw, filtered, TrackFit and jointly estimated tracks in the x and z directions against the noise level. At the lowest levels, all methods exhibit similar performance. At higher levels, however, joint estimation reduces the position, velocity and acceleration errors by up to 60 % relative to B-spline filtering and TrackFit in the densely seeded cases. The benefit of joint estimation diminishes as the seeding density decreases, and TrackFit becomes competitive once the mean spacing δ lies between $18\ell_\nu$ and $36\ell_\nu$.

https://doi.org/10.1017/jfm.2026.11913 Published online by Cambridge University Press

Noise level	Raw	Filtered	TrackFit	KCT	Joint estimation		
					$\delta = 9\ell_v$	$\delta = 18\ell_v$	$\delta = 36\ell_v$
	0.18	0.12	**0.08**	0.25	**0.08**	0.10	0.11
0.05 px	0.21	0.09	0.06	0.35	**0.04**	0.06	0.08
	0.28	0.08	0.05	0.52	**0.02**	0.04	0.05
	0.54	0.28	0.22	0.76	**0.17**	0.23	0.29
0.15 px	0.45	0.18	0.12	0.71	**0.06**	0.09	0.15
	0.63	0.17	0.07	0.82	**0.03**	0.04	0.07
	0.9	0.47	0.34	1.27	**0.27**	0.34	0.42
0.25 px	0.69	0.28	0.17	1.08	**0.08**	0.12	0.19
	0.96	0.26	0.09	1.19	**0.03**	0.04	0.09
	1.26	0.65	0.46	1.77	**0.36**	0.45	0.55
0.35 px	0.94	0.39	0.22	1.81	**0.10**	0.14	0.24
	1.3	0.37	0.11	2.42	**0.04**	0.05	0.13
	1.62	0.84	0.58	2.28	**0.42**	0.57	0.73
0.45 px	1.17	0.50	0.27	1.99	**0.10**	0.17	0.27
	1.67	0.47	0.13	2.80	**0.03**	0.07	0.15
	1.8	0.93	0.64	2.5	**0.45**	0.66	0.92
0.5 px	1.36	0.55	0.29	2.11	**0.11**	0.19	0.31
	1.87	0.52	0.15	2.85	**0.04**	0.07	0.17

Table 3. Standard deviations of track errors in the z direction for varying noise levels. At each level, the three sub-rows correspond to the position, velocity and acceleration errors, normalised by the friction length ℓ_v, velocity v_v and acceleration v_v^2/ℓ_v, respectively. The lowest error in each row is shown in bold.

Figure 4 shows representative raw, filtered and jointly estimated tracks for the densest seeding case, $\delta = 9\ell_v$, at the lowest and highest noise levels. Tracks are coloured by the v_3 component of velocity and by its absolute error. The z direction coincides with the optical axis and therefore exhibits the largest localisation errors. Finite-difference velocities are highly sensitive to noise, largely obscuring the underlying flow. Track filtering suppresses this amplification and recovers tracks that qualitatively resemble the ground truth, but at high noise the filtered tracks still exhibit substantial errors. This is especially evident in segments of high curvature, where localisation errors become comparable to the true particle motion, and near the first and last time steps, where the available temporal support is limited. Joint estimation ameliorates these issues through physical constraints, yielding low errors over the full extent of each track across all noise levels and seeding densities. A close-up in figure 5 shows this contrast: the 'jointly estimated track' captures subtle fluctuations of the true trajectory, whereas the filtered track remains visibly distorted. Quantitatively, at low noise, NRMSEs for the v_3 velocity component are 17.9 %, 7.7 % and 3.9 % for finite differencing, B-spline filtering and KCTs with joint estimation, respectively. At high noise, these errors increase to 174.4 %, 47.2 % and 9.0 %. That is to say, noise amplifies the errors of the raw and filtered tracks by nearly an order of magnitude, whereas joint estimation limits the amplification to roughly a factor of two to three. This robustness carries directly into the flow reconstruction, as discussed next.

5.2. *Flow-field reconstruction*

Flow states are reconstructed by two methods. First, in the baseline method, described in § 2.2.4, we train the flow model using velocities obtained either from raw tracks

https://doi.org/10.1017/jfm.2026.11913 Published online by Cambridge University Press

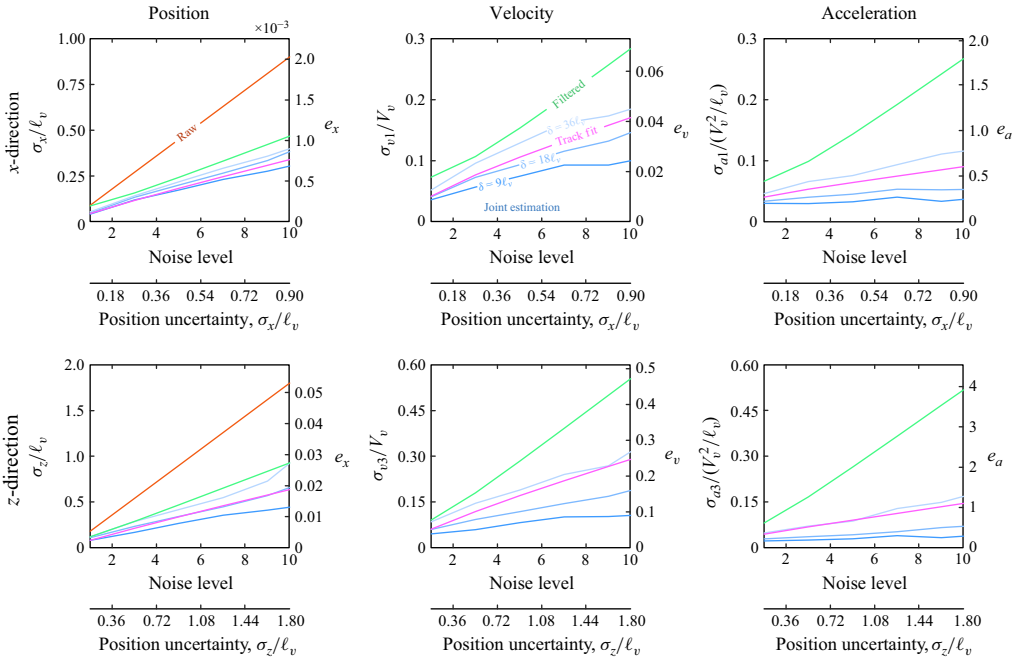


Figure 3. Standard deviations and NRMSEs of particle position, velocity and acceleration errors in the x and z directions under varying noise levels. Joint flow–particle estimation is applied at three inter-particle spacings ($\delta = 9\ell_v$, $18\ell_v$ and $36\ell_v$). Standard deviations are normalised by viscous units. The corresponding position uncertainty at each noise level is labelled below. Joint estimation consistently yields the lowest errors, with some dependence on seeding density. TrackFit achieves accuracy comparable to joint estimation for $\delta = 18\ell_v$ to $36\ell_v$.

processed by finite differencing or using tracks filtered by B-spline smoothing. Second, in the joint estimation, we train the KCT and flow models together. Figure 6 shows the ground truth and error fields of the u_3 velocity component and pressure at the lowest noise level, $\sigma_x = 0.09\ell_v$, using the tracks shown in figure 4. The fields are rendered on three orthogonal planes at the central snapshot in time. All three methods recover the main flow structures with high fidelity, but finite differencing and filtering yield larger errors than joint estimation, with NRMSEs of 17.6 %, 8.0 % and 4.2 %, respectively. The corresponding error fields show a clear reduction in reconstruction error from finite differencing to filtering to joint estimation, illustrating the effects of particle–flow feedbacks. For the u_3 field, low-noise NRMSEs are 11.6 %, 9.4 % and 7.8 %, while for pressure they are 14.9 %, 13.4 % and 12.9 %.

Real LPT experiments can be subject to large localisation errors, especially when single-camera methods are used. Figure 7 shows the ground-truth flow fields and reconstruction errors at the highest noise level considered, which is representative of high-quality plenoptic and DIH–LPT measurements. Baseline reconstructions obtained from finite-difference velocities exhibit large errors throughout the probe volume, reflecting the strong blurring of fine-scale structures. Using velocities from filtered tracks improves the reconstruction markedly, while joint estimation yields the lowest errors and most faithfully recovers the highest-frequency turbulent features. High-noise NRMSEs for the u_3 velocity are 20.9 %, 15.1 % and 12.1 % for finite differencing, filtering and joint estimation, respectively, with corresponding pressure errors of 18.9 %, 13.5 % and 12.2 %. The same trend is evident in the coherent structures extracted from the reconstructions.

https://doi.org/10.1017/jfm.2026.11913 Published online by Cambridge University Press

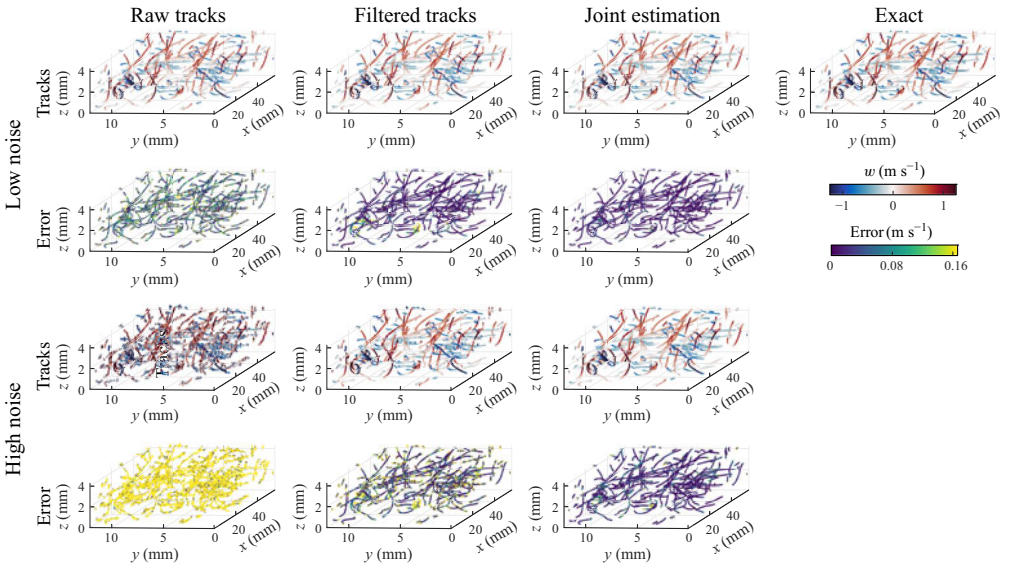


Figure 4. Comparison of exact, raw, filtered and jointly estimated tracks, together with their pointwise velocity errors, at the lowest ($\sigma_x = 0.09\ell_v$) and highest ($\sigma_x = 0.9\ell_v$) noise levels for the densest seeding case ($\delta = 9\ell_v$). Only 200 tracks are shown for clarity. Colours indicate the v_3 velocity or its absolute error. Raw track velocity errors at high noise are downscaled by a factor of five for visualisation. Joint estimation accurately reconstructs track geometries and velocities across noise levels, whereas finite differencing and filtering show large errors, especially near boundaries and in regions of high acceleration.

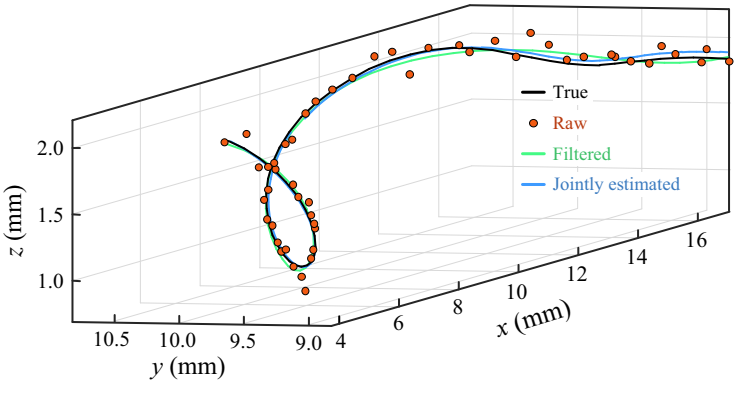


Figure 5. Close-up of a representative track at the noisiest condition. The true track is shown in black, the noisy data as red circles, the filtered track in green and the jointly estimated track in blue. Although filtering improves upon the raw data, joint estimation more accurately recovers the true trajectory.

Specifically, figure 8 shows that, whereas the baseline methods yield flow fields with varying degrees of smoothing, joint estimation resolves more *bona fide* structures across a broad range of scales.

Estimates shown in figure 6–8 correspond to the densest seeding case, which is highly favourable, with particles spaced about 10 viscous units apart. To examine how seeding density and noise interact, we applied both the baseline and joint reconstruction methods to the full matrix of TBL cases described in § 3.1. The resulting NRMSEs of the velocity and pressure fields are plotted over time in figure 9. Naturally, both larger inter-particle

https://doi.org/10.1017/jfm.2026.11913 Published online by Cambridge University Press

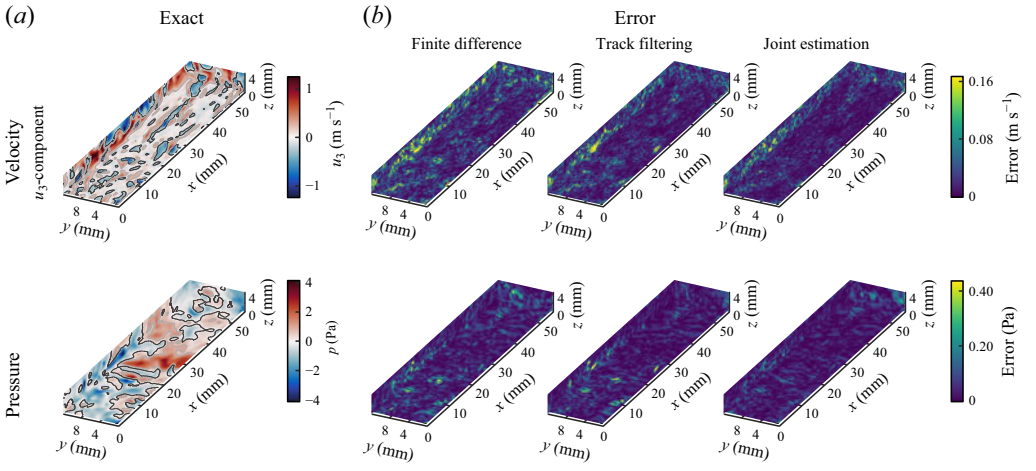


Figure 6. Exact flow fields (a) and absolute error fields (b) at the lowest noise level ($\sigma_x = 0.09\ell_v$) and highest seeding density ($\delta = 9\ell_v$). Dark and grey contour lines indicate low and high iso-values from the exact fields, overlaid on the reconstructions for comparison. The iso-values are -0.17 and $0.17\,\mathrm{m\,s^{-1}}$ for u_3, and 0 and 0.81 Pa for p, respectively. All methods recover the main flow features, but joint estimation yields the lowest errors.

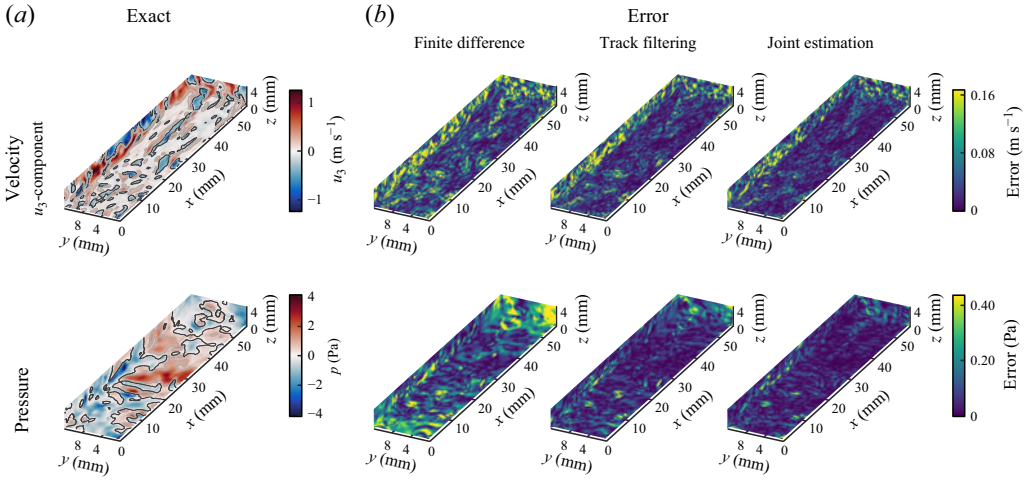


Figure 7. Exact flow fields (a) and absolute error fields (b) at the highest noise level ($\sigma_x = 0.9\ell_v$) and highest seeding density ($\delta = 9\ell_v$). Dark and grey contour lines indicate low and high iso-values from the exact fields, overlaid on the reconstructions for comparison. The iso-values are -0.17 and $0.17\,\mathrm{m\,s^{-1}}$ for u_3, and 0 and 0.81 Pa for p, respectively. Finite-difference and filtered reconstructions blur fine-scale features, whereas joint estimation more faithfully recovers the detailed flow structure.

spacings and higher noise increase the errors for all methods. Baseline reconstructions with velocities computed by finite differencing are especially sensitive. Reconstructions based on filtered velocities benefit from smoothing, but these estimates still degrade substantially as the level of noise increases.

A notable feature of the error traces is the high errors near the beginning and end of the assimilation window. They reflect the limited temporal support available for differentiation near the track ends. In contrast, joint estimation keeps the errors within a relatively narrow band across all the seeding densities and noise levels that we tested, consistent with the

https://doi.org/10.1017/jfm.2026.11913 Published online by Cambridge University Press

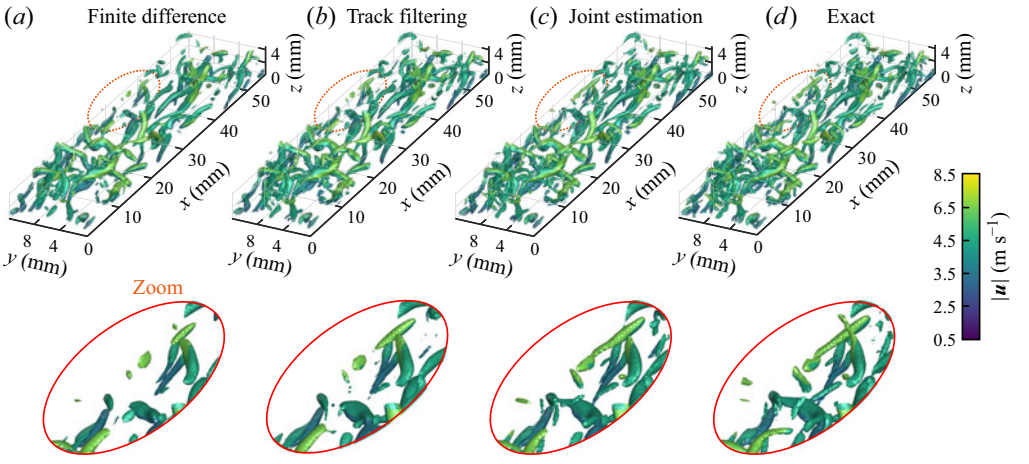


Figure 8. Coherent structures in the TBL reconstructed at the highest noise level ($\sigma_x = 0.9\ell_v$) and densest seeding ($\delta = 9\ell_v$): finite differencing (*a*), filtered tracks (*b*), joint estimation (*c*) and ground truth (*d*). Structures are visualised as Q-criterion isosurfaces ($Q = 2.5 \times 10^6\ \mathrm{s}^{-2}$) coloured by velocity magnitude. Joint estimation best recovers the true structures.

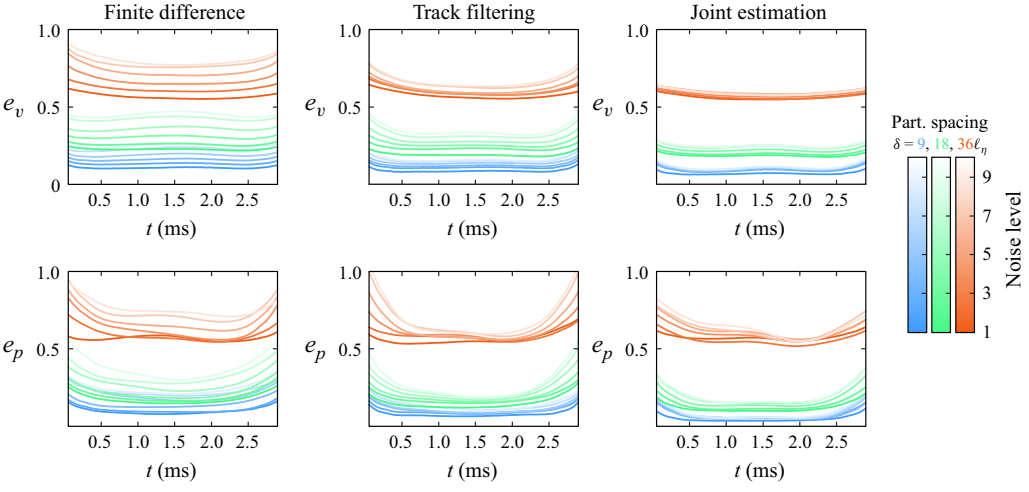


Figure 9. Velocity and pressure errors of the reconstructed flows over the full time window. Colours denote inter-particle spacings of $9\ell_v$ (blue), $18\ell_v$ (green) and $36\ell_v$ (red), with darker shades indicating less noise and brighter shades indicating more noise. Errors increase with both noise level and particle spacing. Finite-difference reconstructions are the most sensitive; filtering provides modest noise suppression; and joint flow–particle estimation consistently maintains the lowest errors.

trends in track error shown in figure 3. The accuracy of joint reconstructions is also fairly uniform over time. Although more advanced optimisers, such as SOAP (Wang *et al.* 2025), may mitigate this effect, the underlying difficulty is tied to the limited temporal support of noisy, sparse and truncated tracks near the observation boundaries. More broadly, this boundary behaviour suggests that reliable flow reconstruction could require a minimum of temporal support. How such a requirement might depend on the flow time scales, measurement rate, noise level and imposed physical constraints remains a topic for future study.

https://doi.org/10.1017/jfm.2026.11913 Published online by Cambridge University Press

Taken together, the track and flow results reported in §§ 5.1 and 5.2 show that incorporating uncertainty information and physics into a joint reconstruction can improve the recovery of particle trajectories as well as flow fields. The governing equations constrain the track geometries; when combined with a prescribed uncertainty model, those geometries permit better localisation of the particles, and the resulting kinematics support more accurate flow reconstruction: a virtuous circle! In this demonstration, we have assumed that the localisation uncertainty distribution is known. In practice, it may be estimated *a priori* using model-based methods (Bhattacharya & Vlachos 2020) or *a posteriori* by estimating the high-frequency noise floor of the position spectrum (Buchwald *et al.* 2025).

6. Joint estimation of flow fields and inertial particle properties

We next study the joint estimation of flow fields and inertial particle properties from particle tracks. Unlike ideal tracers, inertial particles deviate from local flow motion and exhibit dissipative dynamics (Bec 2003). It is therefore not obvious whether inertial track data contain sufficient information to uniquely identify both flow states and the unknown particle properties that affect slip. Flow reconstruction from inertial tracks amounts to a parametrised partial-differential-equation-constrained inverse problem, with the Navier–Stokes equations coupled to one parametrised Maxey–Riley equation per particle (here parametrised by particle diameter d_p and density ρ_p). The framework presented in this text allows us to empirically test whether flow fields and particle properties can be inferred together from the Lagrangian data, alone. We show that such reconstructions are in fact possible. Two representative cases are considered: incompressible turbulence seeded with bidisperse particles that follow the Schiller–Naumann drag law (Schiller 1933), and a supersonic, shock-dominated flow with particle motion described by the compressible Loth drag law (Loth 2008). These examples feature one-way coupling with $St \sim 1$–5 in the former case and non-trivial compressible dynamics with shock–particle interactions in the latter.

6.1. *Homogeneous isotropic turbulence with bidisperse particles*

Figure 10 shows a random subset of 3100 inertial tracks in the HIT flow, coloured by particle diameter. Tracks from small and large particles are intertwined in a dense cluster, with figures 10(*b*) and 10(*c*) isolating each group. The comparison highlights qualitative differences between $St \sim 1$ and $St \sim 5$ transport. Smaller particles (purple) whirl around in all directions with slight velocity lag, while larger particles (chartreuse) bear the mark of gravitational settling, drifting downward in the negative z direction over time. The mean and maximum slip velocities normalised by the Kolmogorov velocity scale, i.e. $|\boldsymbol{u} - \boldsymbol{v}|/u_\eta$, are 2.2 and 13.3 for the small particles ($St \sim 1$) and 9.3 and 27.6 for the large particles ($St \sim 5$). Unlike ideal tracers, which remain strongly correlated to the flow, inertial tracks begin to decorrelate at finite St and become effectively uncorrelated at high St. As a result, both sets of inertial tracks 'mask' the underlying flow in distinct ways, and the particles are unlabelled in the reconstruction (i.e. with no knowledge of their diameter available in the optimisation). This poses a challenge for reconstructing coupled flow states and particle trajectories.

Inertial tracks from the bidisperse particles are used in both the baseline flow-only reconstruction from § 2.2.4 and the joint particle–flow reconstruction. In the baseline case, particles are treated as ideal tracers, such that $\boldsymbol{u} = \boldsymbol{v}$, leading to the velocity-based data loss in (2.12). Particle velocities are obtained from the track data using the B-spline filter. In the joint reconstruction, each particle diameter d_p is a trainable parameter that determines the

https://doi.org/10.1017/jfm.2026.11913 Published online by Cambridge University Press

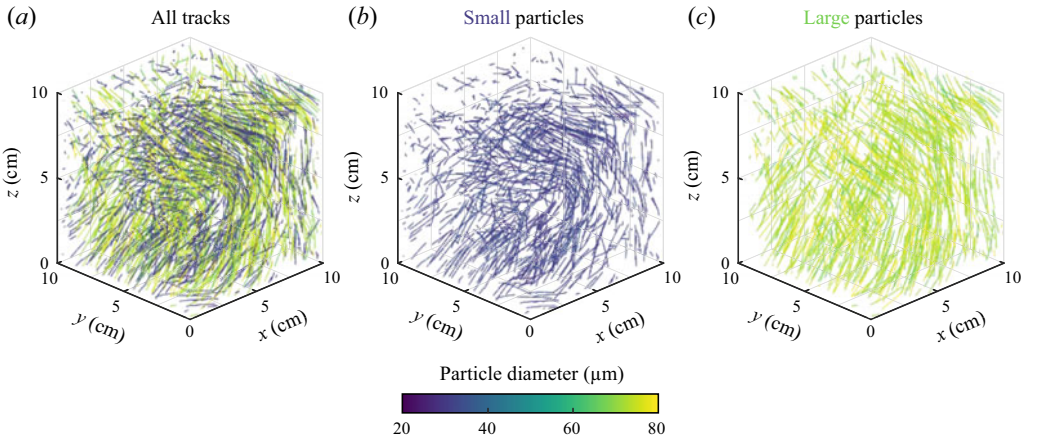


Figure 10. Random selection of bidisperse particle tracks in isotropic turbulence: (*a*) 3100 tracks; (*b*) small particles; (*c*) large particles. Tracks are coloured by particle diameter. Small particles meander in all directions more uniformly, whereas larger particles exhibit pronounced gravitational settling. Tracks are unlabelled in the reconstruction, since d_p and hence St are unknown.

particle's relaxation time τ_p. For inertial particles, τ_p can vary dynamically with the slip velocity through Re_p (B1) and C_D (B3), so the particle dynamics depends on both intrinsic particle properties and the local instantaneous flow velocity. For initialisation, d_p values are drawn from a single Gaussian distribution with mean 52.5 μm and standard deviation 4 μm, chosen to have minimal overlap with the true size distributions.

Figure 11 shows velocity and pressure cut plots from the ground-truth DNS and both reconstructions. Cuts are taken at the bottom ($z = 0$ cm), rear ($y = 10$ cm) and right ($x = 10$ cm) faces of the domain, which represent locations of high error due to the lack of boundary conditions in the reconstructions. While there is qualitative agreement between the DNS and flow-only reconstructions in the u_1 and u_2 components, significant errors appear in u_3 and pressure. These z-direction errors arise because the flow-only method cannot separate gravitational settling from advection, and inaccurate velocities prevent pressure recovery (Pan *et al.* 2016; Faiella *et al.* 2021; Nie *et al.* 2022). Even for the apparently accurate u_1 and u_2 fields, the corresponding error fields reveal large deviations. In contrast, the joint reconstructions are highly accurate across the board, as seen in the dark purple (null) error maps. Time-averaged NRMSEs are 4.2 %, 3.6 % and 11.0 % for the velocity components and 17.2 % for pressure, compared with 18.9 %, 18.3 %, 92.6 % and 72.3 % for the flow-only method. The reconstructions are further examined through coherent structures identified by isosurfaces of the Q-criterion field. Figure 12 shows that flow-only reconstruction produces entirely spurious high-frequency structures, despite the superficial similarity in velocity fields. Meanwhile, joint estimation recovers rich, physically consistent structures, albeit with some noticeable spatial filtering. These results establish the possibility of flow-field reconstruction through the veil of inertial particle dynamics.

Figure 13(*a*) compares the TKE spectra (4.4) from flow-only and joint reconstructions with the DNS reference. For context, we compute the Nyquist wavenumber κ_{Nyq} of particle sampling via (4.6), which sets the maximum recoverable wavenumber for ideal tracers by interpolation alone. Inertial particles, however, alter this picture. Flow-only reconstructions exhibit abnormal TKE behaviour: underestimating energy at low wavenumbers and giving rise to spurious amplification at high wavenumbers, with the low- and high-wavenumber regions demarcated by κ_{Nyq}. The low-wavenumber deficit occurs

https://doi.org/10.1017/jfm.2026.11913 Published online by Cambridge University Press

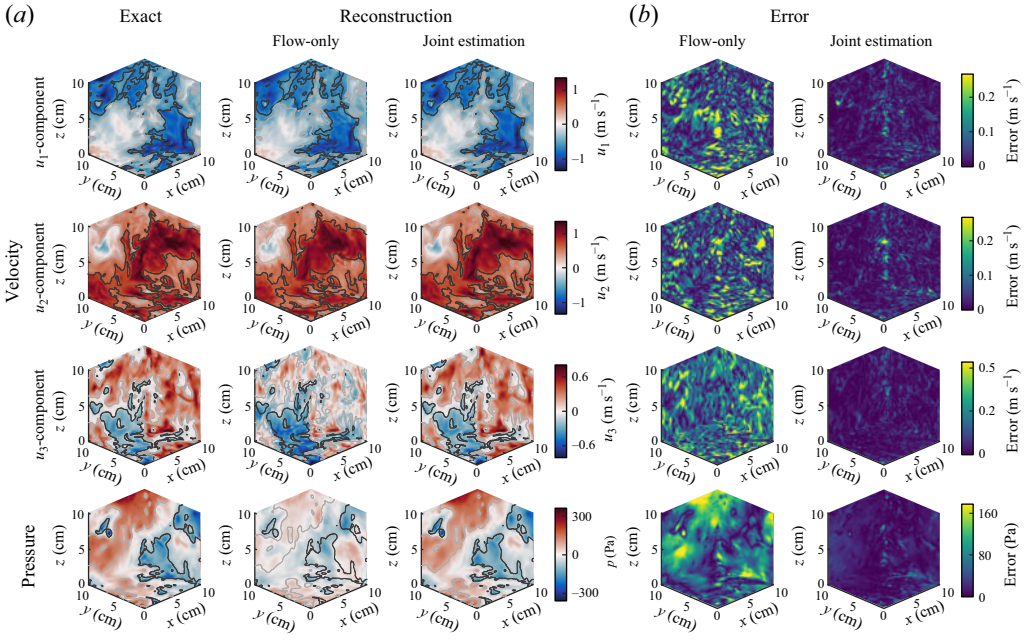


Figure 11. Isotropic turbulent flow fields: (*a*) exact and reconstructed velocity fields; (*b*) absolute error fields. Dark and grey contour lines indicate low and high iso-values from the exact fields, overlaid on the reconstructions for comparison. The iso-values are -636.8 and $-318.4\,\mathrm{m\,s^{-1}}$ for u_1, 318.4 and 636.8 m s^{-1} for u_2, -127.3 and 127.3 m s^{-1} for u_3 and -81.1 and 81.1 Pa for p, respectively. Accounting for particle dynamics enables accurate recovery of turbulent flow from inertial particle tracks.

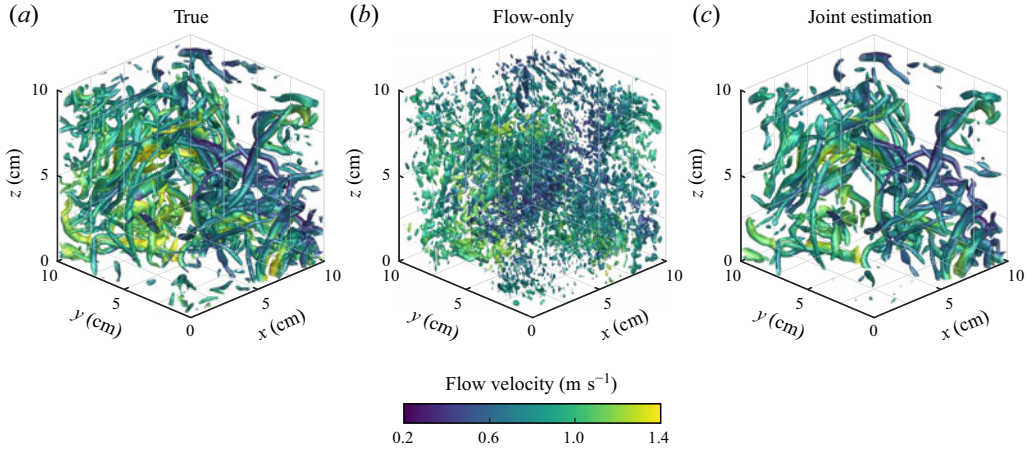


Figure 12. Coherent structures in HIT: (*a*) exact structures; (*b*) flow-only reconstruction under the ideal-tracer assumption ($\boldsymbol{u} = \boldsymbol{v}$); (*c*) joint estimation with inferred St (through d_p). Structures are shown as Q-criterion isosurfaces ($Q = 5000\,\mathrm{s^{-2}}$) coloured by velocity magnitude. Flow-only reconstructions are dominated by artefacts, whereas joint estimation recovers physically consistent structures with some filtering.

because inertial particles respond to turbulent fluctuations with a delay, collectively acting as a low-pass filter on the carrier-phase velocity field (Mei 1996). At high wavenumbers, weakly inertial particles ($St \sim 1$) continue to track the flow, but heavier particles ($St \sim 5$) detach from fluid parcels that are rapidly accelerating, such as in vortices and shear

https://doi.org/10.1017/jfm.2026.11913 Published online by Cambridge University Press

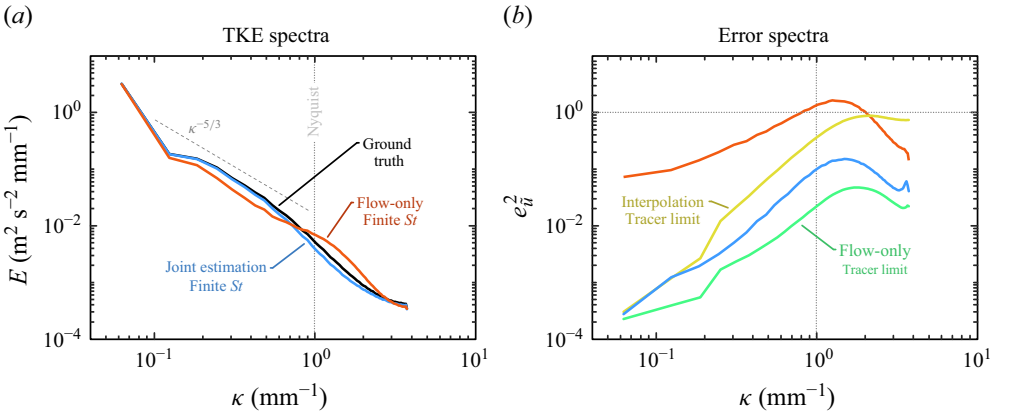


Figure 13. Comparison of TKE spectra. (*a*) The DNS reference (black), flow-only reconstruction (red) and joint reconstruction (blue). (*b*) Normalised error spectra relative to the true energy at each wavenumber, including errors for the flow-only reconstruction (red), joint estimation (blue) and tracer-data baselines under identical conditions: interpolation (yellow) and flow-only reconstruction with tracer data (green). The Nyquist wavenumber $\kappa_{Nyq} = 1.007$ is indicated for reference and coincides with the peak error. Neural reconstructions show decaying error beyond κ_{Nyq} because of the networks' inductive bias. Finite-*St* data produce larger errors, and the flow-only model shows a spurious peak in the super-Nyquist range because of the $St \to 0$ assumption.

layers (Bewley *et al.* 2013; Voßkuhle *et al.* 2014). This detachment leads to multi-valued velocities in an Eulerian description, which cannot be reconciled without accounting for slip velocities, thus producing spurious fluctuations at small scales in a flow-only approach.

By contrast, joint estimation reproduces the DNS spectra well across the wavenumbers. A slight underestimation of TKE appears before κ_{Nyq}, consistent with the spatial filtering effect seen in figure 12. This filtering reflects the additional challenge that comes with using inertial tracks, since particle properties (e.g. d_p) must be inferred simultaneously with the flow states. Because inertial particles encode only indirect information about the carrier phase, they seem to sample the flow less efficiently than ideal tracers. In § 7.1, we show that increasing seeding density mitigates this issue.

Strictly speaking, matching the true TKE spectrum does not guarantee recovery of the target flow fields. For example, distinct snapshots of statistically stationary HIT may share the same TKE spectrum but differ in spatial structure. We therefore compute normalised velocity error spectra, defined in (4.5), and plot them in figure 13(*b*). These spectra quantify reconstruction errors relative to TKE across wavenumbers. For reference, we also include results from ideal tracer tracks that were reconstructed by two conventional methods: adaptive Gaussian windowing, a naive interpolation approach (Agüí & Jimenez 1987), and a flow-only reconstruction. As expected, interpolation without physics asymptotes to 100 % error beyond the Nyquist wavenumber, while flow-only reconstruction at the tracer limit achieves the lowest errors, particularly in the super-Nyquist region, demonstrating the ability of DA methods to recover under-resolved dynamics. A systematic study of the performance of neural DA under varying seeding densities of ideal tracers is presented in Appendix G. By comparison, joint estimation with inertial tracks yields errors lower than naive interpolation but higher than the tracer-based reference, supporting the notion that the information content of inertial tracks that can be leveraged for flow reconstruction is diminished relative to ideal tracers. Finally, flow-only reconstruction with inertial tracks performs worst in the sub-Nyquist region due to inconsistent physical assumptions, but it appears to outperform interpolation at high

https://doi.org/10.1017/jfm.2026.11913 Published online by Cambridge University Press

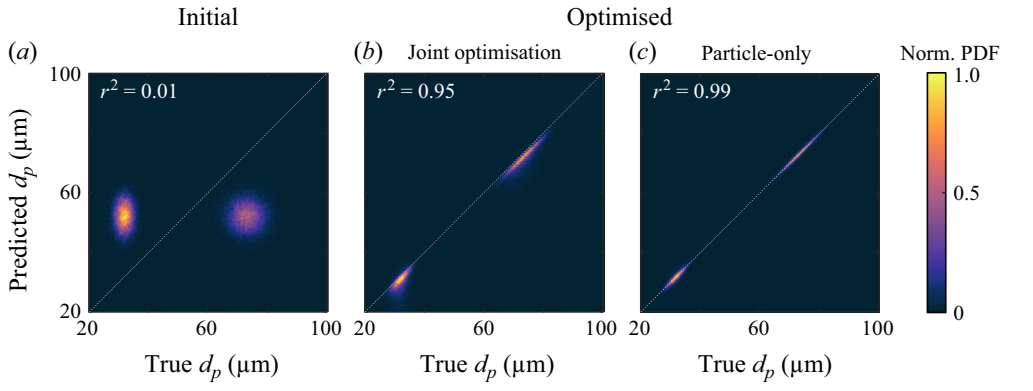


Figure 14. Normalised joint PDFs of estimated and true particle diameters: (*a*) initialisation; (*b*) estimates from joint reconstruction; (*c*) KCT-only estimates computed using the true velocity fields. Joint estimation recovers d_p accurately, with slight underestimation due to filtered slip velocities; reconstructions based on the exact flow are more accurate and essentially unbiased.

wavenumbers. This apparent advantage is simply a by-product of implicit filtering by the network (i.e. its low-frequency inductive bias), which coincides with the natural decay of turbulent energy at small scales.

By training the inertial particle and flow models in tandem, we also recover each particle's diameter. Figure 14 shows normalised joint PDFs of the true and inferred values of d_p. Figure 14(*a*) depicts the random initialisation, drawn from a Gaussian distribution that is centred between the true size distributions. Following joint estimation, the inferred diameters separate into two clusters (figure 14*b*), raising the Pearson correlation between true and estimated values of d_p from 0.01 to 0.95. A slight bias towards underestimation is visible, with density bowing ever so slightly below the 45° line. We attribute this to spatial filtering in the reconstructed velocity fields. That is, high-acceleration events are smoothed out, reducing the apparent slip velocities $|\boldsymbol{u} - \boldsymbol{v}|$ and thus lowering the inferred particle sizes. To test this, we pretrained a high-fidelity neural flow model on DNS velocity data and froze it during the particle inference. With the flow known, the estimated diameters are unbiased (figure 14*c*), and the correlation rises to 0.99.

Before leaving this section, we emphasise that the d_p classification does not rely on prior knowledge of the flow fields nor on analysis of particle images (cf. Khalitov & Longmire 2002; Zhang *et al.* 2008). Rather, the results are obtained solely from the tracks and governing physics. When additional sizing information is available, as in Huang *et al.* (2021) or de la Torre & Jensen (2023), it can be incorporated into the estimation of d_p to further improve accuracy of both the flow states and particle properties. We confirmed this through supplementary tests (not shown), wherein exact values of d_p were prescribed, which yielded more accurate reconstructions of $\boldsymbol{u}$ and p. Statistical priors on d_p from calibration measurements can be similarly beneficial.

6.2. *Supersonic flow over a cone–cylinder body*

We next turn to joint flow–particle estimation in a compressible, shock-dominated flow with inertial particle transport. In high-speed PIV/LPT experiments, seed particles such as TiO_2 or Al_2O_4 are subject to agglomeration due to electrostatic forces, leading to variability in the size and density of the aggregates (Williams *et al.* 2015). These unknown properties, combined with inertial tracks, obscure the flow field. Prior work has shown that PIV measurements of seed traversing an oblique shock wave can be used to calibrate

https://doi.org/10.1017/jfm.2026.11913 Published online by Cambridge University Press

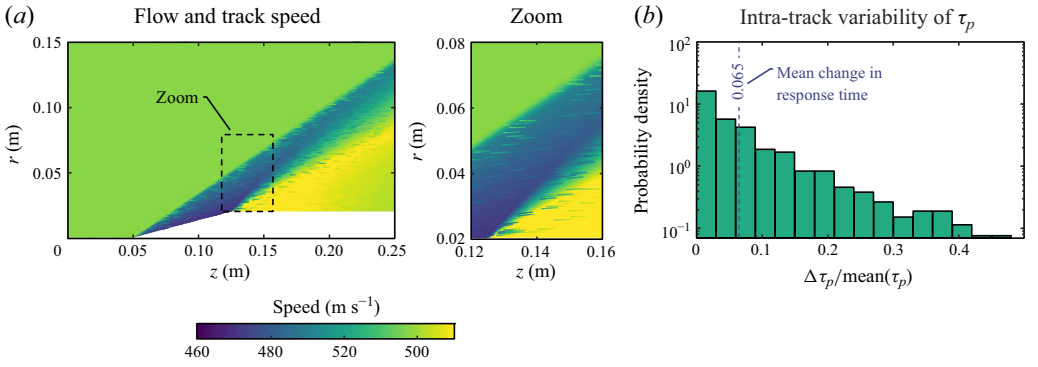


Figure 15. (*a*) Tracks of agglomerated TiO_2 particles in supersonic flow, coloured by particle speed and overlaid on a flow-speed map. Slip is visible in the aft-shock region and expansion fan, where it appears as streaking. (*b*) The PDFs of the normalised intra-track variation of τ_p, highlighting transient changes in particle response across shocks and expansions.

the particle property distributions, yielding values close to manufacturer specifications (Ragni *et al.* 2011; Williams *et al.* 2015). Such calibration data have been employed to assign a constant particle relaxation time τ_p, which could then be used to correct the apparent velocity fields from a cross-correlation analysis of the image pairs (Koike *et al.* 2007; Boiko *et al.* 2015). In practice, however, τ_p usually varies between particles, due to size and density differences, and along individual trajectories, due to local changes in temperature and viscosity. These variations introduce uncertainty into particle properties and flow fields. This issue can be addressed via a joint reconstruction with trainable particle properties.

Figure 15(*a*) shows simulated particle tracks coloured by the local particle speed, with background shading indicating the flow speed. Regions of slip, especially in the aft-shock and expansion fan regions, are clearly visible, manifesting as streaks in the continuous flow speed field. Steep gradients in carrier-phase viscosity, density and speed of sound strongly influence the particle dynamics across shocks and expansions, causing the particle response time to vary substantially throughout the domain (Williams 2014; Williams *et al.* 2015). Figure 15(*b*) presents PDFs of the normalised intra-track range of τ_p for particles punching through the shock wave or lurching forward in the expansion fan. Particles upstream of the shock are excluded, as they are initialised without slip and retain a constant τ_p. On average, τ_p varies by 5.5 % along the tracks in this case, with changes up to 40 % across the shock. These variations underscore the transient character of particle relaxation times in supersonic flows, which has been neglected in some correction schemes for high-speed PIV (Koike *et al.* 2007; Boiko *et al.* 2015).

Inertial tracks from the cone–cylinder case are pre-processed for joint estimation. Since all tracks have a uniform length of eight positions, no track splitting is required. Initial particle diameters are sampled from a Gaussian distribution with mean 2 μm and standard deviation 0.5 μm, while densities are drawn from a Gaussian distribution with mean 950 kg m^{-3} and standard deviation 100 kg m^{-3}. These distributions provide coarse estimates of particle property statistics, assumed to be available in practice from calibration experiments or manufacturer specifications. Figure 16 presents reconstructed axial and radial velocity, density and temperature fields for the cone–cylinder flow. Results are compared against the baseline flow-only reconstruction, which assumes ideal tracers. In the baseline estimates, the shock interface is smeared and density/temperature artefacts appear near the surface, consistent with prior observations (Samimy & Lele 1991;

https://doi.org/10.1017/jfm.2026.11913 Published online by Cambridge University Press

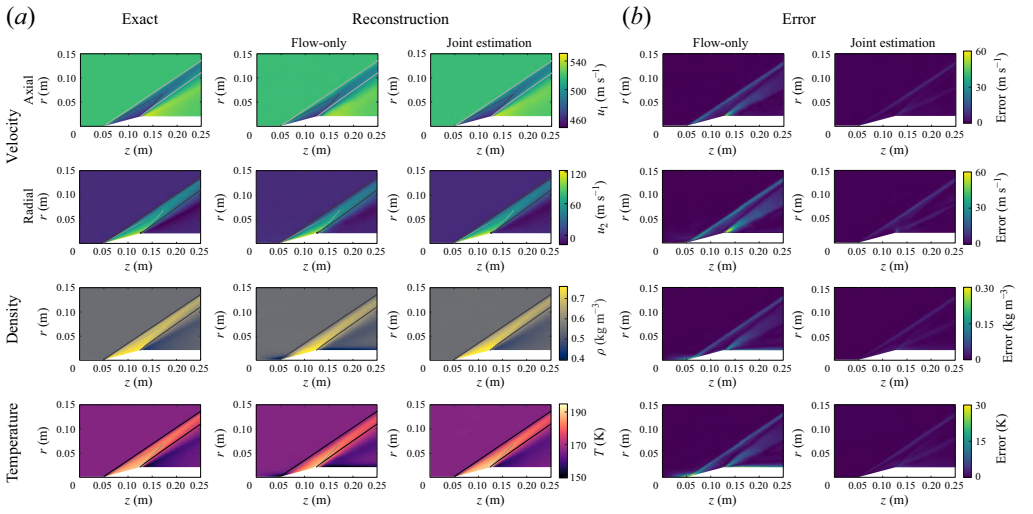


Figure 16. (*a*) Reconstructed cone–cylinder flow fields compared with the CFD reference. (*b*) Absolute error fields, showing sharper shocks and fewer artefacts with joint estimation than with the flow-only baseline. Dark and grey contour lines indicate low and high iso-values from the CFD reference, overlaid on the reconstructions for comparison. The iso-values are 480 and 506 m s^{-1} for the axial velocity component, 22 and 57 m s^{-1} for the radial velocity component, 0.59 and 0.70 kg m^{-3} for density and 172 and 183.5 K for temperature, respectively.

Ragni *et al.* 2011). The joint estimation more accurately resolves the shock structure. Absolute error maps, presented in figure 16(*b*), quantify this improvement: joint estimation achieves NRMSEs of 1 % (axial velocity), 6 % (radial velocity), 3 % (density) and 2 % (temperature), compared to 2 %, 25 %, 18 % and 22 % for the flow-only mode.

Figure 17 shows the inferred particle properties from the joint estimation in the middle column. The top row plots normalised joint PDFs of the estimated and true particle diameters. Although initialised randomly, d_p is effectively optimised to align with the ground truth, with the correlation coefficient improving from 0.01 to 0.8. As in results from the incompressible HIT case, d_p tends to be underestimated due to implicit filtering, particularly across the shock. The bottom row shows the joint PDFs of the estimated and true particle densities ρ_p, which are poorly estimated compared with d_p since τ_p depends quadratically on d_p and linearly on ρ_p, that is: $\tau_p \sim \rho_p d_p^2 / C_D Re_p$ per (B2). We numerically confirmed that the product $C_D Re_p$ remains of order 0.01 for this flow, with minimal variation across particles. Importantly, even with divergent ρ_p estimates, the flow fields are reconstructed with high accuracy, as per figure 16, indicating that the flow model is relatively insensitive to uncertainties in particle density at these conditions.

The joint reconstruction above assumed both d_p and ρ_p to be unknown, representing the most challenging scenario in supersonic PIV/LPT. To assess how prior knowledge of particle properties affects the reconstruction, we reduce the degrees of freedom by fixing ρ_p to its true values and allowing only d_p to vary. The resulting d_p estimates are shown in figure 17(*c*). Compared to the fully unconstrained case, shown in figure 17(*b*), the alignment between estimated and true d_p values is substantially improved, with the Pearson correlation coefficient rising from 0.8 to 0.93. This enhanced particle characterisation translates directly into better flow reconstruction, lowering the NRMSEs to 0.5 % (axial velocity), 4.8 % (radial velocity), 2.3 % (density) and 1.3 % (temperature). These results underscore the complementary nature of the two phases: even partial knowledge of particle properties (here ρ_p) improves the accuracy of both flow fields and particle properties.

https://doi.org/10.1017/jfm.2026.11913 Published online by Cambridge University Press

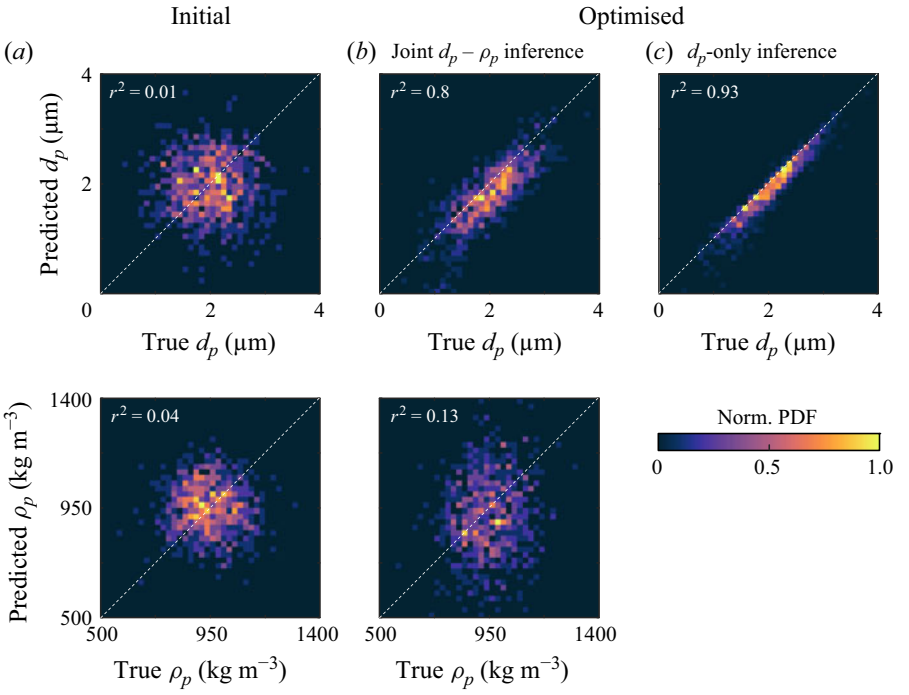


Figure 17. Implicit particle characterisation in the cone–cylinder flow. Initial d_p and ρ_p values (*a*), jointly optimised estimates (*b*) and d_p-only estimates (*c*) are compared with the ground truth. As expected, fixing ρ_p improves the accuracy of the inferred d_p values.

7. Interaction of noise and inertia in flow–particle reconstruction

Section 6 establishes the possibility of jointly estimating flow fields and inertial particle properties, albeit under idealised conditions with dense, noise-free tracks. In real LPT experiments, one must contend with sparse and noisy tracks that could admit many possible solutions. When the number of particles is small, the inversion problem becomes ill-posed: the available data eventually become insufficient to recover both particle properties and flow states. Even when the problem remains formally well-posed, reconstructions may be ill-conditioned in the presence of localisation errors or high-*St* particles, which behave ballistically and interact only weakly with the carrier flow, heightening the sensitivity to noise. In this section, we examine how seeding density, localisation uncertainty and Stokes number interact to govern the feasibility and robustness of joint reconstructions with inertial tracks.

7.1. *Seeding density effects*

To start, we examine the influence of particle seeding density. A suite of test cases is generated in a reduced 64^3 HIT domain, with seeding density varied as described in § 3.4. Both the flow-only and joint estimation methods are tested for comparison. Figure 18 reports NRMSEs of the reconstructed velocity and pressure fields as functions of the normalised inter-particle spacing δ/ℓ_η. Because the flow-only method neglects particle–fluid coupling, reducing the particle spacing does not substantially improve the conditioning of the inverse problem, and the reconstruction remains poor, with velocity and pressure NRMSEs hovering near 40 % and 100 %, respectively. The velocity field is not entirely out of reach, however, since inertial particles ($St = 3$) retain some correlation

https://doi.org/10.1017/jfm.2026.11913 Published online by Cambridge University Press

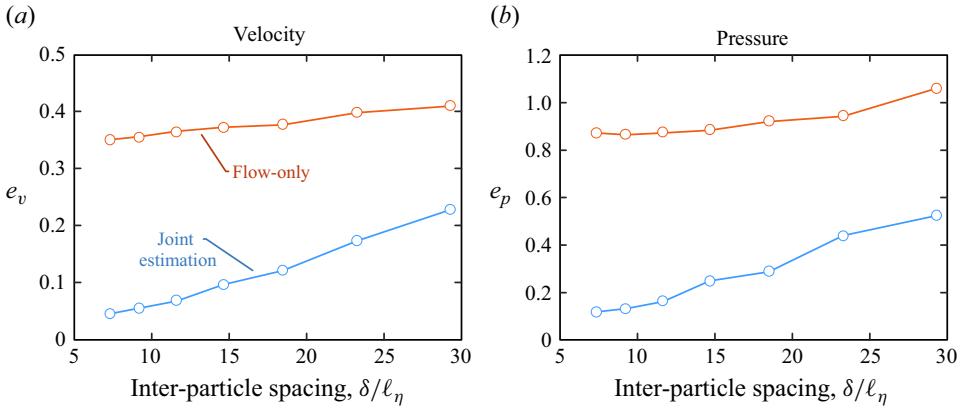


Figure 18. The NRMSEs of reconstructed HIT flow fields versus seeding density: (*a*) velocity; (*b*) pressure. Flow-only reconstructions are shown in red and joint estimation in blue. Errors from joint estimation decrease as the seeding density increases, indicating a transition from a severely ill-posed regime to a much better constrained one.

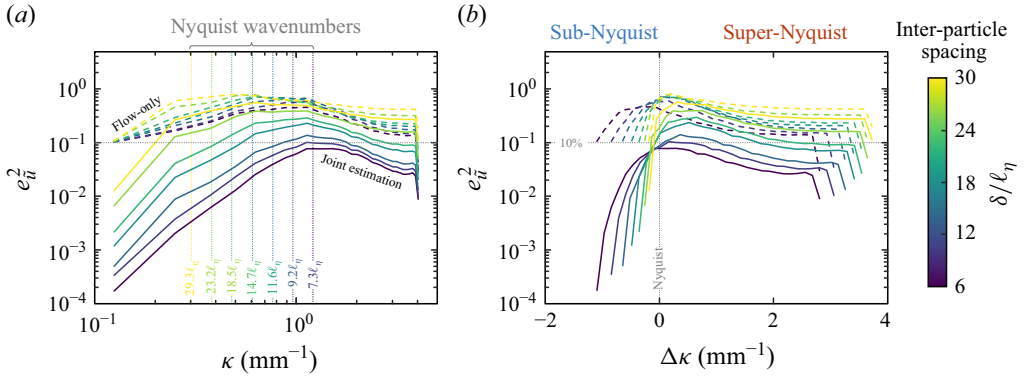


Figure 19. Error spectra of HIT reconstructions under varying inter-particle spacings. Spectra are shown versus wavenumber (*a*) and normalised by the Nyquist wavenumber (*b*). Colours denote particle spacing. Dashed lines indicate flow-only reconstructions, and solid lines indicate joint estimation. Errors in joint estimation decrease rapidly as the seeding density increases, whereas flow-only reconstructions retain large errors across all scales.

with large-scale structures. By contrast, joint estimation improves markedly as the particle spacing decreases, with $e_{\boldsymbol{u}}$ and e_p dropping from roughly 20 % and 50 % to 5 % and 10 %, respectively. This major reduction in error indicates a transition from a severely ill-posed regime to a well-posed one; interestingly, the transition is very gradual.

Figure 19(*a*) shows the normalised spectral errors, per (4.5), for the flow-only and joint reconstructions. Nyquist wavenumbers are plotted to aid interpretation. Errors in the flow-only reconstruction stagnate at a high level, exceeding 10 % across most wavenumbers, whereas the joint estimation method achieves much smaller errors as the particle spacing decreases. To better visualise these trends, figure 19(*b*) plots the error spectra relative to the corresponding Nyquist wavenumbers and separates the sub- and super-Nyquist regions. In the sub-Nyquist region, joint estimation increasingly outperforms the flow-only approach towards lower wavenumbers, in some cases by up to three orders of magnitude. This highlights an important limitation of the flow-only inversion: even the large-scale structures do not improve much as more particles are added. In the super-Nyquist region,

https://doi.org/10.1017/jfm.2026.11913 Published online by Cambridge University Press

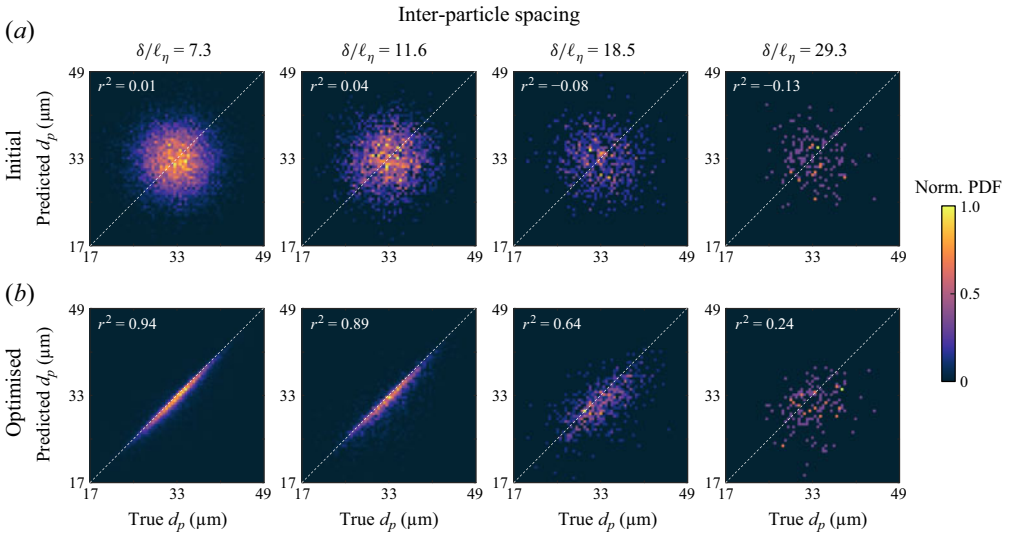


Figure 20. Implicit particle characterisation in a reduced HIT domain under varying seeding densities. Initial (*a*) and optimised (*b*) estimates of d_p are compared with the ground truth. At sparse seeding, the optimised d_p values diverge from the truth, consistent with poor flow reconstruction.

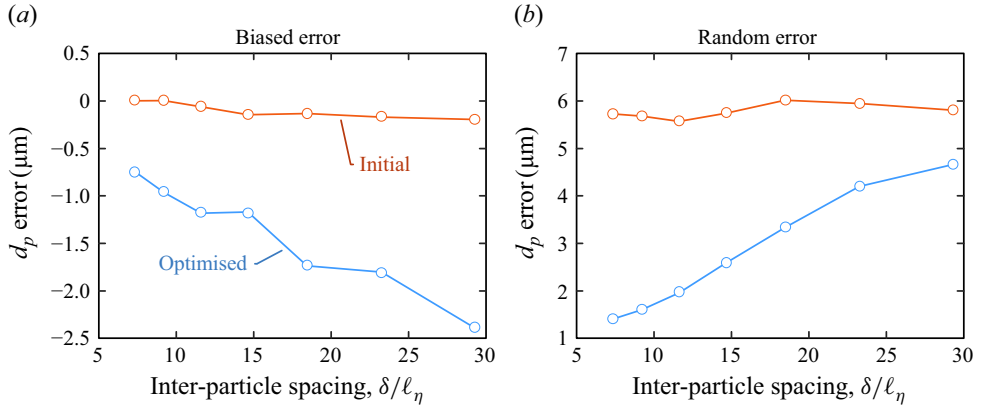


Figure 21. Bias (*a*) and random (*b*) errors in d_p before (red) and after (blue) optimisation across seeding densities. Both decrease sharply at high density because the flow reconstruction improves.

the flow-only reconstruction plateaus at high error, with NRMSEs exceeding 30 %, whereas joint estimation achieves super-resolution at high seeding densities, with errors dropping below 8 % beyond the Nyquist wavenumber in the densest case.

As before, particle sizes are inferred jointly through the inertial model. Figure 20 shows normalised PDFs of the initial and optimised d_p values against the ground truth for four representative particle spacings, labelled at the top of each sub-figure. At small spacings, the optimised values of d_p are closely aligned with the true distribution, whereas at large spacings, the optimisation fails to converge, reflecting the poor flow fields recovered at sparse seeding conditions. The correlation coefficient drops from 0.94 to 0.24 between the smallest and largest spacings. As in figures 14 and 17, d_p is systematically underestimated, consistent with the filtering of slip velocities in the reconstructed flow fields. Figure 21 shows the bias and random error in d_p before and after optimisation, where the bias is the

https://doi.org/10.1017/jfm.2026.11913 Published online by Cambridge University Press

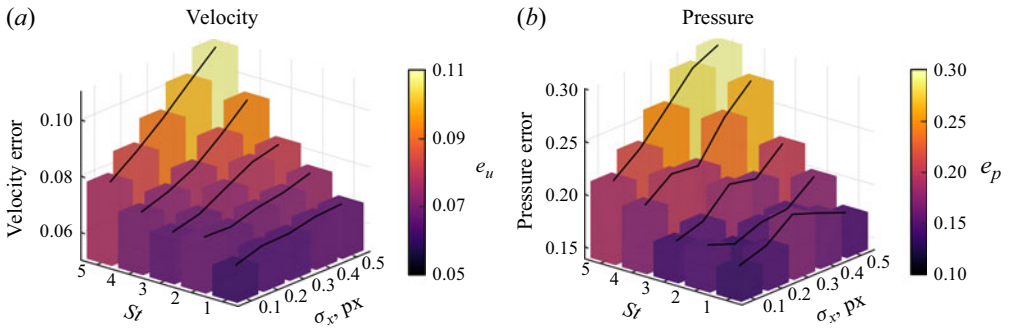


Figure 22. The NRMSEs of reconstructed HIT flow fields: (*a*) velocity; (*b*) pressure, under varying noise levels and Stokes numbers. Accuracy deteriorates with increasing noise and *St*. In the $St \to \infty$ limit, accurate flow recovery becomes extremely difficult because of strong sensitivity to errors in particle acceleration.

mean error across particles and the random error is its standard deviation. As expected from the random initialisation, the initial d_p values are unbiased, whereas the optimised values develop an increasingly negative bias as the particle spacing grows, again reflecting the degradation of the reconstructed velocity field (see figure 19). Random error, by contrast, is sharply reduced with denser seeding, falling from about 5 μm in the sparsest case to 1.5 μm at the highest seeding density.

Taken together, these results show that joint reconstructions with inertial particles depend strongly on seeding density. Dense track data provide enough information for the coupled models to accurately recover the carrier flow and particle properties, whereas sparse seeding leaves the inverse problem too poorly constrained for this task, leading to filtered flow fields and degraded particle property estimates.

7.2. *Noise and Stokes number effects*

Lastly, we examine how measurement uncertainty and particle inertia interact in joint estimation. Inertial tracks are reconstructed over a range of noise levels and Stokes numbers. The resulting NRMSEs for velocity and pressure are shown in the 3-D bar plots of figure 22. Both quantities have similar effects on error, which increases with both noise levels and *St*. At low *St*, the reconstruction is relatively insensitive to noise, whereas at high *St*, the errors increase rapidly with noise. This behaviour is expected. To see why, we rearrange the Maxey–Riley equation (B4) to isolate the carrier velocity:

$$\boldsymbol{u} = \left(\frac{\mathrm{d}\boldsymbol{v}}{\mathrm{d}t} - \boldsymbol{g}\right)\tau_p + \boldsymbol{v}. \tag{7.1}$$

Here, terms II–IV of (B4) are neglected because of the large the density ratio, $\rho_p/\rho \sim O(10^3)$. In the low-*St* limit, with $\tau_p \to 0$, this reduces to $\boldsymbol{u} = \boldsymbol{v}$, so the particle velocity directly tracks the fluid velocity and the reconstruction remains robust, as already seen in § 5. At high *St*, however, the acceleration term $(\mathrm{d}\boldsymbol{v}/\mathrm{d}t - \boldsymbol{g})\,\tau_p$ becomes increasingly important, making $\boldsymbol{u}$ highly sensitive to errors in particle acceleration. Since acceleration estimates degrade rapidly with noise (Berk 2024), the reconstruction becomes much less reliable. In the ballistic limit, where $\tau_p \to \infty$, even small acceleration errors can be amplified without bound. In that regime, the tracks carry too little usable imprint of the surrounding flow to permit accurate reconstruction.

To illustrate what information is practically lost from the inertial tracks and what can be recovered by our joint estimation procedure, figure 23 shows the normalised error spectra of both the flow-only and joint reconstructions over a range of *St*. A medium

https://doi.org/10.1017/jfm.2026.11913 Published online by Cambridge University Press

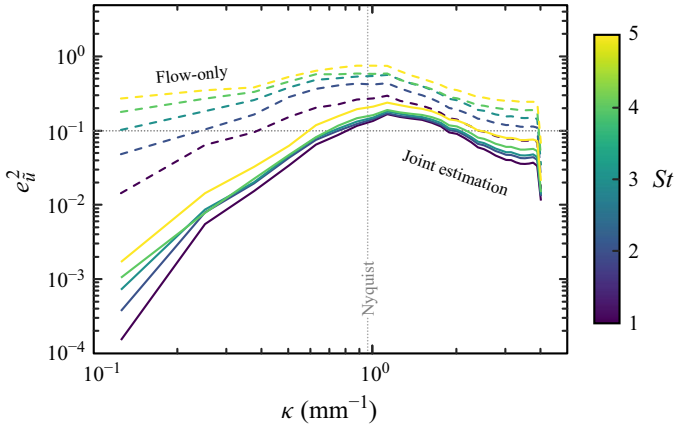


Figure 23. Error spectra of HIT reconstructions under varying Stokes numbers at the medium noise level, $\sigma_x = 0.3$ px. Colour denotes St. Dashed lines indicate flow-only reconstructions, and solid lines indicate joint estimation. Errors from joint estimation collapse into a relatively narrow band, whereas flow-only reconstructions deteriorate rapidly as St increases.

noise level, $\sigma_x = 0.3$ px, is used, corresponding to the upper end of STB uncertainty. The particle-sampling Nyquist wavenumber is plotted for reference. As expected, the flow-only reconstruction yields large errors in both the sub- and super-Nyquist regions, and these increase sharply with St. This arises mainly because the particle velocity field becomes multi-valued at finite St, which cannot be reconciled without explicitly accounting for slip velocities. In contrast, the error spectra from joint estimation collapse into a much narrower band and show only a weak dependence on St. The residual spread across St reflects the noise sensitivity described above: reconstructions based on higher-St particles are more vulnerable to acceleration errors through (7.1). Quantitatively, the cutoff wavenumbers of the flow-only reconstruction at $e^2_{\tilde{u}} = 0.1$ are 0.37 mm^{-1} and 0.24 mm^{-1} for $St = 1$ and 2, respectively; beyond $St = 2$, the spectral errors are uniformly large. Conversely, joint estimation yields cutoff wavenumbers near 0.75 mm^{-1} across all cases, showing that it can recover substantially smaller flow scales than are available under an erroneous assumption of tracer behaviour.

Figure 24 shows the absolute bias and random errors in the inferred particle diameters from joint reconstruction. The bias increases with both noise level and Stokes number, mirroring the trends in the velocity and pressure errors in figure 22. This likely reflects stronger filtering of the reconstructed flow field at larger noise and St, which then propagates into the inferred particle sizes. The random error, however, shows a more nuanced trend. As expected, it grows with noise, but it decreases as St increases. Thus, particles with some degree of inertia make the diameter estimate more repeatable, even though the associated flow reconstruction worsens. This behaviour is consistent with the particle physics loss (2.8), which becomes more sensitive to d_p at larger Stokes number. During training, d_p is optimised together with the flow model to estimate τ_p, i.e. through (B1)–(B3), such that the residuals of (7.1) are minimised. According to (B2) and (B3), τ_p scales as $\tau_p \sim \rho_p d_p^{1.313}$, so the sensitivity of τ_p to d_p increases with particle inertia. In the tracer limit, by contrast, perturbations in d_p have little effect on the dynamics, such that the true particle size cannot be determined from track data. It should be noted that this lack of information about d_p does not compromise recovery of the flow field, however, since near-tracer particles closely track the carrier phase.

https://doi.org/10.1017/jfm.2026.11913 Published online by Cambridge University Press

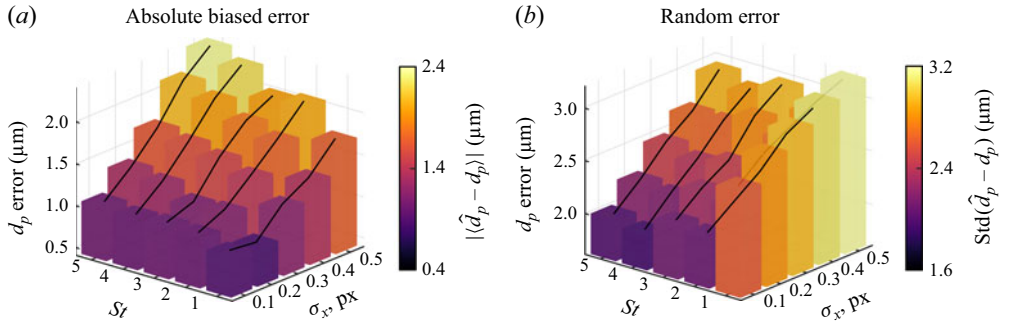


Figure 24. Absolute bias (*a*) and random (*b*) errors of the inferred particle diameters under varying noise levels and Stokes numbers. The bias increases with both noise and *St* because the reconstructed velocity fields become more strongly filtered. The random error decreases with increasing *St* because the physics loss becomes more sensitive to d_p. In the tracer limit, d_p is nearly unidentifiable.

Several practical (and largely intuitive) guidelines follow from these results. First, seeding density should be increased whenever possible, provided that one-way coupling remains valid and that particle tracking is not degraded by overlapping particle images. Second, low-inertia particles are generally preferable for accurate flow reconstruction. When only high-inertia particles are available, high-resolution LPT systems become especially important because they reduce noise and improve acceleration estimates during joint reconstruction. Third, when particle properties are also of interest, lower measurement noise reduces both the bias and the random error in the inferred quantities. High seeding densities are again beneficial because they reduces implicit filtering of the flow and thereby limit bias in the recovered particle properties.

8. Concluding remarks

This work numerically investigates the joint estimation of flow fields and particle properties using Lagrangian track data. The problem is motivated by two central challenges in LPT experiments: noisy particle tracks and inertial transport effects. Existing DA algorithms rely on error-prone velocity estimates derived from fitted tracks and assume ideal tracer particles with zero slip, both of which can compromise the fidelity of Eulerian reconstructions. To overcome these limitations, we propose to reconstruct the flow and particle states jointly from track data, under the combined constraints of disperse multiphase flow physics and known/estimated localisation uncertainties. The resulting framework, termed NIPA, is built on a PINN architecture that couples a neural flow model with a set of KCT models, with one for each particle. Joint training of these models yields flow fields and particle properties that at once satisfy governing physics and match the LPT data.

We test NIPA across a range of particle-laden flows: incompressible turbulence with ideal tracers in § 5, incompressible turbulence with inertial particles in § 6.1 and compressible, shock-dominated flow with inertial particles in § 6.2. For each case, we ask whether the available track data, taken together with the governing physics, suffice to recover both flow states and unknown particle properties. We also examine how seeding density, noise magnitude and Stokes number influence the robustness of reconstructions in § 7. From these studies, four main conclusions emerge, as summarised below.

https://doi.org/10.1017/jfm.2026.11913 Published online by Cambridge University Press

(i) For noisy tracks of ideal tracers, joint estimation can recover both the flow field and the underlying particle trajectories in the TBL case, provided a sufficient number of tracks are available (§ 5). Across a broad range of seeding densities, jointly estimated tracks and flow fields are more accurate than filtered tracks or baseline flow-only reconstructions, highlighting the value of coupled flow–particle learning. As seeding density decreases, accuracy degrades, and conventional filtering may become preferable once the Eulerian field can no longer be inferred reliably from the available tracks. At large localisation uncertainties, however, joint estimation remains robust and outperforms conventional filtering by up to 50 %, owing to the integration of physics-informed tracking with the flow reconstruction.

(ii) Inertial particle properties can be inferred jointly with incompressible (§ 6.1) and compressible (§ 6.2) flow fields. Reconstructions that account for particle–fluid interactions, e.g. through the Maxey–Riley equation, recover the flow accurately from inertial tracks. Particle properties such as their diameter can be inferred from the tracks and governing physics. In the compressible case, particle densities do not reliably converge, reflecting the weak sensitivity of the reconstruction to ρ_p, although this does not noticeably degrade the flow field. When particle properties are known and supplied during training, the flow reconstruction improves substantially.

(iii) In inertial-particle cases, reconstruction quality depends strongly on the information content of the track data (§ 7.1). Dense seeding enables scale-resolving reconstructions, in some cases beyond the particle Nyquist wavenumber, whereas sparse seeding makes the inversion severely ill-posed and yields heavily filtered flow fields that miss much of the high-wavenumber content. These filtered fields in turn degrade the particle inference, leading to systematic underestimation of particle diameters and increased random errors.

(iv) Both flow reconstruction and particle inference depend strongly on localisation uncertainties and Stokes numbers (§ 7.2). As expected, reconstruction accuracy declines with increasing noise and St. At high St, ballistic particle motion amplifies even small acceleration errors through the Maxey–Riley dynamics, making accurate flow recovery increasingly difficult. Bias in the inferred particle size also grows with noise and St because the flow field becomes more strongly filtered. At the same time, random errors in particle size decrease with increasing St, since higher-inertia particles make the physics loss more sensitive to changes in d_p. In the tracer limit, particle size is effectively unidentifiable, though this does not hinder recovery of the flow field.

Lastly, we note that the ideas developed here are not tied specifically to NIPA. The central point is that Lagrangian information can be incorporated directly into a coupled, physics-constrained flow–particle reconstruction. Similar ideas could be pursued with other DA frameworks, including adjoint–variational approaches (Gutierrez & Wang 2026; Ke *et al.* 2026). Continued advances in solvers, track models and optimisation methods may further improve performance, especially in the inertial regime, thereby broadening the range of LPT conditions under which such reconstructions are useful.

Acknowledgements. The authors acknowledge the generous support of Professor A. Schröder, Dr D. Schanz, Mr T. Buchwald and Mr P. Godbersen of the German Aerospace Center (DLR) Göttingen and Brandenburg University of Technology Cottbus-Senftenberg for their assistance in generating the TrackFit results and for helpful discussions regarding their interpretation.

Funding. This material is based upon work supported by the National Science Foundation under Grant Number 2615425.

https://doi.org/10.1017/jfm.2026.11913 Published online by Cambridge University Press

Declaration of interests. The authors report no conflict of interest.

Appendix A. Carrier-phase governing equations

Lagrangian particle tracking experiments involve disperse multiphase flows, wherein tracer particles constitute the disperse phase and the fluid of interest is the carrier phase. Depending on the particle mass loading and volume fraction, particle–fluid interactions are modelled using one-way, two-way or four-way coupling schemes (Subramaniam & Balachandar 2022). Analysis in this work applies to the one-way-coupled regime, where momentum transfer from particles to the carrier flow is negligible. This assumption is appropriate for most PIV and LPT experiments, which typically operate in the dilute limit. Governing equations for flows in the test cases introduced in § 3 are summarised below.

A.1. *Equations for unsteady 3-D incompressible flow*

Flows in the TBL (§ 3.1) and HIT (§ 3.2) cases are governed by the 3-D continuity and momentum equations for incompressible flow:

$$\boldsymbol{\nabla}\cdot\boldsymbol{u}=0, \tag{A1a}$$

$$\frac{\partial \boldsymbol{u}}{\partial t}+\boldsymbol{u}\cdot\boldsymbol{\nabla}\boldsymbol{u}=-\frac{1}{\rho}\boldsymbol{\nabla}p+\nu\nabla^2\boldsymbol{u}+\boldsymbol{F}, \tag{A1b}$$

where $\boldsymbol{u}$ is the 3-D velocity vector and $\boldsymbol{\nabla}$ denotes the del operator in Cartesian coordinates. For isotropic turbulence, a forcing term is introduced to sustain stationary turbulence (Rosales & Meneveau 2005):

$$\boldsymbol{F}=\frac{\varepsilon}{3u_{rms}^2}\boldsymbol{u}, \tag{A2}$$

with ε being the mean energy dissipation rate and u_{rms} the root-mean-square velocity. For the TBL case, we set $\boldsymbol{F}=\boldsymbol{0}$. In both the TBL and HIT cases, the residual vector $\boldsymbol{e}_f$ in (2.7) is formed from the components of (A1).

A.2. *Equations for steady axisymmetric compressible flow*

The cone–cylinder flow (§ 3.3) is governed by the steady, axisymmetric compressible Navier–Stokes equations for the conservation of mass, momentum and energy:

$$\boldsymbol{\nabla}\cdot(\rho\,\boldsymbol{u})=0, \tag{A3a}$$

$$\boldsymbol{\nabla}\cdot\left(\rho\,\boldsymbol{u}\,\boldsymbol{u}^{\top}\right)=-\boldsymbol{\nabla}p+\boldsymbol{\nabla}\cdot\left[\mu\left(\boldsymbol{\nabla}\boldsymbol{u}+\boldsymbol{\nabla}\boldsymbol{u}^{\top}\right)-\frac{2}{3}\mu\,(\boldsymbol{\nabla}\cdot\boldsymbol{u})\,\boldsymbol{I}\right], \tag{A3b}$$

$$\boldsymbol{\nabla}\cdot\left[(\rho E+p)\,\boldsymbol{u}\right]=\boldsymbol{\nabla}\cdot(k\boldsymbol{\nabla}T)+\boldsymbol{\nabla}\cdot\left\{\left[\mu\left(\boldsymbol{\nabla}\boldsymbol{u}+\boldsymbol{\nabla}\boldsymbol{u}^{\top}\right)-\frac{2}{3}\mu\,(\boldsymbol{\nabla}\cdot\boldsymbol{u})\,\boldsymbol{I}\right]\cdot\boldsymbol{u}\right\}. \tag{A3c}$$

In these expressions, $\boldsymbol{u}$ denotes the velocity vector with axial and radial components and $\boldsymbol{\nabla}$ is the two-dimensional del operator in cylindrical coordinates (axial–radial). The thermodynamic variables are the density ρ, pressure p and temperature T, while E is the specific total energy and k the thermal conductivity of the carrier phase. The temperature T is obtained from the local total energy and velocity magnitude, and transport properties μ and k are evaluated via Sutherland's law (Anderson 1990).

Equation (A3) comprises four governing equations with five unknowns and must therefore be closed with an equation of state. We adopt the calorically perfect gas law:

https://doi.org/10.1017/jfm.2026.11913 Published online by Cambridge University Press

$$p = (\gamma - 1)\,\rho \underbrace{\left(E - \frac{1}{2}\boldsymbol{u}\cdot\boldsymbol{u}\right)}_{C_v T}, \tag{A4}$$

where $\gamma = C_p/C_v$ is the ratio of specific heat at constant pressure C_p to that at constant volume C_v. For the cone–cylinder test case, the residual vector $\boldsymbol{e}_f$ in (2.7) collects the contributions from each of the conservation laws in (A3).

Appendix B. Disperse-phase governing equations

This appendix summarises the particle dynamics models employed for the bidispersed HIT case (§ 3.2) and the supersonic cone–cylinder flow case (§ 3.3). We begin with the full Maxey–Riley equation, which governs the motion of small spherical particles in incompressible fluids. We then outline its modification for compressible flows, relevant to tracer particle dynamics in high-speed PIV/LPT applications. Next, we introduce key dimensionless numbers that quantify the relative importance of viscous, compressibility and rarefaction effects on particle motion. Finally, we summarise a drag law suitable for supersonic conditions, which incorporates corrections for these effects.

B.1. *Maxey–Riley equation*

Small spherical particles moving in a locally uniform flow are subject to both inertial and viscous forces. The inertial transport regime is commonly characterised by the particle Reynolds number, defined in terms of a characteristic particle length (diameter d_p), slip velocity and fluid density and viscosity:

$$Re_p = \frac{\rho d_p \overbrace{|\boldsymbol{u} - \boldsymbol{v}|}^{slip}}{\mu}. \tag{B1}$$

Here, 'slip' refers to the ballistic motion of the particle relative to the carrier fluid. A related measure is the particle response time, which quantifies the time scale at which a particle relaxes towards the local fluid velocity:

$$\tau_p = \frac{4}{3C_D Re_p}\frac{\rho_p d_p^2}{\mu} = \frac{4}{3C_D}\frac{\rho_p}{\rho}\frac{d_p}{|\boldsymbol{u} - \boldsymbol{v}|}, \tag{B2}$$

where C_D is the drag coefficient. In the creeping-flow limit, where $Re_p \ll 1$, the Stokes law applies, with $C_D = 24/Re_p$. For finite Re_p, however, inertial effects necessitate modification of the drag law. For our HIT case, we adopt the Schiller–Naumann correlation:

$$C_D = \frac{24}{Re_p}\left(1 + 0.15 Re_p^{0.687}\right), \quad Re_p < 800, \tag{B3}$$

which has been validated over a broad range of Re_p. More general drag laws applicable at higher Re_p are reviewed in Chapter 8 of Subramaniam & Balachandar (2022) and can be incorporated into the DA framework where applicable.

When particles are much smaller than the relevant hydrodynamic length scale (i.e. quasi-point particles), their dynamics is governed by the version of the Maxey–Riley equation

https://doi.org/10.1017/jfm.2026.11913 Published online by Cambridge University Press

(Maxey *et al.* 1997) modified by Mei (1996):

$$\frac{\mathrm{d}\boldsymbol{v}}{\mathrm{d}t} = \underbrace{\frac{\boldsymbol{u}-\boldsymbol{v}}{\tau_p}}_{\mathrm{I}} + \underbrace{\frac{\rho}{\rho_p}\frac{\mathrm{D}\boldsymbol{u}}{\mathrm{D}t}}_{\mathrm{II}} + \underbrace{\frac{1}{2}\frac{\rho}{\rho_p}\left(\frac{\mathrm{D}\boldsymbol{u}}{\mathrm{D}t} - \frac{\mathrm{d}\boldsymbol{v}}{\mathrm{d}t}\right)}_{\mathrm{III}} + \underbrace{\sqrt{\frac{9}{2\pi}\frac{\rho}{\rho_p\tau_p}}\int_{-\infty}^{t}\frac{1}{\sqrt{t-\tau}}\frac{\mathrm{d}(\boldsymbol{u}-\boldsymbol{v})}{\mathrm{d}\tau}\mathrm{d}\tau}_{\mathrm{IV}} + \underbrace{\boldsymbol{g}}_{\mathrm{V}}, \tag{B4}$$

where $\mathrm{D}/\mathrm{D}t$ and $\mathrm{d}/\mathrm{d}t$ denote total derivatives following a fluid parcel and a particle, respectively. The five terms on the right-hand side correspond to: (I) quasi-steady drag, (II) pressure gradient force, (III) added mass effect, (IV) Basset history term (unsteady vorticity diffusion) and (V) gravitational force. Since the carrier-phase momentum equation, i.e. (A1*b*), neglects gravity, buoyancy is not included in (B4). If gravity were retained, the last term would instead appear as $(1-\rho/\rho_p)\boldsymbol{g}$, consistent with the formulation of Mei (1996). The relative magnitude of each contribution depends on flow conditions and particle properties, e.g. density and diameter (Thomas 1992; Ling *et al.* 2013).

Two simplifications are made based on the properties of the small, dense particles assumed in our simulations. First, owing to the large particle-to-fluid density ratio, $\rho_p/\rho \sim O(10^3)$, we neglect the Basset history force in the forward simulations (Eaton 2009; Ling *et al.* 2013). In the reconstructions, we additionally omit the pressure gradient and added mass forces, which are indeed included in the forward simulations, since their magnitudes are roughly three orders of magnitude smaller than Stokes drag. This deliberate mismatch between the forward and reconstruction force models highlights the robustness of NIPA to imperfect particle dynamics, which is important in practice. Second, given the minute particle size, we neglect finite-size corrections such as the Faxén term and Saffman lift (Maxey *et al.* 1997). The Kolmogorov length scale in § 3.2 is about 350 μm: substantially larger than the maximum particle diameter of ∼70 μm, thereby justifying the quasi-point-particle assumption. Consequently, for the HIT case, the residual vector $\boldsymbol{e}_p{}^{(k)}$ in (2.8) includes only the contributions from Stokes drag and gravity, i.e. terms (I) and (V) in (B4), for the kth particle.

B.2. *Particle dynamics in compressible flows*

Tracer particles in high-speed flow are often modelled as solid spheres immersed in an unbounded fluid and subject only to quasi-steady drag (Williams *et al.* 2015). For typical tracers in PIV or LPT, i.e. very small ($d_p \sim 1$ μm) and with large density ratios ($\rho_p/\rho \gg 1$), the contributions of pressure gradient, added mass, Basset history and body forces are negligible in high-speed conditions (Melling 1997; Ragni *et al.* 2011). Under these assumptions, the Maxey–Riley equation reduces to a balance between slip velocity and quasi-steady drag:

$$\frac{\mathrm{d}\boldsymbol{v}}{\mathrm{d}t} = \frac{\boldsymbol{u}-\boldsymbol{v}}{\tau_p}, \tag{B5}$$

where τ_p is the particle response time given in (B2). In our supersonic cone flow case, $\boldsymbol{u}$ and $\boldsymbol{v}$ are two-dimensional vectors (axial and radial), and the residual $\boldsymbol{e}_p{}^{(k)}$ in (2.8) comprises both components of (B5) for the kth particle. Although pressure gradient, added mass and Basset history forces can momentarily exceed Stokes drag as particles traverse a shock wave, their cumulative effect on particle trajectories is negligible in the high-density-ratio limit (Thomas 1992; Parmar *et al.* 2009; Capecelatro & Wagner 2023), making them safe to neglect for our purposes.

https://doi.org/10.1017/jfm.2026.11913 Published online by Cambridge University Press

B.3. *Compressible drag law*

Particle drag in high-speed flow depends not only on viscous forces from the carrier phase but also on compressibility and rarefaction effects. Compressibility effects scale with the particle Mach number:

$$Ma_p = \frac{|\boldsymbol{u} - \boldsymbol{v}|}{\sqrt{\gamma RT}}, \tag{B6}$$

where R is the specific gas constant of the carrier phase. Rarefaction effects are governed by the ratio of the mean free path of the carrier fluid, λ, to a characteristic length scale, typically the particle diameter at low Re_p. This ratio defines the particle Knudsen number:

$$Kn_p = \frac{\lambda}{d_p} = \frac{Ma_p}{Re_p}\sqrt{\frac{\pi\gamma}{2}}, \tag{B7}$$

where the expression on the right-hand side follows from the ideal gas law. Thus, drag correlations for compressible particle-laden flows can be expressed in terms of any two of the three non-dimensional groups: Re_p, Ma_p and Kn_p. In practice, this formulation allows models such as Loth's drag law, discussed next, to bridge viscous, compressibility-dominated and rarefaction-dominated regimes.

Loth (2008) put forth a comprehensive drag correlation for compressible particle-laden flows. The model expresses the drag coefficient C_D as a function of particle Reynolds and Mach numbers, thereby defining the particle response time τ_p through (B2). The general form is

$$C_D = \begin{cases} \dfrac{C_{D,Kn,Re}}{1 + Ma_p^4} + \dfrac{Ma_p^4 C_{D,f_M,Re}}{1 + Ma_p^4}, & Re_p < 45, \\ \dfrac{24}{Re_p}\left[1 + 0.15Re_p^{0.687}\right] H_M + \dfrac{0.42C_M}{1 + \dfrac{42\,500\,G_M}{Re_p^{1.16}}}, & Re_p > 45. \end{cases} \tag{B8}$$

The first branch of (B8) applies in the rarefaction-dominated regime ($Re_p < 45$) and the second branch in the compression-dominated regime ($Re_p > 45$). Although we implement the full model in forward simulations, the cone–cylinder case has $Re_p < 23$ throughout, so only the rarefaction branch is used in our reconstructions. Figure 25 shows C_D normalised by Stokes drag as a function of Re_p and Ma_p. At low Re_p, contours of C_D align with those of Kn_p, indicating rarefaction control. As Re_p increases, the gradient of $C_D Re_p/24$ bends towards the Ma_p axis, marking the onset of compressibility effects. In our case, however, the flow remains entirely within the aforementioned rarefaction regime.

Returning to (B8), the rarefaction-specific terms are

$$C_{D,Kn,Re} = \frac{24}{Re_p}\left(1 + 0.15Re_p^{0.687}\right) f_{Kn}, \tag{B9a}$$

$$f_{Kn} = \frac{1}{1 + Kn_p\left[2.514 + 0.8\,\exp\left(-\dfrac{0.55}{Kn_p}\right)\right]}, \tag{B9b}$$

$$C_{D,f_M,Re} = \frac{C_{D,f_M}}{1 + \left(\dfrac{C_{D,f_M}}{1.63} - 1\right)\sqrt{\dfrac{Re_p}{45}}}, \tag{B9c}$$

https://doi.org/10.1017/jfm.2026.11913 Published online by Cambridge University Press

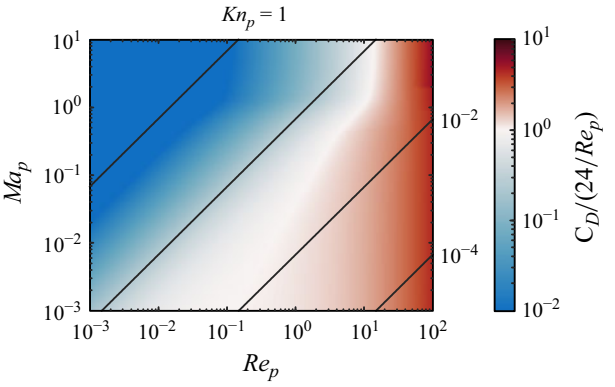


Figure 25. Loth drag model normalised by Stokes drag, showing its dependence on Re_p and Ma_p. Black lines indicate contours of constant Kn_p.

$$C_{D,f_M} = \frac{\left(1+2s_M^2\right)\operatorname{erf}\left(-s_M^2\right)}{s_M^3\sqrt{\pi}} + \frac{\left(4s_M^4+4s_M^2-1\right)\operatorname{erf}(s)}{2s_M^4} + \frac{2}{3s_M}\sqrt{\frac{\pi T_p}{T}}, \tag{B9d}$$

$$s_M \equiv Ma_p\sqrt{\gamma/2}, \tag{B9e}$$

where T_p is the particle temperature. The compression-specific contributions to (B8) are

$$H_M = 1 - \frac{0.258C_M}{1+514\,G_M}, \tag{B10a}$$

$$G_M = \begin{cases} 1-1.525\,Ma_p^4, & Ma_p < 0.89, \\ 0.0002+0.0008\tanh\left[12.77\left(Ma_p-2.02\right)\right], & Ma_p > 0.89, \end{cases} \tag{B10b}$$

$$= \begin{cases} \dfrac{5}{3}+\dfrac{2}{3}\tanh\left[3\,\log\left(Ma_p-0.1\right)\right], & Ma_p < 1.45, \\ 2.044+0.2\,\exp\left[-1.8\,\log\left(\dfrac{Ma_p}{1.5}\right)^2\right], & Ma_p > 1.45. \end{cases} \tag{B10c}$$

The resultant drag law has been extensively benchmarked using experimental data and employed for many simulations of high-speed particle-laden flow. Recently, Loth *et al.* (2021) published a comprehensive review of relevant results, obtained from particle-resolved DNS, rarefied-gas simulations and wind tunnel experiments. The authors found that Loth's original model was not empirically supported near $Re_p = 45$. They reported an updated model that corrects for these discrepancies in Loth *et al.* (2021). However, updates in that paper do not meaningfully affect the cone–cylinder simulation in § 3.3 because, again, it has a maximum Re_p of about 23. We thus employ the original formulation of Loth (2008), as presented above.

Appendix C. B-spline filtering

For the baseline flow-only reconstruction defined in § 2.2.4, particle velocities are estimated from measured tracks via finite differencing as well as smoothing. Among available options, cubic B-splines provide a standard filtering approach because they yield C^2-continuous fits with good stability while relying only on low-order piecewise

https://doi.org/10.1017/jfm.2026.11913 Published online by Cambridge University Press

polynomials (Gesemann *et al.* 2016; Li *et al.* 2024). A representative cubic B-spline approximation for the x coordinate of a particle trajectory is

$$\widehat{x}(t) = \sum_{j=0}^{K} c_j \, \alpha\left(\frac{t - t_j'}{\Delta t}\right), \tag{C1}$$

where c_j are spline coefficients, $\{t_j' \mid j = 0, \ldots, K\}$ are uniformly spaced knots with spacing Δt and α denotes the cubic basis function (Skare & Andersson 2005):

$$\alpha(t) = \begin{cases} \dfrac{2}{3} - \left(1 - \dfrac{|t|}{2}\right) t^2, & 0 < |t| < 1, \\ \dfrac{\left(2 - |t|^3\right)}{6}, & 1 < |t| < 2, \\ 0, & |t| > 2. \end{cases} \tag{C2}$$

Velocity and acceleration are then obtained analytically as the first and second derivatives of $\widehat{x}$. Naturally, the same construction applies to the other spatial components.

The number of knots K controls the trade-off between smoothness and fidelity. Increasing K improves the ability of the spline to follow fine-scale fluctuations but risks fitting to measurement noise. Conversely, small-K splines over-smooth the trajectories. In practice, we set K adaptively such that each spline segment spans about 10 measured points, a choice tuned to ensure sufficient expressivity while effectively suppressing measurement noise. This choice of segment length is robust across the noise levels and achieves the optimal accuracy through supervision against the ground truth. This set-up represents an idealised, best-case scenario filtering that is not available in real experimental data. The spline coefficients are obtained by minimising the residual between measured and filtered positions in a least-squares sense, i.e. by minimising

$$\sum_{j=1}^{n_k} \left\| x_j^{(k)} - \widehat{x}(t_j) \right\|_2^2, \tag{C3}$$

where $x_j^{(k)}$ is the measured position at the jth time step t_j, $\widehat{x}$ is the spline estimate from (C1) evaluated at the same time and n_k is the total number of points in the track.

In our implementation, filtering is performed via MATLAB's `spap2` and `fnder` routines. While details of software usage are secondary, the essential point here is that B-spline filtering yields smoothed particle tracks from which velocities and accelerations can be determined in a consistent manner. These filtered quantities serve as inputs to the baseline reconstruction method introduced in § 2.2.4, used for comparison throughout our tests.

Appendix D. Cone–cylinder flow with low-inertia particles

Particles of lower inertia are simulated in the cone–cylinder flow, following the procedure in § 3.3. This case helps to assess the advantage of joint estimation over the flow-only mode much closer the tracer limit, as might be expected in a highly controlled experiment. To reduce inertia, the particle diameters are drawn from a Gaussian distribution with mean $d_p = 0.8$ μm and standard deviation 0.2 μm. The particle density and all other computational settings, including the number of particles and frames, advection scheme and boundary treatment, are kept the same as in § 3.3. The resulting response time decreases to $\tau_p \approx 3.1$ μs, comparable to the TiO_2 response times reported by Ragni *et al.*

https://doi.org/10.1017/jfm.2026.11913 Published online by Cambridge University Press

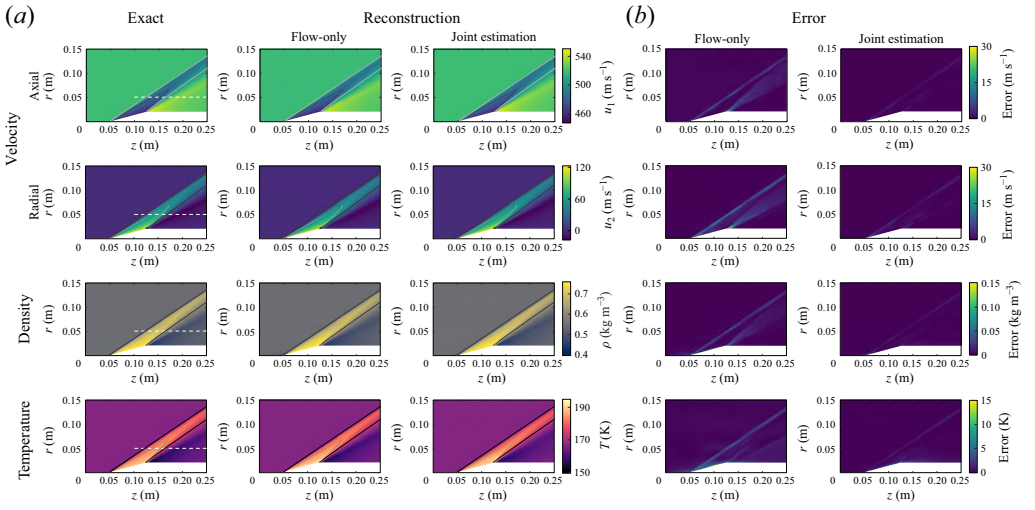


Figure 26. Cone–cylinder flow reconstruction with low-inertia particles at $\tau_p \approx 3$ µs. (*a*) Reconstructed flow fields compared with the CFD reference. (*b*) Absolute error fields, showing substantial error reduction with joint estimation even at low particle inertia. Dark and grey contour lines indicate low and high iso-values from the CFD reference, overlaid on the reconstructions for comparison. The iso-values are 480 and 506 m s^{-1} for the axial velocity component, 22 and 57 m s^{-1} for the radial velocity component, 0.59 and 0.70 kg m^{-3} for density and 172 and 183.5 K for temperature, respectively. The white dashed lines indicate the locations at which the flow profiles in figure 27 are extracted.

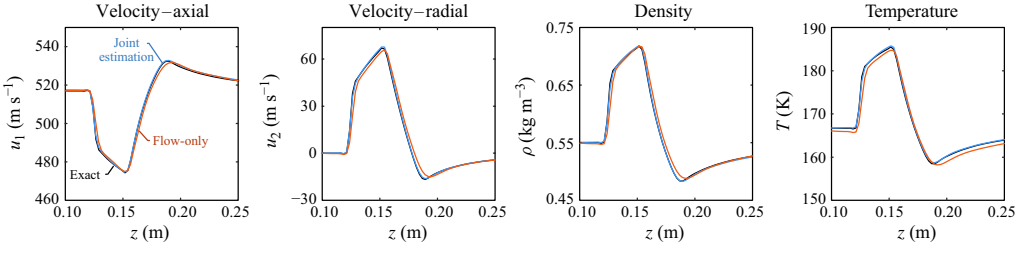


Figure 27. Flow-field cuts along the horizontal line at $r = 0.05$ m with $0.1\,\text{m} < z < 0.25\,\text{m}$. The exact simulation is shown in black, joint estimation in blue and flow-only reconstruction in red. Joint estimation nearly overlaps with the CFD data, whereas the flow-only result is shifted towards the post-shock region because of delayed particle response.

(2011). Figure 26 shows the reconstructed flow fields for the flow-only and joint estimation modes. Because these lower-inertia particles have better traceability, both reconstructions resemble the DNS reference closely, with only subtle visual differences.

To resolve those differences, figure 27 plots velocity, density and temperature profiles along a horizontal line at $r = 0.05$ m for $0.1\,\text{m} < z < 0.25\,\text{m}$. These profiles cross both the shock interface ($z \approx 0.12$ m) and the expansion fan ($z \approx 0.18$ m). The joint estimation results nearly overlap with the ground truth across the full line. The flow-only results capture the overall trends, but are shifted slightly towards the post-shock region because of the delayed particle response. Such discrepancies are expected to be much more significant for fluctuations in high-speed flows. The corresponding absolute-error fields are shown in figure 26(*b*). As expected, the flow-only mode exhibits its largest errors across the shock and expansion regions, much as in the larger-inertia case of § 6.2. Joint estimation substantially reduces these errors, yielding NRMSEs of 0.4 % for the axial velocity, 5.2 %

https://doi.org/10.1017/jfm.2026.11913 Published online by Cambridge University Press

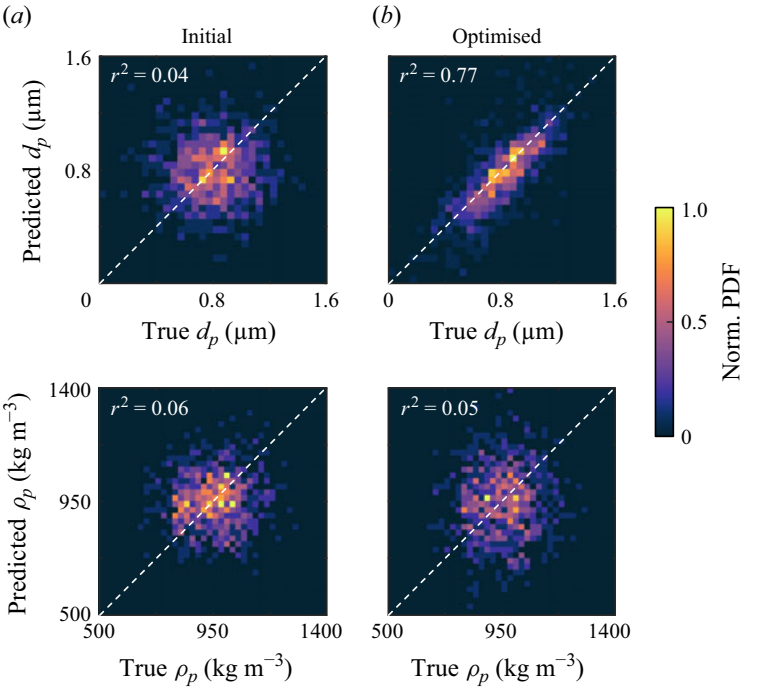


Figure 28. Implicit particle characterisation in the cone–cylinder flow with low-inertia particles at $\tau_p \approx 3$ μs. Initial d_p and ρ_p values (*a*) and jointly optimised estimates (*b*) are compared with the ground truth.

for the radial velocity, 2.0 % for the density and 2.0 % for the temperature, compared with 1.0 %, 10.7 %, 6.8 % and 3.4 % for the flow-only mode.

Figure 28 shows the normalised PDFs of the inferred particle diameter and density from joint estimation, compared with their true distributions. As in the case with the greater-inertia case, shown in figure 17, d_p is recovered successfully from a random initialisation, whereas ρ_p does not converge because the reconstruction is only weakly sensitive to the particle density, as discussed in § 6.2. Taken together, these results indicate that joint particle–flow reconstruction remains sensitive to particle size even for submicrometre particles with relatively weak inertial effects.

Appendix E. Characterisation of neural expressivity

The HIT architecture summarised in table 1 is evaluated here, using DNS data to assess neural expressivity. Three subvolumes are extracted from the full HIT dataset described in § 3.2, with domain sizes of 128^3, 256^3 and 512^3 voxels. After dimensionalisation, these correspond to physical domains of 10^3, 20^3 and 40^3 cm^3, respectively. Five training datasets are constructed at two temporal resolutions, each spanning 100 frames over 0.04 s. Two high-resolution cases use the 128^3 and 256^3 domains at a temporal resolution of $0.05\tau_\eta$. Owing to memory limits, the 512^3 case is only tested at a coarser temporal resolution of $0.25\tau_\eta$, for which 21 frames are sampled uniformly from the corresponding high-resolution data. The 128^3 high-resolution case matches the conditions used for the inertial HIT study in § 3.2, allowing for direct comparison.

https://doi.org/10.1017/jfm.2026.11913 Published online by Cambridge University Press

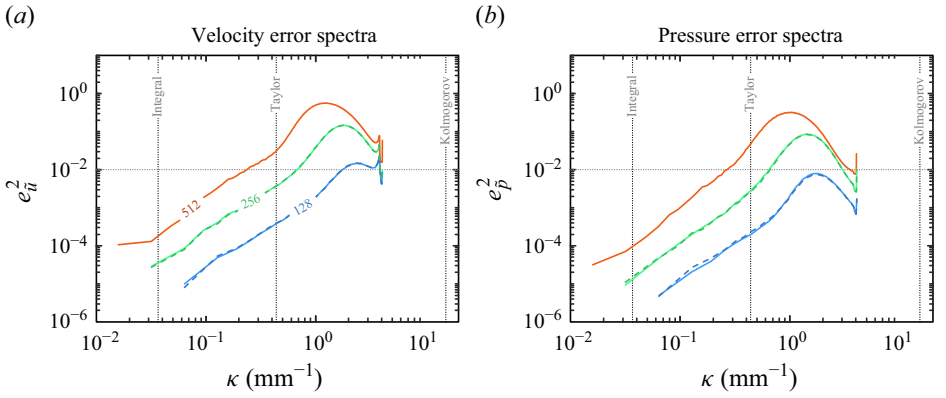


Figure 29. Velocity (*a*) and pressure (*b*) error spectra from idealised training on DNS data of HIT over three domain sizes: 128^3, 256^3 and 512^3 voxels. Dashed and solid lines denote high- and low-temporal-resolution cases, respectively. Vertical lines indicate the wavenumbers associated with the three turbulence length scales. The horizontal line marks an error threshold of 0.01, used to define the cutoff wavenumber for each domain size. The selected neural network resolves scales beyond the Taylor scale for the 128^3 and 256^3 domains, but only the large integral scales for the 512^3 domain.

To isolate representation error, the networks are trained to learn the DNS data with the idealised loss functions for velocity and pressure:

$$\mathscr{J}^{\boldsymbol{u}}_{ideal} = \frac{\dim(\boldsymbol{e}_f)^{-1}}{|\mathcal{V}\times\mathcal{T}|}\int_{\mathcal{T}}\int_{\mathcal{V}} \|\boldsymbol{u}-\boldsymbol{u}_{exact}\|_2^2 \,\mathrm{d}\boldsymbol{x}\,\mathrm{d}t \quad \text{and} \quad \mathscr{J}^{p}_{ideal} = \frac{\dim(\boldsymbol{e}_f)^{-1}}{|\mathcal{V}\times\mathcal{T}|}\int_{\mathcal{T}}\int_{\mathcal{V}} \|p-p_{exact}\|_2^2 \,\mathrm{d}\boldsymbol{x}\,\mathrm{d}t, \tag{E1}$$

where $(\cdot)_{exact}$ denotes a DNS quantity. The integrals are approximated by Monte Carlo sampling of the voxels and time steps, using batches of 5000 randomly sampled points. Both the velocity and pressure networks are trained using the procedure described in § 4.3, and all errors are evaluated at the higher temporal resolution. Hence, reconstruction errors serve as a proxy for network expressivity.

Figure 29 shows normalised velocity and pressure error spectra for the different domain sizes and temporal resolutions. Results for low and high temporal resolutions overlap nearly perfectly, indicating that temporal resolution is not the limiting factor in these tests. At low temporal resolution, the mean velocity NRMSEs are 1.1 %, 3.6 % and 9.6 % for the 128^3, 256^3 and 512^3 domains, respectively, while the corresponding pressure NRMSEs are 1.6 %, 3.6 % and 7.1 %. In each case, the difference relative to the corresponding high-resolution result is below 0.1 %. Naturally, errors systematically increase with domain size, due to the increased spectral content and constant neural expressivity. By comparison, the inertial HIT reconstruction in § 3.2 yields velocity and pressure NRMSEs of 5.0 % and 17.2 %, both being far larger than the ideal-training errors of 1.1 % and 1.6 % for the matched 128^3 case. This indicates that the inertial HIT results are not limited by the neural representation, but rather by the conditioning of the inverse problem, i.e. the finite seeding density and particle inertia.

Appendix F. Initialisation of the KCT models

F.1. *Track splitting*

Particle tracks in LPT vary in length, ranging from only a few positions to several hundred. Since TensorFlow requires fixed tensor shapes for computational graphs, we divide each trajectory into fixed-length segments of 20 positions. Shorter segments are

https://doi.org/10.1017/jfm.2026.11913 Published online by Cambridge University Press

zero-padded. When a single trajectory spans multiple segments, its particle properties (e.g. size, density) are shared across all segments; these properties may be trainable in cases with inertial particles. Although longer segments are possible, they increase the number and dimension of coefficient matrices in (2.28)–(2.29), thereby raising the computational cost and memory demand of KCTs. Conversely, very short segments disrupt the continuity of tracks and introduce boundary-related artefacts. In practice, therefore, segment lengths of 15–30 points strike a good balance between efficiency and fidelity.

F.2. *Warm-starting KCTs with filtered tracks*

For inertial particles, joint optimisation of flow states, particle positions and per-particle properties from noisy data is ill-posed and prone to divergence. To improve stability, we 'warm-start' each KCT model using filtered tracks obtained from a conventional smoothing technique, such as polynomial regression or kernel convolution (Berk 2024). Initialisation is posed as a per-track optimisation that identifies the displacement vector $\boldsymbol{\delta}$ and velocity parameters $\boldsymbol{\theta}$ which minimise

$$\mathscr{J}_{warm} = \sum_{j=1}^{n_k} \left(\| \boldsymbol{v}_j - \widehat{\boldsymbol{v}}_j \|_2^2 + \chi \| \boldsymbol{a}_j - \widehat{\boldsymbol{a}}_j \|_2^2 \right), \tag{F1}$$

where χ balances velocity and acceleration residuals and is assigned as

$$\chi = \frac{\langle \| \widehat{\boldsymbol{v}} \|_2 \rangle_p}{\langle \| \widehat{\boldsymbol{a}} \|_2 \rangle_p}, \tag{F2}$$

with $\langle \cdot \rangle_p$ indicating an average over the current track. Velocities $\boldsymbol{v}$ and accelerations $\boldsymbol{a}$ are the outputs of the particle model $\mathsf{P}^{(k)}$ from (2.27) and (2.29).

We minimise (F1) using MATLAB's implementation of the Levenberg–Marquardt algorithm, initialising $\boldsymbol{\delta}$ with raw (noisy, observed) positions and $\boldsymbol{\theta}$ with zeros. In this study, fifth-order polynomials provide the filtered velocity and acceleration vectors $\widehat{\boldsymbol{v}}$ and $\widehat{\boldsymbol{a}}$, though more advanced methods such as TrackFit (Gesemann *et al.* 2016) could also be employed. This warm-start is only used for cases with inertial particles. For ideal tracers, initialising with filtered tracks offers no improvement and risks biasing the reconstruction, so we simply initialise $\boldsymbol{\delta}$ with raw data and $\boldsymbol{\theta}$ with zeros.

F.3. *Particle property transform*

In inertial cases, particle properties such as their size and density can differ in units and span several orders of magnitude, limiting the precision of optimisation. Therefore, we map each positive property $\varphi > 0$ to a dimensionless variable $\xi \sim O(1)$, with the latter variable being optimised. The forward transformation is

$$\xi = \frac{\log\left[\exp(c_1\varphi) - 1\right]}{c_2} - c_3, \tag{F3}$$

with parameters c_1, c_2 and c_3 chosen so that ξ is of order one. The inverse transform recovers φ:

$$\varphi = \frac{\log\left[\exp(c_2\xi + c_2c_3) + 1\right]}{c_1} = \frac{\mathrm{softplus}(c_2\xi + c_2c_3)}{c_1}, \tag{F4}$$

where the softplus function ensures that $\varphi > 0$ for $c_1 > 0$.

Parameters are chosen as follows. First, c_1 is set to φ^{-1}, so $c_1\varphi = 1$. Second, given an expected range $\varphi \in [\varphi_{min}, \varphi_{max}]$, we determine c_2 and c_3 by enforcing $\xi(\varphi_{min}) = -1$ and

https://doi.org/10.1017/jfm.2026.11913 Published online by Cambridge University Press

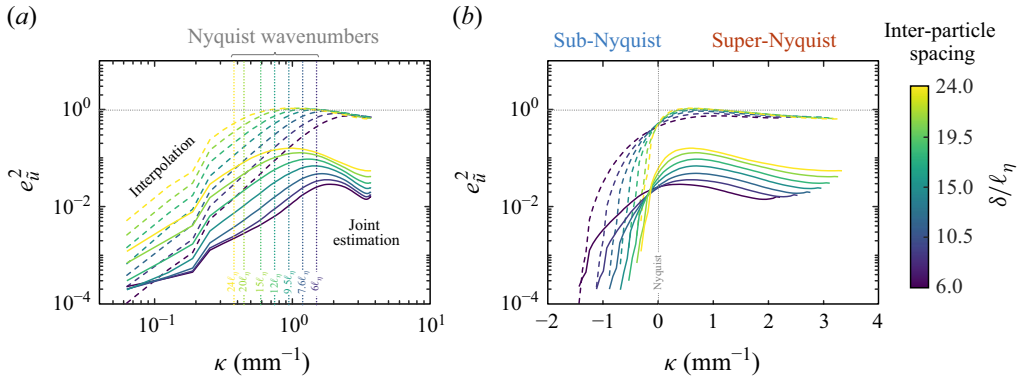


Figure 30. Error spectra of HIT reconstructions in the tracer limit ($St \to 0$) under varying inter-particle spacings. Spectra are shown versus wavenumber (*a*) and normalised by the Nyquist wavenumber (*b*). Colours denote particle spacing. Dashed lines indicate interpolation, and solid lines indicate joint estimation. Errors from joint estimation decrease rapidly in the super-Nyquist region because of the physical constraints, whereas naive interpolation asymptotes to 100 % error.

$\xi(\varphi_{max}) = 1$, yielding

$$c_2 = \frac{\log\left[\exp(c_1\varphi_{min}) - 1\right]}{c_3 - 1}, \qquad c_3 = \frac{2}{1-\zeta} - 1, \tag{F5a}$$

with

$$\zeta = \frac{\log\left[\exp(c_1\varphi_{min}) - 1\right]}{\log\left[\exp(c_1\varphi_{max}) - 1\right]}. \tag{F5b}$$

This mapping is bijective and has bounded gradients, ensuring one-to-one correspondence between ψ and ξ and stable optimisation during backpropagation. The formulation is valid for strictly positive (or negative) properties such as size and density; properties that may cross zero, such as electrical charge, require a different mapping.

Appendix G. Reconstruction accuracy for noise-free tracers

The capability of joint estimation to recover under-resolved dynamics from ideal tracers is numerically assessed and compared with naive interpolation by adaptive Gaussian windowing (Agüí & Jimenez 1987). Here HIT is used as a representative flow case. Noise-free tracks of perfect tracers are simulated using the same numerical settings as in § 3.2, including the domain size, temporal resolution and advection scheme. The number of tracks is varied to produce inter-particle spacings from $6\ell_\eta$ to $24\ell_\eta$, corresponding to particle image densities from 0.1 to 0.0016 ppp for a 1 MP camera.

Figure 30 compares the velocity error spectra obtained by joint estimation and by interpolation. Figure 30(*a*) shows the spectra in absolute wavenumbers, with the particle-sampling Nyquist wavenumbers indicated for reference. Joint estimation reduces the error by one to two orders of magnitude compared with interpolation, especially at high wavenumbers. Figure 30(*b*) shows the error spectra versus the relative wavenumbers, i.e. relative to κ_{Nyq}. Whereas the interpolation method saturates near 100 % error across all cases, joint estimation yields progressively smaller errors as the particle spacing decreases. This result illustrates the possibility for DA to recover flow information beyond the nominal sampling limit. However, this capability has not yet been definitively established for experimental data, which motivates further exploration.

https://doi.org/10.1017/jfm.2026.11913 Published online by Cambridge University Press

References

Agüí, J.C. & Jimenez, J. 1987 On the performance of particle tracking. *J. Fluid Mech.* **185**, 447–468.

Aliseda, A., Cartellier, A., Hainaux, F. & Lasheras, J.C. 2002 Effect of preferential concentration on the settling velocity of heavy particles in homogeneous isotropic turbulence. *J. Fluid Mech.* **468**, 77–105.

Anderson, J.D. 1990 *Modern Compressible Flow: With Historical Perspective*, vol. 12. McGraw-Hill.

Argyropoulos, C.D. & Markatos, N. 2015 Recent advances on the numerical modelling of turbulent flows. *Appl. Math. Model.* **39** (2), 693–732.

Bec, J. 2003 Fractal clustering of inertial particles in random flows. *Phys. Fluids* **15** (11), L81–L84.

Beresh, S.J. 2021 Time-resolved particle image velocimetry. *Meas. Sci. Technol.* **32** (10), 102003.

Berk, T. 2024 A second-order polynomial kernel outperforms Gaussian kernels when smoothing Lagrangian particle trajectories. *Exp. Fluids* **65** (7), 1–4.

Berk, T. & Coletti, F. 2021 Dynamics of small heavy particles in homogeneous turbulence: a Lagrangian experimental study. *J. Fluid Mech.* **917**, A47.

Berk, T. & Coletti, F. 2024 An analytical model for the slip velocity of particles in turbulence. *J. Fluid Mech.* **996**, A1.

Bewley, G.P., Saw, E.-W. & Bodenschatz, E. 2013 Observation of the sling effect. *New J. Phys.* **15** (8), 083051.

Bhattacharya, S. & Vlachos, P.P. 2020 Volumetric particle tracking velocimetry (PTV) uncertainty quantification. *Exp. Fluids* **61** (9), 197.

Boiko, V.M., Zapryagaev, V.I., Pivovarov, A.A. & Poplavski, S.V. 2015 Correction of PIV data for reconstruction of the gas velocity in a supersonic underexpanded jet. *Combust. Explos. Shock Waves* **51**, 587–596.

Brandt, L. & Coletti, F. 2022 Particle-laden turbulence: progress and perspectives. *Annu. Rev. Fluid Mech.* **54**, 159–189.

Bristow, N., Li, J., Hartford, P., Guala, M. & Hong, J. 2023 Imaging-based 3D particle tracking system for field characterization of particle dynamics in atmospheric flows. *Exp. Fluids* **64** (4), 78.

Buchta, D.A., Laurence, S.J. & Zaki, T.A. 2022 Assimilation of wall-pressure measurements in high-speed flow over a cone. *J. Fluid Mech.* **947**, R2.

Buchwald, T., Schanz, D. & Schröder, A. 2025 Accurate determination of acceleration statistics in a turbulent jet using locally adapted TrackFit. In *16th International Symposium on Particle Image Velocimetry, 1*, vol. 1061, pp. 1–10. ISPIV 2025 Organizing Committee.

Capecelatro, J. & Wagner, J.L. 2023 Gas–Particle dynamics in high-speed flows. *Annu. Rev. Fluid Mech.* **56**, 379–403.

Cary, A.W., Chawner, J., Duque, E.P., Gropp, W., Kleb, W.L., Kolonay, R.M., Nielsen, E. & Smith, B. 2021 CFD vision 2030 road map: progress and perspectives. In *AIAA Aviation 2021 Forum*, p. 2726. American Institute of Aeronautics and Astronautics.

Casa, L.D.C. & Krueger, P.S. 2013 Radial basis function interpolation of unstructured, three-dimensional, volumetric particle tracking velocimetry data. *Meas. Sci. Technol.* **24** (6), 065304.

Corrsin, S. 1951 On the spectrum of isotropic temperature fluctuations in an isotropic turbulence. *J. Appl. Phys.* **22** (4), 469–473.

Deng, Z., He, C., Wen, X. & Liu, Y. 2018 Recovering turbulent flow field from local quantity measurement: turbulence modeling using ensemble-Kalman-filter-based data assimilation. *J. Vis.* **21** (6), 1043–1063.

Di Leoni, P.C., Agarwal, K., Zaki, T.A., Meneveau, C. & Katz, J. 2023 Reconstructing turbulent velocity and pressure fields from under-resolved noisy particle tracks using physics-informed neural networks. *Exp. Fluids* **64** (5), 95.

Domínguez-Vázquez, D., Escobar-Castaneda, N., Wang, Q. & Jacobs, G.B. 2025 Inference of inertial particle dynamics from limited measurements. *Phys. Fluids* **37** (4), 043361.

Duraisamy, K., Iaccarino, G. & Xiao, H. 2019 Turbulence modeling in the age of data. *Annu. Rev. Fluid Mech.* **51** (1), 357–377.

Eaton, J.K. 2009 Two-way coupled turbulence simulations of gas-particle flows using point-particle tracking. *Intl J. Multiphase Flow* **35** (9), 792–800.

Elghobashi, S. 1994 On predicting particle-laden turbulent flows. *Appl. Sci. Res.* **52**, 309–329.

Fahringer, T.W., Lynch, K.P. & Thurow, B.S. 2015 Volumetric particle image velocimetry with a single plenoptic camera. *Meas. Sci. Technol.* **26** (11), 115201.

Faiella, M., Macmillan, C.G.J., Whitehead, J.P. & Pan, Z. 2021 Error propagation dynamics of velocimetry-based pressure field calculations (2): on the error profile. *Meas. Sci. Technol.* **32** (8), 084005.

Faleiros, D.E., Tuinstra, M., Sciacchitano, A. & Scarano, F. 2021 The slip velocity of nearly neutrally buoyant tracers for large-scale PIV. *Exp. Fluids* **62** (9), 186.

https://doi.org/10.1017/jfm.2026.11913 Published online by Cambridge University Press

FERRAN, A., MACHICOANE, N., ALISEDA, A. & OBLIGADO, M. 2023 An experimental study on the settling velocity of inertial particles in different homogeneous isotropic turbulent flows. *J. Fluid Mech.* **970**, A23.
FOURES, D.P.G., DOVETTA, N., SIPP, D. & SCHMID, P.J. 2014 A data-assimilation method for Reynolds-averaged Navier–Stokes-driven mean flow reconstruction. *J. Fluid Mech.* **759**, 404–431.
GAO, J., GUILDENBECHER, D.R., REU, P.L. & CHEN, J. 2013 Uncertainty characterization of particle depth measurement using digital in-line holography and the hybrid method. *Opt. Express* **21** (22), 26432–26449.
VAN GENT, P.L. *et al.* 2017 Comparative assessment of pressure field reconstructions from particle image velocimetry measurements and Lagrangian particle tracking. *Exp. Fluids* **58**, 1–23.
GESEMANN, S. 2021 TrackFit: uncertainty quantification, optimal filtering and interpolation of tracks for time-resolved Lagrangian particle tracking. In *14th International Symposium on Particle Image Velocimetry*, vol. 1. ISPIV 2021 Organizing Committee.
GESEMANN, S., HUHN, F., SCHANZ, D. & SCHRÖDER, A. 2016 From noisy particle tracks to velocity, acceleration and pressure fields using B-splines and penalties. In *18th International Symposium on Applications of Laser and Imaging Techniques to Fluid Mechanics*, vol. 4, pp. 1–17. LISBON Simposia.
GORLÉ, C., GARCIA-SANCHEZ, C. & IACCARINO, G. 2015 Quantifying inflow and RANS turbulence model form uncertainties for wind engineering flows. *J. Wind Engng Ind. Aerodyn.* **144**, 202–212.
GRONSKIS, A., HEITZ, D. & MÉMIN, E. 2013 Inflow and initial conditions for direct numerical simulation based on adjoint data assimilation. *J. Comput. Phys.* **242**, 480–497.
GUO, T., ARDEKANI, A.M. & VLACHOS, P.P. 2019 Microscale, scanning defocusing volumetric particle-tracking velocimetry. *Exp. Fluids* **60**, 1–14.
GUTIERREZ, L. & WANG, Q. 2026 Mixed Lagrangian–Eulerian data assimilation for turbulent channel flows. In *AIAA SciTech 2026 Forum*, p. 0682. American Institute of Aeronautics and Astronautics.
HALL, E.M., GUILDENBECHER, D.R. & THUROW, B.S. 2017 Uncertainty characterization of particle location from refocused plenoptic images. *Opt. Lett.* **25** (18), 21801–21814.
HE, C., LI, S. & LIU, Y. 2025 Data assimilation: new impetus in experimental fluid dynamics. *Exp. Fluids* **66**, 94.
HE, C., ZENG, X., WANG, P., WEN, X. & LIU, Y. 2024 Four-dimensional variational data assimilation of a turbulent jet for super-temporal-resolution reconstruction. *J. Fluid Mech.* **978**, A14.
HUANG, J., LI, S., ZI, Y., QIAN, Y., CAI, W., ALDÉN, M. & LI, Z. 2021 Clustering-based particle detection method for digital holography to detect the three-dimensional location and in-plane size of particles. *Meas. Sci. Technol.* **32** (5), 055205.
JAGTAP, A.D. & KARNIADAKIS, G.E. 2023 How important are activation functions in regression and classification? A survey, performance comparison, and future directions. *J. Mach. Learn. Model. Comput.* **4** (1), 21–75.
JEON, Y.J., SCHNEIDERS, J.F.G., MÜLLER, M., MICHAELIS, D. & WIENEKE, B. 2018 4D flow field reconstruction from particle tracks by VIC+ with additional constraints and multigrid approximation. In *Proceedings 18th International Symposium on Flow Visualization*, p. 1. ETH Zurich.
JOHNSON, C., MYSORE, P.V., SCHAU, K.A. & OEFELEIN, J. 2023 Sensitivity of shock-wave boundary-layer interactions to inflow turbulence characteristics using the synthetic eddy method. In *AIAA SciTech 2023 Forum*, p. 0094. American Institute of Aeronautics and Astronautics.
JUX, C., SCIACCHITANO, A. & SCARANO, F. 2020 Flow pressure evaluation on generic surfaces by robotic volumetric PTV. *Meas. Sci. Technol.* **31** (10), 104001.
KATZ, J. & SHENG, J. 2010 Applications of holography in fluid mechanics and particle dynamics. *Annu. Rev. Fluid Mech.* **42**, 531–555.
KE, H., YOU, Z. & WANG, Q. 2026 Preconditioned adjoint data assimilation for two-dimensional decaying isotropic turbulence. arXiv:2602.14016.
KHALITOV, D.A. & LONGMIRE, E.K. 2002 Simultaneous two-phase PIV by two-parameter phase discrimination. *Exp. Fluids* **32** (2), 252–268.
KOIKE, S., TAKAHASHI, H., TANAKA, K., HIROTA, M., TAKITA, K. & MASUYA, G. 2007 Correction method for particle velocimetry data based on the Stokes drag law. *AIAA J.* **45** (11), 2770–2777.
KOLMOGOROV, A.N. 1941 The local structure of turbulence in incompressible viscous fluid for very large Reynolds numbers. *Dokl. Akad. Nauk SSSR* **30** (4), 299–301.
LAWSON, J.M., BODENSCHATZ, E., LALESCU, C.C. & WILCZEK, M. 2018 Bias in particle tracking acceleration measurement. *Exp. Fluids* **59** (11), 172.
LEAKE, C., JOHNSON, H. & MORTARI, D. 2022 *The Theory of Functional Connections: A Functional Interpolation Framework with Applications*. Lulu.com.
LI, J., GUALA, M. & HONG, J. 2022 Snow particle analyzer for simultaneous measurements of snow density and morphology. arXiv:2209.11129.

https://doi.org/10.1017/jfm.2026.11913 Published online by Cambridge University Press

LI, J., GUALA, M. & HONG, J. 2024 Field investigation of 3-D snow settling dynamics under weak atmospheric turbulence. *J. Fluid Mech.* **997**, A33.
LI, L. & PAN, Z. 2024 Three-dimensional time-resolved Lagrangian flow field reconstruction based on constrained least squares and stable radial basis function. *Exp. Fluids* **65** (4), 57.
LING, Y., PARMAR, M. & BALACHANDAR, S. 2013 A scaling analysis of added-mass and history forces and their coupling in dispersed multiphase flows. *Intl J. Multiphase Flow* **57**, 102–114.
LOTH, E. 2008 Compressibility and rarefaction effects on drag of a spherical particle. *AIAA J.* **46** (9), 2219–2228.
LOTH, E., DASPIT, J.T., JEONG, M., NAGATA, T. & NONOMURA, T. 2021 Supersonic and hypersonic drag coefficients for a sphere. *AIAA J.* **59** (8), 3261–3274.
LYNCH, K. & SCARANO, F. 2013 A high-order time-accurate interrogation method for time-resolved PIV. *Meas. Sci. Technol.* **24** (3), 035305.
MALIK, N., DRACOS, T. & PAPANTONIOU, D. 1993 Particle tracking velocimetry in three-dimensional flows. *Exp. Fluids* **15** (4), 279–294.
MALIK, N.A. & DRACOS, T. 1995 Interpolation schemes for three-dimensional velocity fields from scattered data using Taylor expansions. *J. Comput. Phys.* **119** (2), 231–243.
MALLERY, K. & HONG, J. 2019 Regularized inverse holographic volume reconstruction for 3D particle tracking. *Opt. Express* **27** (13), 18069–18084.
MALLERY, K., SHAO, S. & HONG, J. 2020 Dense particle tracking using a learned predictive model. *Exp. Fluids* **61** (10), 223.
MANOVSKI, P., NOVARA, M., MOHAN, N.K.D., GEISLER, R., SCHANZ, D., AGOCS, J., GODBERSEN, P. & SCHRÖDER, A. 2021 3D Lagrangian particle tracking of a subsonic jet using multi-pulse shake-the-box. *Exp. Therm. Fluid Sci.* **123**, 110346.
MAXEY, M.R., PATEL, B.K., CHANG, E.J. & WANG, L.P. 1997 Simulations of dispersed turbulent multiphase flow. *Fluid Dyn. Res.* **20** (1–6), 143.
MAXEY, M.R. & RILEY, J.J. 1983 Equation of motion for a small rigid sphere in a nonuniform flow. *Phys. Fluids* **26** (4), 883–889.
MEI, R. 1996 Velocity fidelity of flow tracer particles. *Exp. Fluids* **22** (1), 1–13.
MELLING, A. 1997 Tracer particles and seeding for particle image velocimetry. *Meas. Sci. Technol.* **8** (12), 1406.
MOAVEN, M., GURURAJ, A., RAGHAV, V. & THUROW, B. 2024 Improving depth uncertainty in plenoptic camera-based velocimetry. *Exp. Fluids* **65** (4), 49.
MOLNAR, J.P., GRAUER, S.J., LÉON, O., DONJAT, D. & NICOLAS, F. 2023 Physics-informed background-oriented schlieren of turbulent underexpanded jets. In *AIAA SciTech 2023 Forum*, p. 2441. American Institute of Aeronautics and Astronautics.
MORDANT, N., CRAWFORD, A.M. & BODENSCHATZ, E. 2004 Experimental Lagrangian acceleration probability density function measurement. *Phys. D: Nonlinear Phenom.* **193** (1–4), 245–251.
MURALIDHAR, K. 2002 Temperature field measurement in buoyancy-driven flows using interferometric tomography. *Annu. Rev. Heat Transfer* **12**, 265–375.
NIE, M., WHITEHEAD, J.P., RICHARDS, G., SMITH, B.L. & PAN, Z. 2022 Error propagation dynamics of PIV-based pressure field calculation (3): what is the minimum resolvable pressure in a reconstructed field? *Exp. Fluids* **63** (11), 168.
NOVARA, M., SCHANZ, D., GEISLER, R., GESEMANN, S., VOSS, C. & SCHRÖDER, A. 2019 Multi-exposed recordings for 3D Lagrangian particle tracking with multi-pulse shake-the-box. *Exp. Fluids* **60**, 1–19.
OBUKHOV, A.M. 1949 The local structure of atmospheric turbulence. *Dokl. Akad. Nauk SSSR* **67** (4), 643–646.
PAN, Z., WHITEHEAD, J., THOMSON, S. & TRUSCOTT, T. 2016 Error propagation dynamics of PIV-based pressure field calculations: how well does the pressure Poisson solver perform inherently? *Meas. Sci. Technol.* **27** (8), 084012.
PARMAR, M., HASELBACHER, A. & BALACHANDAR, S. 2009 Modeling of the unsteady force for shock–particle interaction. *Shock Waves* **19**, 317–329.
PERLMAN, E., BURNS, R., LI, Y. & MENEVEAU, C. 2007 Data exploration of turbulence simulations using a database cluster. In *Proceedings of the 2007 ACM/IEEE Conference on Supercomputing*, pp. 1–11. Association for Computing Machinery.
PETERSEN, A.J., BAKER, L. & COLETTI, F. 2019 Experimental study of inertial particles clustering and settling in homogeneous turbulence. *J. Fluid Mech.* **864**, 925–970.
RAFFEL, M., WILLERT, C.E., SCARANO, F., KÄHLER, C.J., WERELEY, S.T. & KOMPENHANS, J. 2018 Physical and technical background. In *Particle Image Velocimetry: A Practical Guide*, pp. 33–111. Springer.
RAGNI, D., SCHRIJER, F., VAN OUDHEUSDEN, B.W. & SCARANO, F. 2011 Particle tracer response across shocks measured by PIV. *Exp. Fluids* **50**, 53–64.

https://doi.org/10.1017/jfm.2026.11913 Published online by Cambridge University Press

RAISSI, M., PERDIKARIS, P. & KARNIADAKIS, G.E. 2019 Physics-informed neural networks: a deep learning framework for solving forward and inverse problems involving nonlinear partial differential equations. *J. Comput. Phys.* **378**, 686–707.

RIGHETTI, M. & ROMANO, G.P. 2004 Particle–fluid interactions in a plane near-wall turbulent flow. *J. Fluid Mech.* **505**, 93–121.

RIVAL, D.E. & VAN OUDHEUSDEN, B. 2017 Load-estimation techniques for unsteady incompressible flows. *Exp. Fluids* **58** (3), 20.

ROSA, B., PARISHANI, H., AYALA, O. & WANG, L.-P. 2016 Settling velocity of small inertial particles in homogeneous isotropic turbulence from high-resolution DNS. *Intl J. Multiphase Flow* **83**, 217–231.

ROSALES, C. & MENEVEAU, C. 2005 Linear forcing in numerical simulations of isotropic turbulence: physical space implementations and convergence properties. *Phys. Fluids* **17** (9), 095106.

ROY, C.J. & BLOTTNER, F.G. 2006 Review and assessment of turbulence models for hypersonic flows. *Prog. Aerosp. Sci.* **42** (7–8), 469–530.

SAMIMY, M. & LELE, S.K. 1991 Motion of particles with inertia in a compressible free shear layer. *Phys. Fluids A: Fluid Dyn.* **3** (8), 1915–1923.

SCARANO, F. 2012 Tomographic PIV: principles and practice. *Meas. Sci. Technol.* **24** (1), 012001.

SCARANO, F. & VAN OUDHEUSDEN, B.W. 2003 Planar velocity measurements of a two-dimensional compressible wake. *Exp. Fluids* **34** (3), 430–441.

SCHANZ, D., GESEMANN, S. & SCHRÖDER, A. 2016 Shake-the-box: Lagrangian particle tracking at high particle image densities. *Exp. Fluids* **57** (5), 1–27.

SCHANZ, D., JAHN, T. & SCHRÖDER, A. 2022 3D particle position determination and correction at high particle densities. In *20th International Symposium on the Application of Laser and Imaging Techniques to Fluid Mechanics, 1*, vol. 214, pp. 1933–1949.

SCHANZ, D., SCHRÖDER, A., GESEMANN, S., HUHN, F., NOVARA, M., GEISLER, R., MANOVSKI, P. & DEPURU-MOHAN, K. 2018 Recent advances in volumetric flow measurements: high-density particle tracking ('Shake-The-Box') with Navier–Stokes regularized interpolation ('FlowFit'). In *New Results in Numerical and Experimental Fluid Mechanics XI*, pp. 587–597. Springer Cham.

SCHILLER, V.L. 1933 Uber die grundlegenden Berechnungen bei der Schwerkraftaufbereitung. *Z. Verein. Deutsch. Ing.* **77**, 318–321.

SCHNEIDERS, J.F.G., SCARANO, F. & ELSINGA, G.E. 2017 Resolving vorticity and dissipation in a turbulent boundary layer by tomographic PTV and VIC+. *Exp. Fluids* **58** (4), 1–14.

SCHRÖDER, A., GEISLER, R., SIEVERLING, A., WIENEKE, B., HENNING, A., SCARANO, F., ELSINGA, G.E. & POELMA, C. 2009 Lagrangian aspects of coherent structures in a turbulent boundary layer flow using TR-Tomo PIV and PTV. In *Proceedings of 8th International Symposium on Particle Image Velocimetry*, pp. 25–28. ISPIV 2009 Organizing Committee.

SCHRÖDER, A. & SCHANZ, D. 2023 3D Lagrangian particle tracking in fluid mechanics. *Annu. Rev. Fluid Mech.* **55**, 511–540.

SCHRÖDER, A., SCHANZ, D., GEISLER, R., GODBERSEN, P., AGOCS, J. & SIMHAN, A.R. 2024 Near-wall flow features in ZPG-TBL at various Reynolds numbers using dense 3D Lagrangian particle tracking. In *21st International Symposium on the Application of Laser and Imaging Techniques to Fluid Mechanics*, p. 1. LISBON Simposia.

SCHRÖDER, A., SCHANZ, D., GEISLER, R., VOSS, C., SHIN, H., GODBERSEN, P., AGOCS, J. & SIMHAN, A. 2025 On the spatial and temporal development of reverse flow-and high wall-shear stress events in ZPG-TBL. In *16th International Symposium on Particle Image Velocimetry, 1*, vol. 1170, pp. 1–12. ISPIV 2025 Organizing Committee.

SCHRÖDER, A., SCHANZ, D., GESEMANN, S., HUHN, F., GARABOA-PAZ, D. & BODENSCHATZ, E. 2022 Measurements of the energy dissipation rate in homogeneous turbulence using dense 3D Lagrangian particle tracking and FlowFit. In *Proceedings of the 20th International Symposium on the Application of Laser and Imaging Techniques to Fluid Mechanics, 1*, vol. 216, pp. 2300–2319. LISBON Simposia.

SHAO, S., MALLERY, K., KUMAR, S.S. & HONG, J. 2020 Machine learning holography for 3D particle field imaging. *Opt. Express* **28** (3), 2987–2999.

SHIN, H. & SCHRÖDER, A. 2025 Robust flow field reconstruction using PINN for 3D Lagrangian particle tracking. In *16th International Symposium on Particle Image Velocimetry, 1*, vol. 1142, pp. 1–12. ISPIV 2025 Organizing Committee.

SKARE, S. & ANDERSSON, J. 2005 Correction of MR image distortions induced by metallic objects using a 3D cubic B-spline basis set: application to stereotactic surgical planning. *Magn. Reson. Med.* **54** (1), 169–181.

https://doi.org/10.1017/jfm.2026.11913 Published online by Cambridge University Press

SLOTNICK, J.P., KHODADOUST, A., ALONSO, J., DARMOFAL, D., GROPP, W., LURIE, E. & MAVRIPLIS, D.J. 2014 CFD vision 2030 study: a path to revolutionary computational aerosciences. *Tech. Rep.* NF1676L–18332. National Aeronautics and Space Administration.

SUBRAMANIAM, S. & BALACHANDAR, S. 2022 *Modeling Approaches and Computational Methods for Particle-Laden Turbulent Flows*. Academic Press.

TANCIK, M., SRINIVASAN, P., MILDENHALL, B., FRIDOVICH-KEIL, S., RAGHAVAN, N., SINGHAL, U., RAMAMOORTHI, R., BARRON, J. & NG, R. 2020 Fourier features let networks learn high frequency functions in low dimensional domains. *Adv. Neural Inform. Proc. Syst.* **33**, 7537–7547.

TANG, R., ZHOU, K., TAN, J. & GRAUER, S.J. 2026 Neural inference of fluid–structure interactions from sparse off-body measurements. *Phys. Rev. Fluids* **11**, 074901.

THOMAS, P. 1992 On the influence of the Basset history force on the motion of a particle through a fluid. *Phys. Fluids* **4** (9), 2090–2093.

TOLOUI, M. & HONG, J. 2015 High fidelity digital inline holographic method for 3D flow measurements. *Opt. Express* **23** (21), 27159–27173.

DE LA TORRE, R.G.R. & JENSEN, A. 2023 Sizing of particles and droplets using 3D-PTV, an OpenPTV post-processing tool. *Meas. Sci. Technol.* **34** (6), 065404.

URBAN, W.D. & MUNGAL, M. 2001 Planar velocity measurements in compressible mixing layers. *J. Fluid Mech.* **431**, 189–222.

VENKATAKRISHNAN, L. & MEIER, G.E.A. 2004 Density measurements using the background oriented schlieren technique. *Exp. Fluids* **37**, 237–247.

VOSSKUHLE, M., PUMIR, A., LÉVÊQUE, E. & WILKINSON, M. 2014 Prevalence of the sling effect for enhancing collision rates in turbulent suspensions. *J. Fluid Mech.* **749**, 841–852.

VOTH, G.A., LA PORTA, A., CRAWFORD, A.M., ALEXANDER, J. & BODENSCHATZ, E. 2002 Measurement of particle accelerations in fully developed turbulence. *J. Fluid Mech.* **469**, 121–160.

WANG, L.-P. & MAXEY, M.R. 1993 Settling velocity and concentration distribution of heavy particles in homogeneous isotropic turbulence. *J. Fluid Mech.* **256**, 27–68.

WANG, S., BHARTARI, A.K., LI, B. & PERDIKARIS, P. 2025 Gradient alignment in physics-informed neural networks: a second-order optimization perspective. arXiv:2502.00604.

WANG, S., LI, B., CHEN, Y. & PERDIKARIS, P. 2024 Piratenets: physics-informed deep learning with residual adaptive networks. *J. Mach. Learn. Res.* **25** (402), 1–51.

WANG, S., TENG, Y. & PERDIKARIS, P. 2021 Understanding and mitigating gradient flow pathologies in physics-informed neural networks. *SIAM J. Sci. Comput.* **43** (5), A3055–A3081.

WANG, S., YU, X. & PERDIKARIS, P. 2022 When and why PINNs fail to train: a neural tangent kernel perspective. *J. Comput. Phys.* **449**, 110768.

WANG, Y. & LAI, C.-Y. 2024 Multi-stage neural networks: function approximator of machine precision. *J. Comput. Phys.* **504**, 112865.

WEISS, S., SCHANZ, D., ERDOGDU, A.O., SCHRÖDER, A. & BOSBACH, J. 2023 Investigation of turbulent superstructures in Rayleigh–Bénard convection by Lagrangian particle tracking of fluorescent microspheres. *Exp. Fluids* **64** (4), 82.

WIENEKE, B. 2012 Iterative reconstruction of volumetric particle distribution. *Meas. Sci. Technol.* **24**, 1–14.

WIENEKE, B. & ROCKSTROH, T. 2024 Lagrangian particle tracking in the presence of obstructing objects. *Meas. Sci. Technol.* **35** (5), 055303.

WILL, J.B., MATHAI, V., HUISMAN, S.G., LOHSE, D., SUN, C. & KRUG, D. 2021 Kinematics and dynamics of freely rising spheroids at high Reynolds numbers. *J. Fluid Mech.* **912**, A16.

WILLIAMS, O.J.H. 2014 Density effects on turbulent boundary layer structure: from the atmosphere to hypersonic flow. PhD thesis, Princeton University, NJ, USA.

WILLIAMS, O.J.H., NGUYEN, T., SCHREYER, A.-M. & SMITS, A.J. 2015 Particle response analysis for particle image velocimetry in supersonic flows. *Phys. Fluids* **27** (7), 076101.

WISSINK, J.G. & HERLINA, H. 2023 Surface-temperature-induced Marangoni effects on developing buoyancy-driven flow. *J. Fluid Mech.* **962**, A23.

WOLF, C.C., SCHWARZ, C., KAUFMANN, K., GARDNER, A.D., MICHAELIS, D., BOSBACH, J., SCHANZ, D. & SCHRÖDER, A. 2019 Experimental study of secondary vortex structures in a rotor wake. *Exp. Fluids* **60** (11), 175.

XIAO, H. & CINNELLA, P. 2019 Quantification of model uncertainty in RANS simulations: a review. *Prog. Aerosp. Sci.* **108**, 1–31.

YAMAKAITIS, M., BARDET, P., PIGEON, A., ANDERSON, J., PARKER, C. & EHRMANN, R. 2024*a* 3D particle tracking velocimetry to the wall in a zero pressure gradient turbulent boundary layer with a single plenoptic camera. In *APS Division of Fluid Dynamics Meeting Abstracts*, pp. C15-008. American Physical Society.

https://doi.org/10.1017/jfm.2026.11913 Published online by Cambridge University Press

YAMAKAITIS, M., PIGEON, A., EHRMANN, R., PARKER, C., ANDERSON, J. & BARDET, P. 2025*a* Time-resolved 3D particle tracking velocimetry with a single camera in the viscous layer and buffer region of a zero-pressure-gradient turbulent boundary layer. In *16th International Symposium on Particle Image Velocimetry*. ISPIV 2025 Organizing Committee.

YAMAKAITIS, M.J., REZAIGUIA, A., CAPANNA, R. & BARDET, P.M. 2024*b* Novel plenoptic imager for 3D particle tracking velocimetry for fluid structure interactions. In *Proceedings of the International Symposium on the Application of Laser and Imaging Techniques to Fluid Mechanics*. LISBON Simposia.

YAMAKAITIS, M.J., REZAIGUIA, A., FORT, C., CAPANNA, R. & BARDET, P.M. 2025*b* Four-view single-camera plenoptic 3.0 imager for three-dimensional Lagrangian particle tracking in an oscillatory laminar boundary layer. *Exp. Fluids* **66** (9), 165.

ZAKI, T.A. 2025 Turbulence from an observer perspective. *Annu. Rev. Fluid Mech.* **57**, 311–334.

ZAKI, T.A. & WANG, M. 2025 Data assimilation and flow estimation. In *Data Driven Analysis and Modeling of Turbulent Flows*, pp. 129–181. Elsevier.

ZHANG, W., WANG, Y. & LEE, S.J. 2008 Simultaneous PIV and PTV measurements of wind and sand particle velocities. *Exp. Fluids* **45**, 241–256.

ZHOU, K., GRAUER, S.J., SCHANZ, D., GODBERSEN, P., SCHRÖDER, A., ROCKSTROH, T., JEON, Y.J. & WIENEKE, B. 2024 Benchmarking data assimilation algorithms for 3D Lagrangian particle tracking. In *21st International Symposium on Applications of Laser and Imaging Techniques to Fluid Mechanics*, p. 229. LISBON Simposia.

ZHOU, K., LI, J., HONG, J. & GRAUER, S.J. 2023 Stochastic particle advection velocimetry (SPAV): theory, simulations, and proof-of-concept experiments. *Meas. Sci. Technol.* **34** (6), 065302.

https://doi.org/10.1017/jfm.2026.11913 Published online by Cambridge University Press